GFZ Helmholtz Centre Potsdam

Institute of Geosciences

Universität Potsdam

Improvement of routine seismic source parameter estimation based on regional and teleseismic recordings

Nima Nooshiri

Dissertation
to obtain the academic degree
"doctor rerum naturalium" (Dr. rer. nat.)
in the scientific discipline Geophysics

Submitted to the
Faculty of Mathematics and Natural Sciences
at the University of Potsdam, Germany

Date of disputation: 4 February 2020

Primary advisor:	Prof. Dr. Torsten Dahm
Co-advisor:	Prof. Frederik Tilmann
Reviewers:	Prof. Dr. Torsten Dahm apl. Prof. Dr. Frank Krüger Dr. Steven J. Gibbons
Examining committee:	Prof. Dr. Max Wilke Prof. Dr. Torsten Dahm apl. Prof. Dr. Frank Krüger Prof. Dr. Eva Eibl Prof. Dr. Michael Weber

Published online at the
Institutional Repository of the University of Potsdam:
https://doi.org/10.25932/publishup-45946
https://nbn-resolving.org/urn:nbn:de:kobv:517-opus4-459462

Statement of originality

I hereby declare that this thesis is the product of my own work. All the assistance received in preparing this thesis and the sources used have been acknowledged.

Nima Nooshiri
March, 2020

Abstract

Seismological agencies seek to facilitate cooperation in seismological research and also seismic hazard mitigation by providing source parameters of seismic events (location, magnitude, mechanism), and keeping these data accessible in the long term. The availability of catalogues of seismic source parameters is expected to have considerable social and economic impact in the evaluation and mitigation of seismic hazards, and the catalogues are particularly valuable to the research community as they provide fundamental data in the geophysical sciences. This work is well motivated by the rising demand for developing more robust and efficient methods for routine source parameter estimation, and ultimately generation of reliable catalogues of seismic source parameters. Specifically, the aim of this work is to develop some methods to determine hypocentre location and temporal evolution of seismic sources based on regional and teleseismic observations more accurately, and investigate the potential of these methods to be integrated in near real-time processing.

To achieve this, a location method that considers several events simultaneously and improves the relative location accuracy among nearby events has been provided. This method tries to reduce the biasing effects of the lateral velocity heterogeneities (or equivalently to compensate for limitations and inaccuracies in the assumed velocity model) by calculating a set of timing corrections for each seismic station. The systematic errors introduced into the locations by the inaccuracies in the assumed velocity structure can be corrected without explicitly solving for a velocity model. Application to sets of multiple earthquakes in complex tectonic environments with strongly heterogeneous structure such as subduction zones and plate boundary region demonstrate that this relocation process significantly improves the hypocentre locations compared to standard locations.

To meet the computational demands of this location process, a new open-source software package has been developed that allows for efficient relocation of large-scale multiple seismic events using arrival time data. Upon that, a flexible location framework is provided which can be tailored to various application cases on local, regional, and global scales. The latest version of the software distribution including source codes, a user guide, an example data set, and a change history, is freely available to the community.

The developed relocation algorithm has been modified slightly and then its performance in a simulated near real-time processing has been evaluated. It has been demonstrated that applying the proposed technique significantly reduces the bias in routine locations and enhance the ability to locate the lower magnitude events using only regional arrival data.

Finally, to return to emphasis on global seismic monitoring, an inversion framework has been developed to determine the seismic source time function through direct waveform fitting of teleseismic recordings. The inversion technique can be systematically applied to moderate-size seismic events and has the potential to be performed in near real-time applications. It is exemplified by application to an abnormal seismic event; the 2017 North Korean nuclear explosion.

The presented work and application case studies in this dissertation represent the first step in an effort to establish a framework for automatic, routine generation of reliable catalogues of seismic event locations and source time functions.

Zusammenfassung

Seismologische Dienste spielen eine wichtige Rolle in der seismologischen Forschung und Gefährdungsanalyse, indem sie Quellparameter für seismische Ereignisse (Lokalisierung, Stärke, Mechanismus) bereitstellen und diese Daten langfristig verfügbar machen. Die Verfügbarkeit von Katalogen seismischer Quellparameter ist eine wichtige Voraussetzung für die Bewertung der seismischen Gefährdung und Minderung der Auswirkungen von Erdbeben. Die seismischen Kataloge sind für die Forschungsgemeinschaft besonders wertvoll, da sie grundlegende Hintergrundsdaten über lange Zeiträume liefern. Die vorliegende Arbeit ist motiviert durch die steigende Nachfrage nach der Entwicklung robusterer und effizienterer Methoden für die routinemäßige Schätzung von Quellparametern und schließlich die Verbesserung der Qualität und Quantität der seismischen Kataloge. Ziel dieser Arbeit ist es insbesondere Methoden zu entwickeln, um die Lokalisierung von Hypozentren und die zeitliche Entwicklung der Momentfreisetzung bei einem Erdbeben auf der Grundlage regionaler und teleseismischer Beobachtungen genauer zu bestimmen, und das Potenzial dieser Methoden für eine zeitnahe Verarbeitung zu untersuchen.

Um dies zu erreichen, wurde eine Lokalisierungsmethode bereitgestellt, die mehrere Ereignisse gleichzeitig berücksichtigt und die relative Genauigkeit der Hypozentren zwischen benachbarten Ereignissen verbessert. Dieses Verfahren versucht, die Verzerrungen durch Geschwindigkeits-heterogenitäten zu reduzieren, oder äquivalent Einschränkungen und Ungenauigkeiten in dem angenommenen Geschwindigkeitsmodell auszugleichen, indem richtungsabhängige Zeitkorrekturen für jede seismische Station berechnet werden. Die systematischen Fehler, die durch die Ungenauigkeiten in der angenommenen Geschwindigkeitsstruktur in die Lokalisierung projiziert werden, können korrigiert werden, ohne explizit nach einem Geschwindigkeitsmodell zu lösen. Die Anwendung auf Ensemble von Erdbeben in tektonischen Situationen mit stark heterogener, komplexer Struktur wie Subduktionszonen und Plattengrenzregionen zeigt, dass diese Relokalisierung die Hypozentren im Vergleich zu Standardlokalisierungen signifikant verbessert.

Um den rechnerischen Anforderungen der Lokalisierung gerecht zu werden, wurde ein neues Open-Source-Softwarepaket entwickelt, das eine effiziente Relokalisierung einer großen Anzahl von Erdbeben unter Verwendung von Ankunftszeitdaten ermöglicht. Daraufhin wird ein flexibler Lokalisierungsrahmen bereitgestellt, der an verschiedene Fälle auf lokaler, regionaler und globaler Ebene angepasst werden kann. Die neueste Version der Software einschließlich Quellcodes, Benutzerhandbuch, Beispieldatensatz und Änderungsverlauf ist für die Öffentlichkeit frei verfügbar.

Der entwickelte Relokalisierungs-Algorithmus wurde geringfügig verändert und anschließend seine Leistung in einem simulierten Echtzeit Prozess bewertet. Es zeigte sich, dass die Anwendung der vorgeschlagenen Technik die Verzerrung der Hypozentren der Routineauswertung erheblich verringert und die Fähigkeit zum Lokalisieren der Ereignisse mit niedriger Magnitude unter Verwendung nur regionaler Ankunftsdaten verbessert.

Um sich wieder auf die globale seismische Überwachung zu konzentrieren, wurde schließlich ein Inversionssystem entwickelt, um die Zeitfunktion der seismischen Quelle durch direkte Wellenformanpassung von teleseismischen Aufzeichnungen zu bestimmen. Die Inversion-

stechnik kann systematisch auf seismische Ereignisse mittlerer Größe angewendet werden und hat das Potenzial, in nahezu Echtzeitanwendungen ausgeführt zu werden. Dies wird beispielhaft durch die Anwendung auf ein abnormales seismisches Ereignis veranschaulicht: die nordkoreanische Atomexplosion 2017.

Die in dieser Dissertation vorgestellten Arbeits- und Anwendungsfallstudien stellen den ersten Schritt dar, um einen Rahmen für die automatische, routinemäßige Erzeugung zuverlässiger Kataloge von seismischen Ereignisorten und Quellzeitfunktion zu schaffen.

Acknowledgements

While writing this dissertation, I received support from many people that I would like to sincerely acknowledge.

First of all, thanks to my supervisors, Torsten Dahm and Frederik Tilmann, whose advice and continuous support have been very important for me in these years. Special thanks to Sebastian Heimann for his advice and encouragement: his office door was always open for discussing work and for advice about computer programming. Thanks to Joachim Saul for providing the earthquake bulletin data sets. Finally, thanks to Susanne Köster for being so helpful and patient whenever I struggled with the intricacies of German bureaucracy.

Friends and colleagues, whose moral support made the completion of this dissertation possible, should not be forgotten. Especially, I would like to mention Eleonora, Mehdi, Djamil, Francesco, Luigi, Simone, Gesa, Peter, Marius, Pouria, Anne, Jens, Eram, Tim, Ayleen, Toño, Sreeram, and Nasim. I really had a great time in Potsdam and Berlin, and I feel lucky to have met such wonderful colleagues and friends. I am greatly indebted to Mehdi, who has been a superb coach and to Djamil for his kind and continuous help - Thank you so much!

A big thank you goes to my parents, Ahmad and Nasrin, and my brothers, Behrang and Behzad, who have supported me all these years, even from thousands of kilometres away.

Last but not least, I would like to extend my deepest gratitude to Sara, who helped me withstand difficult times and put things in perspective during stressful times. You are the greatest - Grazie!

Contents

Chapter 1

Introduction

1.1 Motivation

Tectonic earthquakes, landslides and volcanic eruptions have caused numerous catastrophes throughout the history and contemporary records and yet continue to do so. These natural hazards have constantly put human lives and civilizations subject to a very high risk in many areas all over the world (Bilham, 2013). The risk due to these natural hazards is becoming even higher with the growing population of humans in the world. During the 20^{th} century, there was a fourfold increase in the world's population (Nichols and Beavers, 2008). In particular, the large number of inhabitants and infrastructures of the large cities located in areas such as along the subduction zones and near tectonic faults are susceptible to these natural hazards. Comprehensive plans for disaster and risk management can save millions of lives and prevent massive economical losses in these areas. Effective forecasting and early warning systems and timely assessment of the mentioned natural hazards are essential for this purpose. All these, however, rely on our understanding of the underlying physical causes, precursors and consequences of these processes. Thus, scientific research in these fields is crucial for a sustainable human life and development.

Seismic sources are processes that cause mechanical disturbance to the ground and release energy into the Earth in the form of seismic waves that propagate through the Earth to the recording seismographic sensors. There are different types of sources that produce seismic energy, such as earthquakes, explosions, human activities, ocean waves, and volcanic processes. The energy associated with these sources can have a tremendous range and, thus, can have a wide range of intensities and magnitudes.

Identifying the locations of seismic sources is usually the first task when analysing the seismic waves from uncontrolled sources. The seismic location inverse problem has a long history in seismology dating back more than a century, at least to Geiger (1921). In the last two decades, there has been a resurgence of interest in improving the ability to estimate reliable and precise seismic event locations for both earthquakes and explosions. One reason for this resurgence is the effort to improve event locations in global bulletins produced, for example, by the International Seismological Center (ISC), or the GFZ German Research Centre for Geosciences seismological infrastructure (GEOFON). Another reason is the need for improved seismic monitoring due to the signing of the Comprehensive Nuclear-Test-Ban Treaty (CTBT). Greater emphasis on locating small natural or man-made seismic events has been motivated by CTBT. Moreover, there has been growing recognition of the importance of the high-quality seismic locations in quantitative seismological analyses, such as seismic hazard analyses, fault-zone characterization, and Earth's deformation. Therefore, accurate estimation of seismic locations is critical since a wrong estimate of the seismic source location will result in wrong interpretations in the subsequent analyses. Besides, the locations

of seismic sources may reveal information about the geology near their hypocentres. For example, it is common in seismology to use earthquake seismicity to delineate faults in an area. Having accurate locations will therefore allow us to better understand the structures of the fault systems.

Seismic event location is not the only parameter of interest in (near) real-time source characterisation. The strength of the seismic source (i.e. seismic moment), seismic wave radiation pattern and source time function are parameters being of equal interest and partly assessed in this thesis. Seismic moment is a physical quantity (as opposed to seismic source magnitude) that measures the strength and energy release of a seismic source. In fact, the best way to quantify the size of a seismic event is to determine its seismic moment. Seismic moment rate function – often referred as source time function – is the variation of the amplitude of the seismic moment as a function of time. Source time function offers an integrated view of the seismic source process. Its duration and peak value are used to infer the global characteristics of the seismic event and in particular stress or strain drop (Tocheport et al., 2007; Vallée, 2013). Moreover, it contains the broad-band spectrum of the source process, therefore it can be used to calculate the radiated energy (Vassiliou and Kanamori, 1982), and to explore how the source spectrum behaves with respect to theoretical models (Aki, 1967, 1972). Source time function is therefore an efficient tool to quickly detect abnormal seismic events such as destructive tsunami earthquakes and nuclear explosion tests. From a practical point of view, their properties can also be studied to understand the influence of the seismic source on the strong ground motions generated by earthquakes. Finally, a consistent catalogue of source time functions will provide important information in understanding the physics and mechanics of seismic source processes.

The main motivation of this thesis is to contribute towards an improved routine source parameter estimation by combining some advanced seismological methods. One of the goals of this project is to achieve substantial improvements in global seismicity catalogues through better use of regional data (epicentral distances less than $\sim 20^{\circ}$). The research also affords to locate smaller seismic events (with magnitude $M \leq 4.5$) in global bulletin data sets more accurately, which is motivated by efforts to reduce magnitude thresholds in global monitoring systems. This would be made possible by better seismic travel-time models of crust and uppermost-mantle. An innovation of this project is to combine advances in seismic travel-time models and multiple-event location techniques to obtain better hypocenter localization in global bulletin data sets. In the scope of this thesis, the computational demands of the seismic source location is also fulfilled through the development of a new software package, which is being made available to the community as an integrated tool. Furthermore, a step is made in this work to develop a stable and reliable method to determine seismic source time function and to ultimately implement this method as a routine application, especially for seismic sources with uncommon rupture or energy release (e.g. nuclear explosions).

The overall concepts of the methods are based on various previous studies. As described in the following section, several theoretical and technical innovations have been made and put together to better localise and characterise seismic sources, namely in details on how the biasing effects of the unmodelled velocity structure is reduced, how the inherent non-linearity of the earthquake location problem is addressed, how a near real-time relative location can be done, and how the seismic source time function is parametrised. The following parts of this chapter give details on more specific contributions of this dissertation and the addressed questions therein.

1.2 Research questions and outline

1. A proper solution to the seismic location inverse problem requires knowledge of the dominant factors causing uncertainties of seismic locations, which are: measurement errors of seismic arrival times (picks), modelling errors of computed travel times, and non-linearity of the earthquake location problem. The latter is only relevant for linearised, least-square solutions; direct, global-search methods do not require linearisation of the earthquake location problem, and as such they are not affected by errors due to non-linearity and multi-modal object function. Among the other two groups of errors, that are relevant for both linearised and non-linear methods, modelling errors of calculated travel times lead to systematic biases in earthquake location. Hence, they are often much more significant than random, uncorrelated errors caused by arrival time picking, which average out given a sufficient number of picks. The first research question in this thesis is:

   - What approach can be adopted to lower the effects of these factors and improve the seismic locations in global bulletin data sets?

   In Chapter 2, I improved seismic location accuracy by applying a multiple-event location technique using deterministic travel-time corrections. The correction terms reduce the effect of spatially correlated residuals caused by 3-D velocity structure and, in consequence, can drastically reduce travel-time residuals at regional stations. Moreover, the algorithm has been adopted for probabilistic, non-linear, global-search location. The location procedure thus is less affected by local optima in the model space, and is less sensitive to outlier data. The latter becomes especially important if automatic picks are used in the location procedure, since in an automated picking process, occasional phase misidentification and picking errors are inevitable. After discussing the relocation method in details, the method has been applied to obtain improved locations of earthquake hypocentres at regional and teleseismic distances using two specific test regions: shallow to intermediate events in the Chilean margin, and shallow to very large depth earthquakes in the Tonga-Fiji subduction zone. For this purpose, both automatic and manual phase picks provided by the GEOFON bulletin data have been used.

   In Chapter 3, I developed a software package for relocating seismicity based on the algorithm described in Chapter 2. This package can be used for relocations in local, regional, and global scales. It has been designed as an easy-to-use command-line tool that is configured with a plain text file in a human-readable structured data format. Several subcommands for a number of routines, from input data preparation to exporting results, have been provided. The applicability and performance of the new relocation tool is demonstrated through examples in this chapter.

2. The use of a 1-D velocity model for seismic event location is often associated with significant mismatch between theoretical and observed arrival times (travel time residuals). Particularly for regional stations, where the velocity structure strongly deviates from the assumed 1-D model, large travel-time residuals are observed even for clear arrivals with small measurement uncertainties, indicating systematically biased locations. Since these residuals are normally not due to measurement errors but regional travel-time anomalies, arrival times at regional and near-regional stations do not match the location obtained with teleseismic picks, and vice versa. If the earthquake is weak and only recorded regionally, or if fast location based on regional stations is needed, the location may be far off the corresponding teleseismic location. This gives rise to the next question:

- How can the use of travel-time correction terms be extended to improve the routine location of lower-magnitude events or to obtain more reliable location in rapid solutions?

In Chapter 4, I investigated the potential of the relocation algorithm presented in Chapter 2 to be integrated to near real-time processing to locate new seismic sources with the accuracy of a reference catalogue with accurately known or high-resolution locations. For this purpose, a near real-time location process has been simulated and tested. In this simulation, I utilized locally stored ISC-EHB bulletin data set (Weston et al., 2018) as a reference catalogue and a set of ground-truth events as validation data, which I relocated relative to the base catalogue. It has been demonstrated that applying the proposed technique significantly reduces the bias in routine locations and enhance the ability to locate the lower magnitude events using only regional arrival data.

3. The steady march of technical progress in global monitoring system has provided first for the rapid determination of epicentre location, magnitude, focal mechanism, and depth of seismic sources. All of these parameters determined in near real-time describe a seismic source as a point source or an overall average in space and time. Although these parameters provide required information on seismic sources, in some cases, especially in the scope of rapid hazard assessment and tsunami early warning, more details about temporal evolution of the seismic source process are of great importance. This gives rise to the need for adding a new source parameter to those that are determined in near real-time. In this context, a promising approach to better characterise the seismic source would be to determine the moment release of the seismic source as a function of time; this is called the source time function or the seismic moment-rate function. On the other hand, we do not know the shape of source time function *a priori*. Therefore, the main questions in this regard are:

   - How should the seismic source inverse problem be recast to retrieve the source time function? What is an efficient parametrisation of the source time function to better resolve its complexities and determine its actual shape?

   In Chapter 5, it has been tried to answer to above questions with developing a more flexible and yet reasonably efficient inversion technique that can be systematically applied to moderate-size seismic events, also to seismic sources with unusual long or short durations with overshoot signals. I presented an inversion method for source time function estimation from a set of teleseismic body-wave records directly through waveform fitting. The parametrisation of the source time function using orthogonal basis functions allowed to capture the complexities of the source time function with satisfactory resolution. Moreover, to overcome the trade-off between the seismic source depth and the shape of the source time function, the method has been adopted for a simultaneous inversion of source time function and hypocentre depth using time windows appropriate for the direct P phase and the associated depth phases (pP, sP) needed for accurate source depth determination. The method has been applied to determine an abnormal seismic event, the 2017 North Korean nuclear explosion test, using high-frequency beam waveforms calculated at several small-aperture seismic arrays. The inversion outputs have been then compared with the results of other independent studies and the implications have been discussed including the impact on seismic moment and magnitude estimates.

In Chapter 6, the concluding remarks of this thesis and the outlook for the future research have been mentioned.

1.3 Author's contributions and publications

The articles published during the course of this thesis and my contributions therein are listed below:

- Chapter 2:

  Nooshiri, N., Saul, J., Heimann, S., Tilmann, F., and Dahm, T. (2016): Revision of earthquake hypocentre locations in global bulletin data sets using source-specific station terms. *Geophysical Journal International*, 208(2):589–602. doi:10.1093/gji/ggw405.

  - I developed and tested the method, wrote up the manuscript and made the figures and implemented comments from all co-authors. The contribution of the other authors consisted of supervising the project (TD, FT, and SH), providing data sets (JS), and providing feedback on the manuscript (all co-authors).

- Chapter 3:

  Nooshiri, N. (2019): SCOTER - multiple-earthquake location by using static and source-specific Station COrrection TERms. *Scientific Technical Report STR 19/05. GFZ German Research Centre for Geosciences*. doi:10.2312/GFZ.b103-19056.

  - I developed, tested and documented the method, prepared example test cases, made the figures, and wrote up the manuscript. This work is benefited from the comments, suggestions, and criticisms of my academic adviser, TD.

  Nooshiri, N., Heimann, S., Tilmann, F., Dahm, T., and Saul, J. (2019): SCOTER – software package for multiple-earthquake relocation by using static and source-specific station correction terms. *GFZ Data Services*. doi:10.5880/GFZ.2.1.2019.002.

  - This is the technical implementation of the relocation method elaborated on in Chapter 2. I developed and tested the software package. SH supervised the project. All co-authors provided suggestions and feedback on the design and functionality of the software.

- Chapter 4:

  Nooshiri, N., Saul, J., Tilmann, F., Heimann, S., and Dahm, T.: Toward near real-time relative event location using long-term archives of earthquake bulletins. *in preparation for submission to Journal of Seismology.*

  - I developed and tested the method, wrote up the manuscript, made the figures and implemented comments from all co-authors. The contribution of the other authors consisted of supervising the project and providing feedback on the manuscript.

- Chapter 5:

  Gaebler, P., Ceranna, L., **Nooshiri, N.**, Barth, A., Cesca, S., Frei, M., Grünberg, I., Hartmann, G., Koch, K., Pilger, C., Ross, J. O., and Dahm, T. (2018): A multi-technology analysis of the 2017 North Korean nuclear test. *Solid Earth*, 10(1):59–78. doi:10.5194/se-10-59-2019.

  - This is an application of the simultaneous inversion of source time function and depth that I developed and presented in Chapter 5. I did the depth and seismic moment-rate function inversion and contributed to moment tensor inversion. I also contributed to the related text and figures as well as the discussions on the seismological results.

Chapter 2

Revision of earthquake hypocentre locations in bulletin data sets using travel-time corrections: proof of concept

The material presented in this chapter has been published as:

Nooshiri, N., Saul, J., Heimann, S., Tilmann, F., and Dahm, T. (2016): Revision of earthquake hypocentre locations in global bulletin data sets using source-specific station terms. *Geophysical Journal International*, 208(2):589–602. doi:10.1093/gji/ggw405.

Abstract

Global earthquake locations are often associated with very large systematic travel time residuals even for clear arrivals, especially for regional and near-regional stations in subduction zones because of their strongly heterogeneous velocity structure. Travel time corrections can drastically reduce travel-time residuals at regional stations and, in consequence, improve the relative location accuracy. We have extended the shrinking box source-specific station terms (SSST) technique to regional and teleseismic distances and adopted the algorithm for probabilistic, non-linear, global-search location. We evaluated the potential of the method to compute precise relative hypocentre locations on a global scale. The method has been applied to two specific test regions using existing P- and pP-phase picks. The first data set consists of 3103 events along the Chilean margin and the second one comprises 1680 earthquakes in the Tonga-Fiji subduction zone. Pick data were obtained from the GEOFON earthquake bulletin, produced using data from all available, global station networks. A set of timing corrections varying as a function of source position was calculated for each seismic station. In this way, we could correct the systematic errors introduced into the locations by the inaccuracies in the assumed velocity structure without explicitly solving for a velocity model. Residual statistics show that the median absolute deviation (MAD) of the travel time residuals is reduced by $40\% - 60\%$ at regional distances, where the velocity anomalies are strong. Moreover, the spread of the travel time residuals decreased by $\sim 20\%$ at teleseismic distances ($> 28°$). Furthermore, strong variations in initial residuals as a function of recording distance are smoothed out in the final residuals. The relocated catalogues exhibit less scattered locations in depth and sharper images of the seismicity associated with the subducting slabs. Comparison with a high resolution local catalogue reveals that our relocation process significantly improves the hypocentre locations compared to standard locations.

2.1 Introduction

The use of a 1-D velocity model for seismic event location is often associated with significant travel time residuals. Particularly for regional stations in subduction zones, where the velocity structure strongly deviates from the assumed 1-D model, residuals of up to ±10 s are observed even for clear arrivals, resulting in systematically biased locations. Since these residuals are normally not due to measurement errors but regional travel time anomalies, arrival times at regional and near-regional stations do not match the location obtained with teleseismic picks, and vice versa (Fig. 2.1). If the earthquake is weak and only recorded regionally, or if fast location based on regional stations is needed, the location may be far off the corresponding teleseismic location.

A proper solution to this problem requires knowledge of the dominant factors causing uncertainties of earthquake locations, which are (Pavlis, 1986; Husen and Hardebeck, 2010): assumed velocity model-dependent errors of calculated travel times, timing and picking errors of seismic phase arrival times, and inherent non-linearity of the earthquake location problem. The latter is only relevant to linearised, least-squares location methods. Direct, global-search location algorithms are not affected by errors due to non-linearity of the inverse problem since they do not involve linearisation of the problem. The other two groups of errors are relevant for both linearised and non-linear methods. Inaccuracies in the assumed velocity model introduce systematic bias (Billings et al., 1994), and hence they are often much more significant than random, uncorrelated errors caused by arrival time picking, which average out given a sufficient number of picks. Indeed, the accuracy of an earthquake location depends on the modelling errors of calculated travel times. Fig. 2.1 shows how the location of an earthquake in the Chilean subduction zone is biased due to inaccuracies and limitations in the assumed velocity model. Note the discrepancy of more than 50 km between the epicentral solutions based on teleseismic and regional arrival times, respectively.

There are different strategies that can be adopted to lower the effects of unmodelled velocity structure and improve the seismic locations. One approach is to use tomographic velocity models to predict the travel times of seismic phases more accurately. Several studies have demonstrated improved travel-time prediction accuracy using a global 3-D model (Smith and Ekström, 1996; Antolik et al., 2001; Chen and Willemann, 2001; Myers et al., 2015). However, although the obtained velocity information provides enhanced absolute hypocentre locations by reducing the biasing effects of large-scale velocity structure, usually only a smooth model can be obtained, which cannot effectively account for small-scale velocity heterogeneities, particularly when applied to global earthquake location. In addition to improved velocity models, several studies showed that applying corrections to travel-time predictions to account for travel-time bias can lead to improvement in location. Travel-time corrections can be computed empirically based on ground-truth (GT) event locations. Travel-time residuals for the GT events are calculated relative to a velocity model and then these calibration points are statistically interpolated to form continuous travel-time correction surfaces (Schultz et al., 1998; Myers and Schultz, 2000). Myers and Schultz (2000) demonstrated that applying such empirical corrections significantly reduces the bias in location and improve the ability to locate the lower magnitude events. In another technique the travel-time corrections can be refined by determining a set of station corrections. The use of station corrections along with differential arrival times is the basic concept behind most of the relative location techniques (e.g., Douglas, 1967; Jordan and Sverdrup, 1981; Pavlis and Booker, 1983; Poupinet et al., 1984; Got et al., 1994; Richards-Dinger and Shearer, 2000; Waldhauser and Ellsworth, 2000; Myers et al., 2007). When the travel-time-prediction errors are dominated by the biasing effects of lateral velocity heterogeneities, the relative location

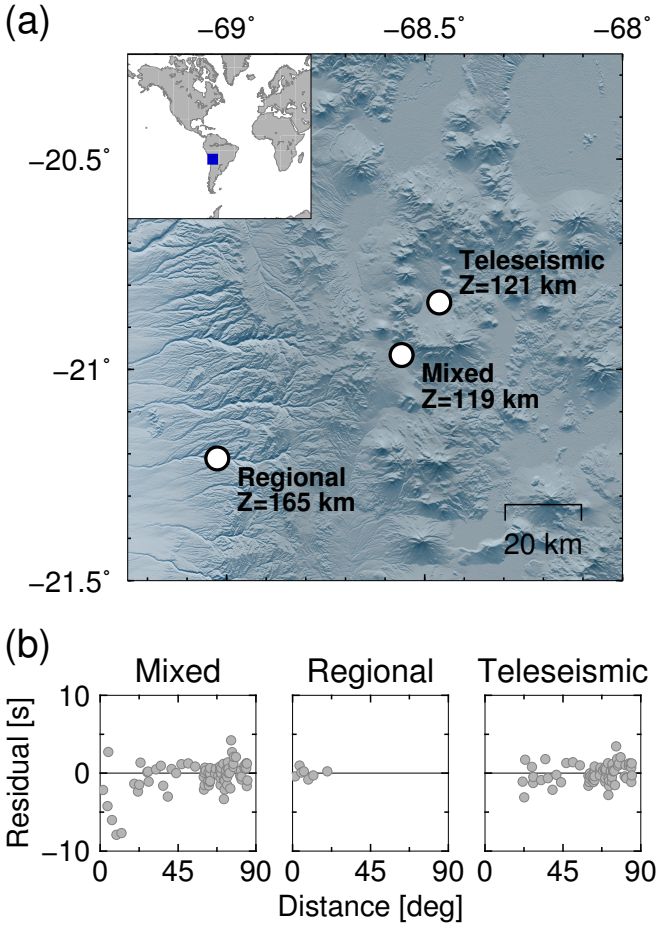

Figure 2.1: Example illustrating an earthquake that is differently located using either regional or teleseismic arrival times. Note the discrepancies of more than 50 km horizontally and ∼45 km vertically between regional and teleseismic epicentres. (a) Map view, and (b) Travel-time residuals corresponding to the three solutions. Combining regional and teleseismic stations results not only in another different hypocentre location but also large travel time residuals at regional stations. Travel times have been calculated using the global 1-D velocity model ak135.

techniques can be highly effective for events within a localized region, provided the local source region is small compared to the heterogeneity. This is because nearby events share common ray-paths to network stations and therefore the residuals to a given station are spatially correlated among these events.

The double-difference algorithm (Waldhauser and Ellsworth, 2000) and the shrinking box source-specific station terms (SSST) method (Richards-Dinger and Shearer, 2000; Lin and Shearer, 2005) are both techniques that can improve the relative location accuracy among nearby events in the case of distributed seismicity. Despite differences in how the methods work, they solve the same underlying problem. Synthetic tests have shown that these methods yield very similar results for the relative locations among nearby events when applied to identical data sets but that the shrinking box SSST is slightly better in terms of absolute location accuracy (Lin and Shearer, 2005). The shrinking box SSST has some further advantages: since SSST technique separates the location part from the station correction calculation, any desired single-event location algorithm can be used, including L1-norm misfit measures or grid-search methods. Moreover, SSST is computationally more efficient for very large data sets (e.g., >400,000 events (Lin et al., 2007)), because large matrix inversions are not required (Lin and Shearer, 2006). Furthermore, large to small scales of velocity heterogeneity are handled through the shrinking box SSST approach.

In this study, the SSST method has been applied to obtain improved locations of earthquake hypocentres using existing P and pP phase picks at regional and teleseimic distances. We use this global SSST technique to relocate two different data sets: 3103 shallow to intermediate events in the Chilean margin; and 1680 shallow to very large depth (∼700 km) earthquakes in the Tonga-Fiji subduction zone. For this purpose, both automatic and manual phase picks provided by the GEOFON bulletin data have been used. GEOFON (http://geofon.gfz-potsdam.de/) is the seismological infrastructure operated by the GFZ German Research Center for Geosciences. Using real-time seismological data from their own broadband network GEOFON Data Centre (1993) and many open and selected restricted station networks around the world, GEOFON determines rapid automatic location estimates for all globally recorded and most larger regional earthquakes, and provides manually revised solutions for at least the largest earthquakes.

2.2 Relocation method

Travel time residuals to a single seismic station contain the effect of unmodeled 3-D velocity structure and random errors of arrival time measurements. The latter is uncorrelated and the former is spatially correlated in the source region because close-by events will be affected by similar structure. The goal of the SSST method is to reduce the effect of spatially correlated residuals caused by 3-D velocity structure (Lin et al., 2007). By using this technique, a set of station corrections is computed iteratively for each receiver. Therefore, the time corrections for each station vary as a function of source position. The calculated station terms are added to the travel times computed from the velocity model to take unmodeled structure into account. Thus, the travel time residual misfit function to be minimized is a function of station terms in addition to earthquake hypocentre parameters:

$$\phi\left(t_i, \boldsymbol{x_i}, s_{ij}\right) \propto \|T_{ij}^{obs} - t_i - \tau_j\left(\boldsymbol{x_i}\right) - s_{ij}\|_p, \tag{2.1}$$

where t_i and $\boldsymbol{x_i}$ are the origin time and location of the i-th event respectively, s_{ij} is the SSST for the i-th event at the j-th station, T_{ij}^{obs} is the observed arrival time of the i-th event at the j-th station, $\tau_j(\boldsymbol{x_i})$ gives the model-predicted travel time from event location $\boldsymbol{x_i}$ to the station j, and $\|.\|_p$ denotes the p-norm. An additional constraint is imposed that the station terms must only be varying slowly as a function of source position. This is a coupled system of equations that can be solved by using a two-step iterative procedure of Frohlich (1979). In each iteration, first, ϕ is minimized with respect to hypocentre parameters (t, $\boldsymbol{x}$) while the station terms s are held fixed. Then the station terms are updated by appropriate averaging of residuals while holding the hypocentres fixed.

The basic algorithm is described by the following steps (Richards-Dinger and Shearer, 2000):

1. First, all the earthquakes are located with the actual arrival times.
2. Then, an SSST is calculated for each source-receiver pair as the mean of the residuals from at most N neighbouring events which are located within a sphere of radius R_{max} around the target event and have picks at the station in question.
3. The original arrival time picks are corrected by the calculated SSSTs ($T_{ij}^{'obs} = T_{ij}^{obs} - s_{ij}$).
4. Then, the earthquakes are relocated with these corrected arrival times.
5. The above steps are repeated iteratively.

As mentioned earlier, the so-called shrinking-box SSST technique has been applied in this study. In this method, obtained station corrections vary smoothly as a function of earthquake source location in both position and depth, with the degree of smoothing determined by the number of neighbouring events N and cut-off distance R_{max}. The number N and cut-off distance R_{max} were set to case specific initial values in the first iteration and then were gradually reduced to predefined minimum values in the final iteration. In this study, we chose different values of N and R_{max} for different regions considering the seismicity and the extent of the study area. To relocate events in the Chilean margin (Tonga-Fiji subduction zone), the procedure started with 600 (400) neighbouring events and a cut-off radius of 350 km (450 km) and ended after 10 (7) iterations with 20 (12) nearby events and a maximum inter-event distance of 35 km (55 km). For intermediate iterations, N and R_{max} are set to values spaced evenly in logarithmic scale. In this way, large to small scales of lateral velocity heterogeneities have been modelled during the relocation procedure. It should be pointed out that the iterative approach described above provides good relative locations but does not allow to quantify the absolute location error.

Here, we adopted the SSST relocation procedure for the probabilistic, non-linear, global-search location method implemented in the software package NonLinLoc (Lomax et al., 2000). In a probabilistic framework, a solution to the earthquake location problem is achieved by constructing the *a posteriori* probability density function (*pdf*) and directly searching it to find optimal solutions (Lomax et al., 2009). The *a posteriori pdf* is formulated as a combination of independent states of information including prior information on model parameters obtained independently of data, information obtained from (uncertain) observations, and a *pdf* describing the uncertainty of the forward problem (travel time calculation). In NonLinLoc, the posterior *pdf* can be constructed by either least-squares, L2-norm (LS-L2) (Tarantola and Valette, 1982) or equal-differential-time (EDT) (Font et al., 2004; Lomax, 2005) likelihood functions. While the former seeks to best satisfy all of the observations simultaneously, the latter tries to achieve its highest value (lowest misfit) by satisfying the most pairs of observations and thus is much more robust in the presence of outliers (Lomax, 2005). Using the EDT likelihood function, the location *pdf* has the following form (Lomax, 2005):

$$pdf(\boldsymbol{x}) \propto k \left[\sum_{obs_a, obs_b} \frac{1}{\sqrt{\sigma_a^2 + \sigma_b^2}} \exp \left(- \frac{\{[T_{obs_a}(\boldsymbol{x}) - T_{obs_b}(\boldsymbol{x})] - [TT_{calc_a}(\boldsymbol{x}) - TT_{calc_b}(\boldsymbol{x})]\}^2}{\sigma_a^2 + \sigma_b^2} \right) \right]^N , \tag{2.2}$$

where T_{obs_a} and T_{obs_b} are observed arrival times and TT_{calc_a} and T_{calc_b} are calculated travel times for stations a and b. σ_a and σ_b are assigned errors for the two observations, k is a normalization factor and N is the total number of observations. The exponential term in eq. 2.2 has its maximum value at points $\boldsymbol{x}$ where the two differential times (the terms in the braces) are equal. Such points $\boldsymbol{x}$ best satisfy the two observations obs_a and obs_a. In general, sets of points $\boldsymbol{x}$ where the exponential is non-zero construct a finite width, curved surface in 3-D space. In eq. 2.2, since the sum taken over differential times of all pairs of observations is outside the exponential, the EDT likelihood function has its maximum value for those points $\boldsymbol{x}$ where the most pairs of observations are satisfied and, therefore, is less sensitive to outlier data (Lomax, 2005). Furthermore, Lomax et al. (2009) performed comprehensive tests with synthetic data comparing the EDT approach with the standard LS-L2 method in the presence of outlier data and incorrect velocity model confirming the robustness of EDT

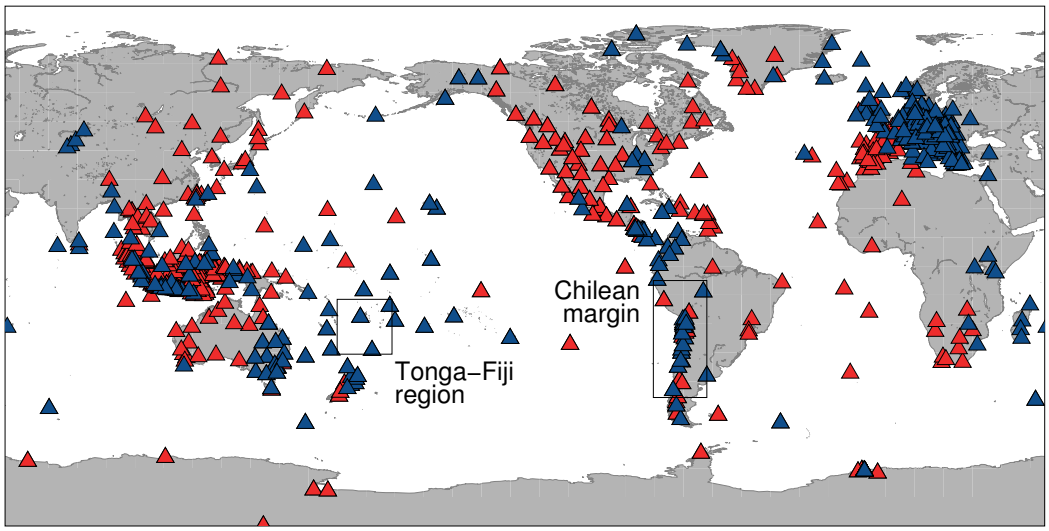

Figure 2.2: Distribution of seismic stations used to relocate 3103 Chilean events and 1680 earthquakes in the Tonga-Fiji region. Seismic stations recording at least one *pP* depth phase are shown by red triangles. Solid boxes indicate the boundaries of the study regions.

likelihood function. This becomes especially important if automatic picks are used in the location procedure, since in an automated picking process, occasional phase misidentification and picking errors are inevitable.

The resulting posterior *pdf* is typically irregular and multimodal but can be efficiently sampled by using the oct-tree algorithm (Lomax and Curtis, 2001), which is a stable, global-search method. It is based on a recursive subdivision and sampling of cells in 3-D space and importance sampling of the *pdf* with a high density of sampled cells in the areas of higher *pdf* values. In our study, we used the oct-tree method to sample the complex EDT *pdf* in 3-D space to find the maximum likelihood hypocentres of earthquakes. The location procedure thus is less affected by local optima in the model space. Moreover, it has been shown that the horizontal and vertical errors estimated by NonLinLoc are more realistic compared to those derived by linear algorithms (Lippitsch et al., 2005). In addition, 3-D velocity models can be used by NonLinLoc although we did not make use of this possibility in the present study.

We solved the spherical forward problem of calculating travel times of *P*- and *pP*-wave arrivals by assuming the global 1-D earth model ak135 (Kennett et al., 1995) also used for routine location by GEOFON.

2.3 Application to subduction earthquakes in the Chilean margin

2.3.1 Data set

Our first data set includes the arrival times of *P* and *pP* waves from 3103 events in the Chilean subduction zone. The earthquakes occurred from 2010 to 2015 between 15°S–45°S and 62°W–90°W. The depth of earthquakes ranges from 2 to 624 km and event magnitudes are between M3.3 and M8.4. The events were recorded at more than 400 global seismic stations. Fig. 2.2 shows the distribution of seismic stations recording the earthquakes used

in this study. The final data set consists of 125,236 P and 5,327 pP arrival time picks. Approximately two thirds of the Chilean catalogue had been revised and picked manually by GEOFON analysts. The events were originally located using *scautoloc*, the location module of the SeisComP3 package (https://www.seiscomp3.org/), producing an earthquake catalogue for all available station networks (hereafter referred to as GEOFON catalogue). Rather than using the hypocentres in the GEOFON catalogue as starting locations for our relocation procedure, we relocate all of the events with NonLinLoc as described above. These locations are referred to as single-event locations in the following section.

2.3.2 Relocation results and residual analysis

Based on the initial locations, first a set of P-wave static corrections was calculated for each station and then used as a starting point for the SSST calculation. Our tests show that this leads to some improvement in the absolute locations of the events because the shallow velocity heterogeneities beneath each station are accounted for by the static terms. For similar reason, the same static station terms were applied to both P and pP arrival times. Then, in an iterative manner, we estimated the P-wave SSSTs for each source-receiver ray paths to reduce the biasing effect of the true 3-D earth structure and then relocated the events by applying the obtained correction terms to P phases (at this step, we did not apply the same P SSSTs to pP phases due to their ray-geometries).

Fig. 2.3(a) shows examples of final calculated P-wave SSSTs (relative to the 1-D reference model ak135) for two particular regional stations (GE-LVC and GT-LPAZ) and a teleseismic station (US-GOGA). The station terms for each event recorded at the receiver are plotted at each event location. Spatial coherence of the pattern of the SSSTs indicates the existence of heterogeneities in the real velocity structure. Positive correction terms indicate low velocities and negative values reflect high velocity anomalies on the way of the seismic rays travelling from sources to the stations. Comparison between histograms of P travel time residuals at regional stations observed from locations before (Fig. 2.3b) and after (Fig. 2.3c) application of the computed SSSTs reveals significant reduction of their misfit. The median absolute deviation (MAD), mean (μ) and standard deviation (σ) of each distribution are indicated on each subplot. The MAD is a measure of spread that is less sensitive to outliers in the data set than the standard deviation and so often more appropriate in the presence of non-Gaussian errors. Applying SSSTs leads to the MAD reduction of 63% and 56% for stations GE-LVC and GT-LPAZ, respectively. The SSST values for teleseismic station are quite small, since in the lower mantle, where most of the teleseismic P-wave ray path resides, lateral heterogeneities are relatively weak and hence the velocity distribution is smooth.

The final relocated catalogue is shown in map view and in selected east-west cross sections in Fig. 2.4. Visual inspection of the SSST hypocentre locations in the cross sections presents a sharper image of the seismicity associated with the subducting slab compared to the non-linear, single-event locations. Particularly, a narrower Wadati-Benioff zone is imaged with fewer outlier locations. However, it should be noted that although SSST method reduces the relative errors among nearby events, the absolute locations remain biased since they require knowledge of the true 3-D velocity structure.

In most cases, accurately resolving depth is the most challenging part of earthquake location. Therefore, some indication of the reliability of an earthquake location method may be achieved by studying the overall distribution of depths in an earthquake catalogue. We compare the histograms of depth distributions from the original GEOFON catalogue, non-linear single-event locations, and our final SSST locations in Fig. 2.5. In the GEOFON catalogue, there is a sharp peak at 10-15 km depth, because for some events the depth is

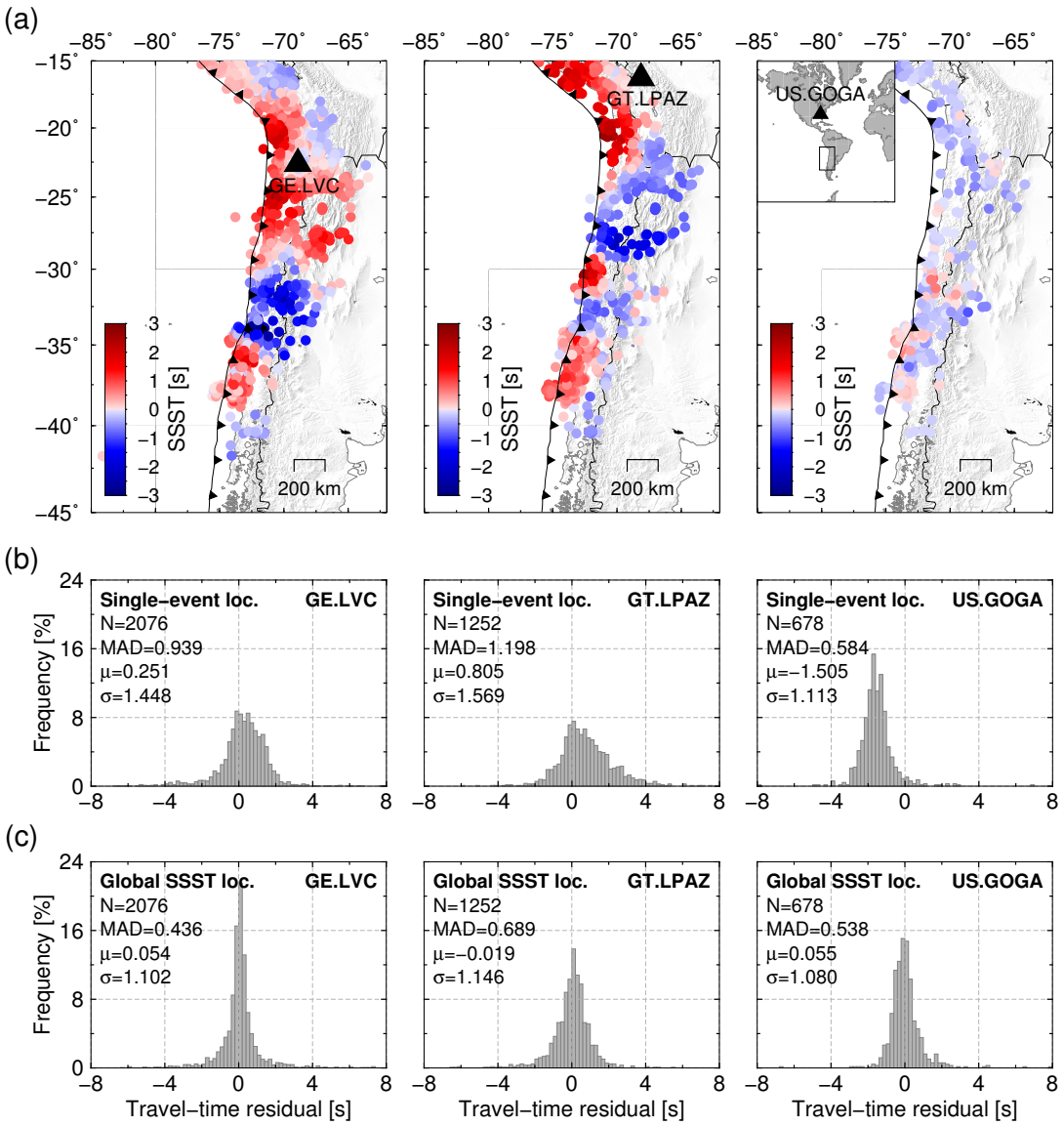

Figure 2.3: (a) Final *P*-wave source-specific station terms (SSSTs) for two selected regional stations and a teleseismic station (the right-most subplot) calculated from travel time residuals for events along the Chilean margin recorded by these stations. The SSST values are plotted at the event locations. (b) Histograms of the travel time residuals from single-event locations and (c) the SSST relocations for the stations shown in Fig. 2.3(a). The median absolute deviation (MAD), mean (μ) and sample standard deviation (σ) of each distribution are indicated on each subplot.

fixed to this level when it is poorly constrained. There is also a strong peak at 0-5 km depth in the single-event locations, indicating that there may be no or weak depth control and the maximum likelihood hypocentres calculated by NonLinLoc stuck at the surface. The depth distribution in our final SSST catalogue is more uniform and smooth, especially for shallower depths, with peaks likely reflecting actual trends in the seismicity. By looking at Fig. 2.4 we can identify the peak at 30-35 km with seismogenic zone activity, and the peak at a little over 100 km with the flat slab in this depth range.

Fig. 2.6(a) shows a comparison of the histograms of the *P*-wave travel time residuals for the single-event locations and the SSST locations. A substantial reduction of spread is observed after global SSST relocation. The MAD of the residuals drops from 1.144 s before relocation to 0.528 s after relative location; the root-mean-square (RMS) residual decreases from 1.506 s to 1.003 s. Fig. 2.6(b) presents the residuals before and after SSST relocation

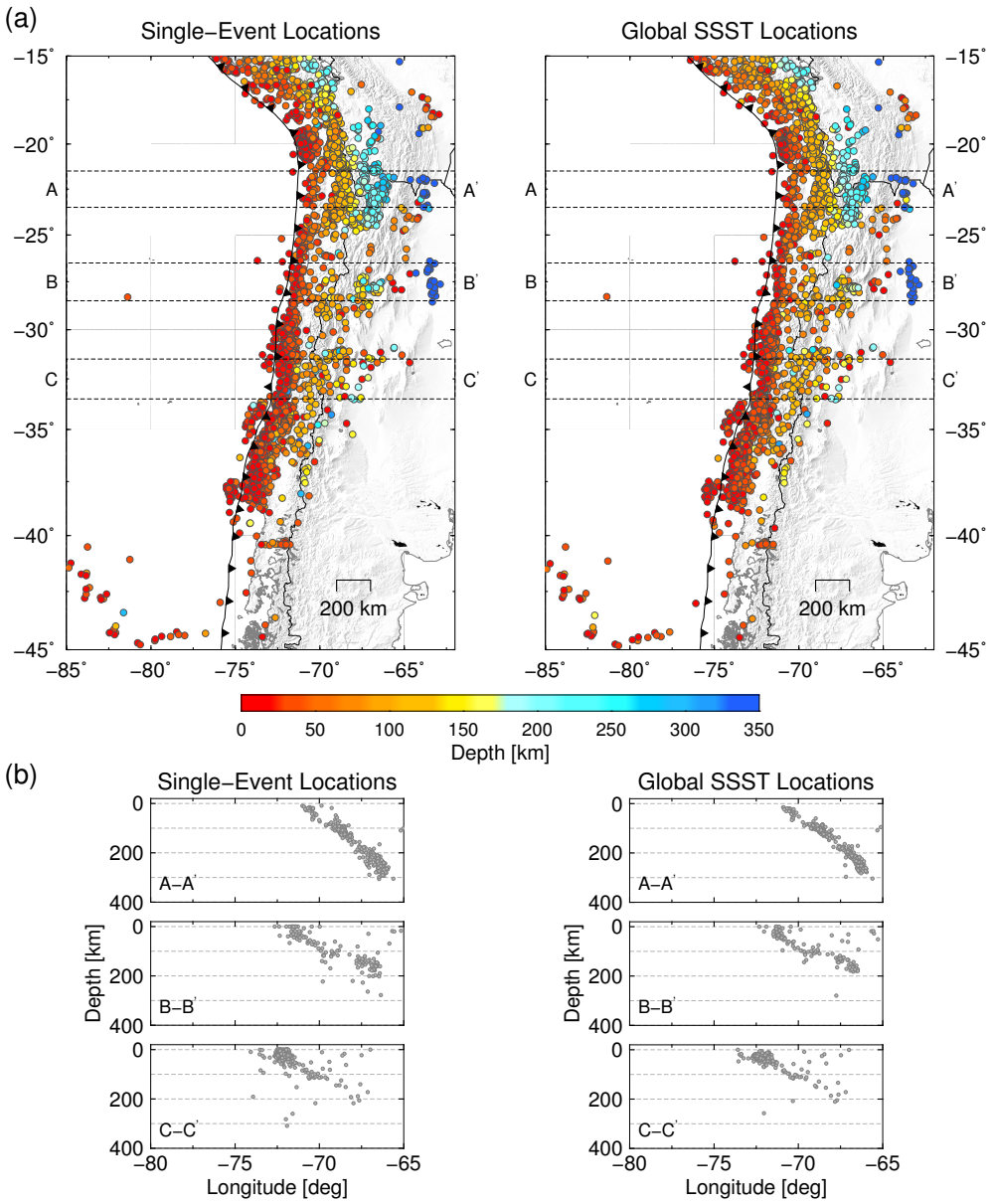

Figure 2.4: (a) Map view and (b) east-west cross sections of the 3103 earthquakes in the Chilean subduction zone (left) before and (right) after source-specific station terms relocation. Hypocentre locations in the left panels are from the single-event relocation. Boxes in the map views indicate the locations of the cross sections. Same events are shown in corresponding subplots.

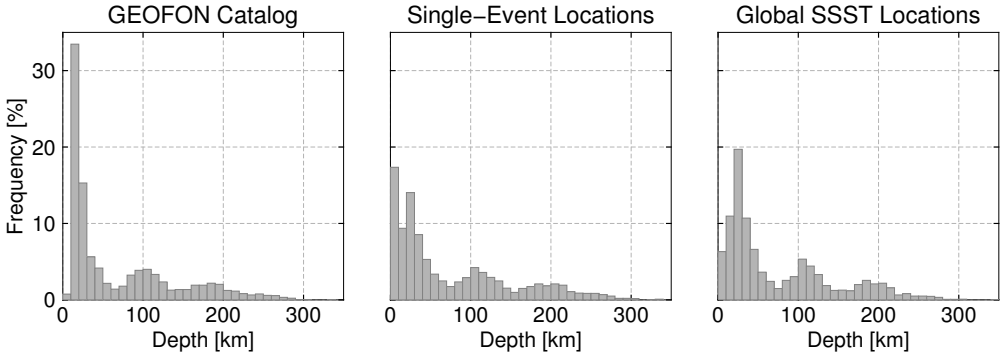

Figure 2.5: Histograms of depth distributions for different hypocentre locations indicated above each subplot.

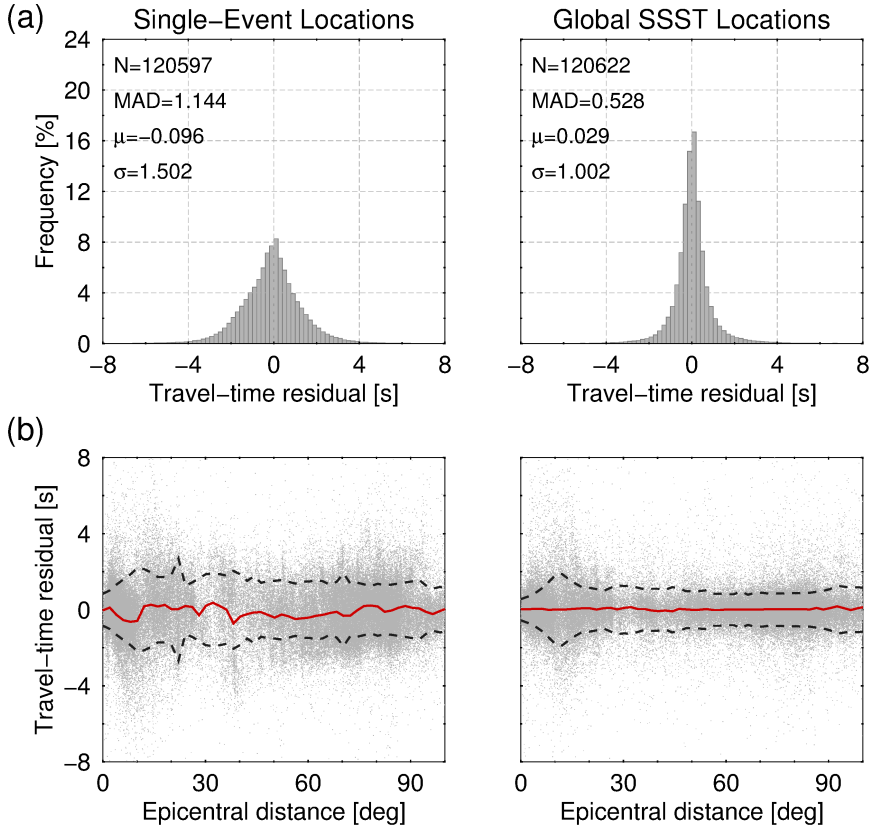

Figure 2.6: (a) Histograms of travel time residuals from single-event locations (left) and our global SSST relocations (right). (b) Residuals as a function of epicentral distance. Solid red lines and dashed black lines indicate mean and one standard deviation, respectively. Mean and standard deviation are computed within bins of 2° distance.

as a function of recording distance. Strong variations in initial residuals are smoothed out in the final residuals, especially in the regional distance range where the effect of lithospheric velocity anomalies is strong.

2.3.3 Comparison with high resolution earthquake locations

To assess the effectiveness of our relocation procedure, we compared our global SSST locations in two selected areas of the Chilean margin for which earthquake catalogues derived from a dense, local seismic network or by a temporary deployment of seismic sensors for aftershock studies are available. We consider these data sets as the most accurate locations available. They are the closest we can get to actual ground truth (GT) known locations, even though they do not fulfil the formal criteria for GT events (Bondár et al., 2004).

The first database is provided by the IPOC (Integrated Plate Boundary Observatory Chile) network (GFZ and CNRS-INSU, 2006) shown by triangles in Figs 2.7(a) and 2.7(b) (catalogue provided by Bernd Schurr as personal communication, 2015; a subset of this catalogue was published in Schurr et al. (2014)). Events roughly within the network and with magnitudes M≥4 are used as comparison dataset. None of the IPOC stations were used in the SSST relocation procedure, such that the data underlying both catalogues are (nearly) independent. The single-event locations (without applying any travel time corrections) and global SSST locations are visually compared with GT hypocentres in Fig. 2.7(a). Our results show the importance of the relocation procedure to constrain event depths when using only regional and teleseismic data. Quantitatively, the global SSST application improves the

reduction of the mean relative mislocation to 52% horizontally (Fig. 2.7b) and 55% vertically (Fig. 2.7c). We thus confirm that our relocation procedure using SSSTs results in global-network hypocenter locations that are more consistent with dense, local-network locations.

We used the aftershocks of the Maule earthquake (M_w8.8 on 27 February 2010) recorded by the dense temporary seismological network IMAD (International Maule Aftershock Deployment)(Beck et al., 2014) as a second reference set to further evaluate the validity of the global SSST results. The station spacing of ∼30 km provides a good resolution of hypocentral coordinates, including depth, for this database (catalogue published in Lange et al. (2012)), and none of the IMAD stations contributed to the SSST locations. Fig. 2.8(a) illustrates how the relocation procedure recovers the hypocentre locations better. Qualitatively, it can be seen that the global SSST improves the agreement with the local hypocentre locations and reduces systematic bias. Moreover, statistical measures of differences in hypocentre locations (Figs 2.8b and c) show a reduction of horizontal and vertical differences in location after applying SSST corrections.

2.4 Application to deep earthquakes in the Tonga-Fiji subduction zone

The Tonga-Fiji subduction zone is the most seismically active subduction zone worldwide and one of the best regions for imaging of the down-going slab and mantle wedge structure. It stretches from the North Island of New Zealand to the north-north-east and is about 2600 km long. The depth of earthquakes in the Tonga subduction zone ranges from very shallow (∼5 km) to very deep (∼700 km) and this region accounts for about two thirds of the globally recorded deep seismicity (>300 km depth). Many seismological studies identified complex morphology of the subducted lithosphere and anomalous mantle beneath the Tonga Trench, such as lateral mantle displacements (Gurnis et al., 2000), anomalously hot mantle (Chen and Brudzinski, 2001), and mantle upwelling (Pysklywec et al., 2003). The consequence of this structural complexity is large uncertainty in hypocentre locations in the Tonga-Fiji subduction zone listed in global catalogues like the GEOFON bulletin that use 1-D velocity models for computing earthquake locations.

2.4.1 Data set

We use 1680 events that occurred in the Tonga-Fiji subduction from 2010 to 2014 to evaluate the ability of global SSST method to relocate hypocentres in this region (Fig. 2.2). Body-wave magnitudes range between 4.1 and 7.5 with 685 events having M≥5. The events span a depth range of 5-682 km, making them well suited to investigate the effect of upper mantle and transition zone on global SSST solutions. The original data set is composed of 113,931 *P* and 1,726 *pP* phases included in the GEOFON bulletin. Less than 1% of phases recorded at local distances (0°-2.5°), ∼13% at regional and upper mantle distances (2.5°-28°), and ∼86% at teleseismic distances (28°-95°) (Fig. 2.9). Consequently, earthquake location inversion leads to large travel time residuals at the few near stations to better fit the abundance of distant data as in the first example. These large travel time residuals also could result from inadequate representation of heterogeneous upper-mantle structure in 1-D global velocity models. Like for the Chilean example case, instead of using initial locations from the GEOFON bulletin, the whole data set was first relocated by using the NonLinLoc program and then a set of static station terms was calculated based on these starting locations and applied before SSST relocation procedure.

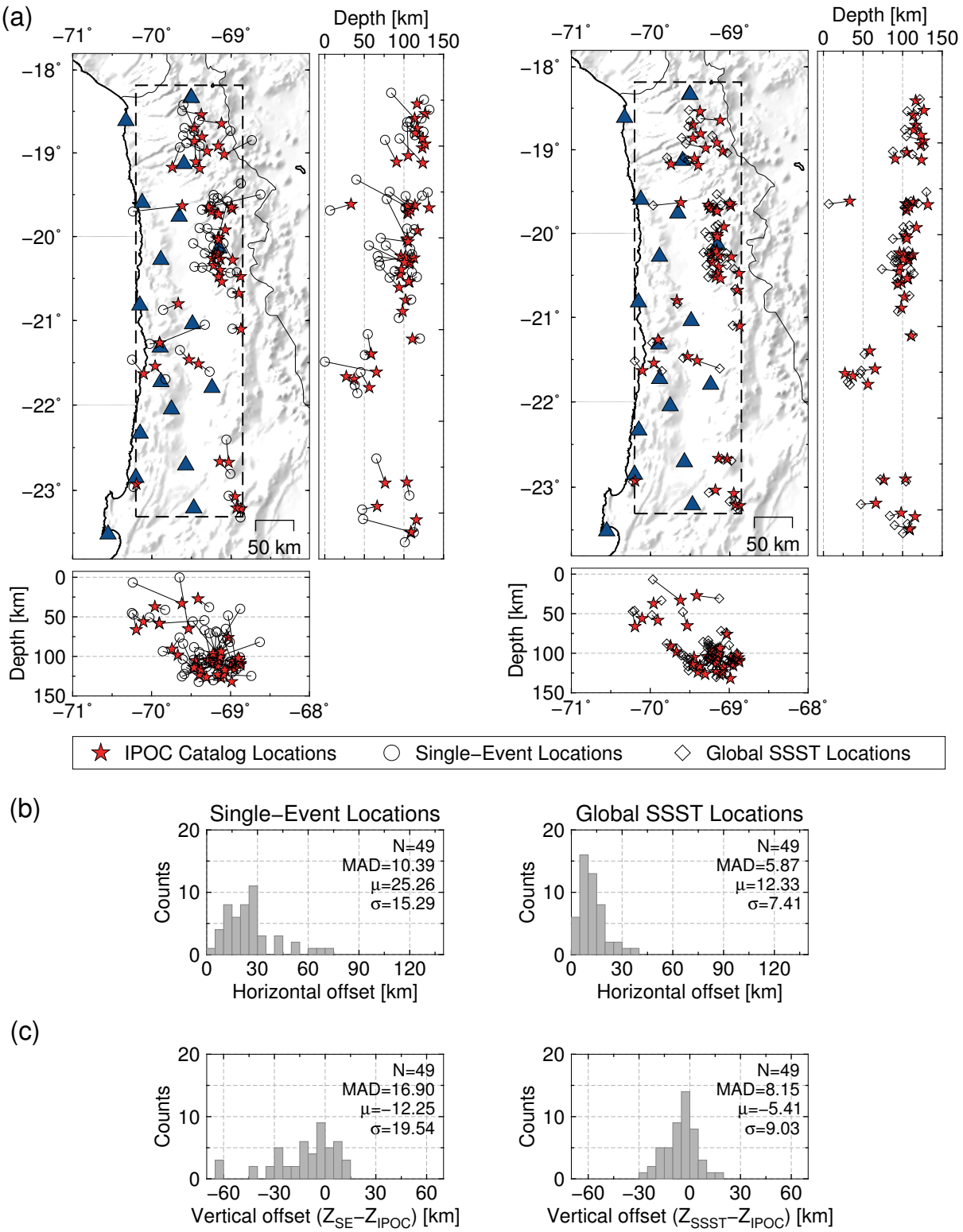

Figure 2.7: (a) Map views and cross sections of the seismicity in northern Chile, where high-resolution earthquake locations (stars) are available from the local IPOC network (triangles). Events roughly within the network (dashed box) and with magnitudes M≥4 are used as "ground-truth" (GT) events (in spite of not fulfilling formal criteria for GT events). Non-linear, single-event locations (left) and global SSST relocations obtained in this study (right) are compared with these GT events. Solid lines indicate mislocations between corresponding hypocentres. (b) Horizontal and (c) vertical differences between local hypocentres and single-event locations (left) and between local hypocentres and global SSST locations (right) are shown as histograms. MAD, mean relative mislocation (μ) and sample standard deviation (σ) of each distribution are shown in each subplot.

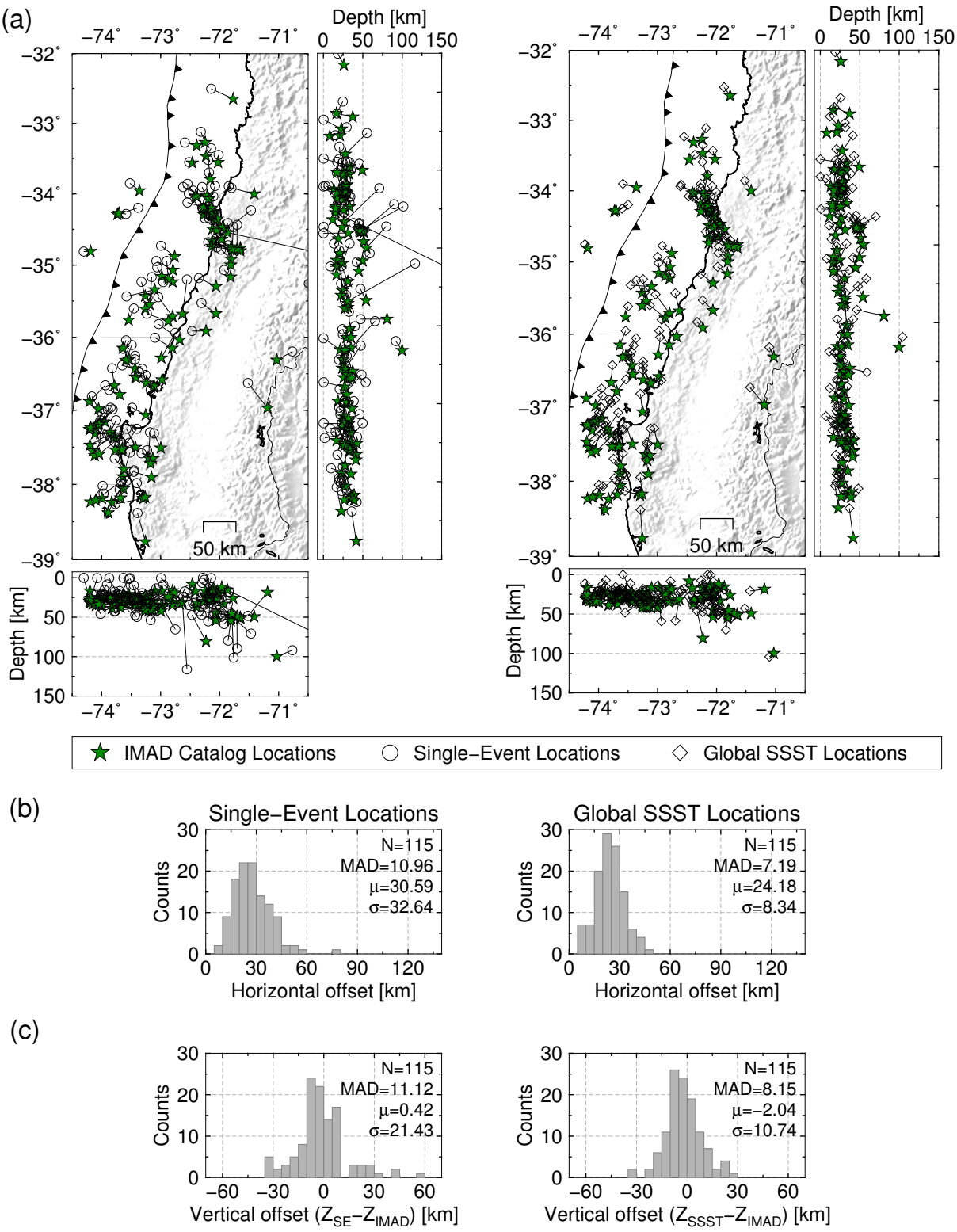

Figure 2.8: (a) Comparison of locations for 115 earthquakes in the 2010 Maule aftershock sequence (Lange et al., 2012) that were both locally and teleseismically recorded. The locations determined using local data (stars) are used as GT data set. Single-event locations (left) and our global SSST relocations (right) are compared with these GT events. Solid lines indicate mislocations between corresponding hypocentres. (b) Horizontal and (c) vertical differences between local hypocentres and single-event locations (left) and between local hypocentres and global SSST locations (right) shown as histograms.

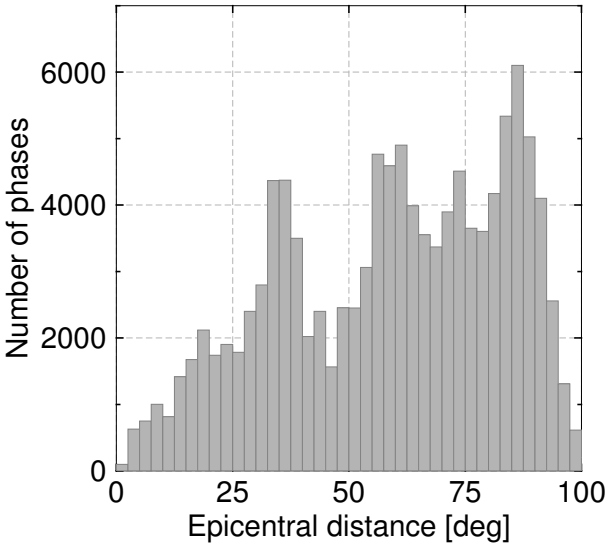

Figure 2.9: Histogram of number of recorded phases as a function of epicentral distance for earthquakes in the Tonga-Fiji region.

2.4.2 Source-specific station terms and statistical analysis of residuals

Using the algorithm described in section 2, the *P*-wave SSSTs were iteratively computed for each source-receiver pair recorded at a given station. The station term values are a smoothed version of the event-specific residual field for each station. Figs 2.10(a) and 2.10(c) show examples of final SSSTs for two different regional stations both of which show coherent patterns. The most obvious features in these figures are quite large positive SSST values at station II-MSVF (Fig. 2.10a) and large negative correction terms at station AU-NIUE (Fig. 2.10c) from sources located at shallow to intermediate depths. This can easily be interpreted by considering that these stations are located on opposite sides of the Tonga Trench. Along the Tonga-Fiji subduction zone, the Pacific Plate to the east is subducting beneath the Tonga Plate to the west. Several studies have determined tomographic models of this region, which delineate the Tonga Wadati-Benioff zone as a fast subducted slab with a slow mantle wedge structure in the back arc region (van der Hilst, 1995; Gorbatov and Kennett, 2003). Westward propagating seismic waves produced by earthquakes that occur at shallow to intermediate depths in the subduction zone will travel mostly through high attenuation and low velocity mantle wedge to arrive at the station II-MSVF (Fig. 2.10a). In contrast, seismic waves from the same source but propagating eastwards towards station AU-NIUE will pass through the high velocity slab (Fig. 2.10c). This effect is smaller for deeper earthquakes where the slab steepens up. Roughly similar SSST patterns are thus found for deep events (Fig. 2.10a and c).

Significant improvements to residual reduction are achieved by using our global relocation procedure (Fig. 2.10b and d). The MAD of the travel time residuals decreases by 58% and 51% at regional stations II-MSVF and AU-NIUE, respectively. For the whole catalogue a gradual reduction of travel time residual MAD from the 1680 events with iteration number in our global SSST calculation can be observed (Fig. 2.11). For comparison, the RMS residual decreased from 1.050 s to 0.912 s.

2.4.3 Relocated seismicity; close-ups and cross sections

The differences between the single-event locations and our SSST relocations are most obvious in some depth cross sections and close-ups of spatial clusters of earthquakes. Here, we select

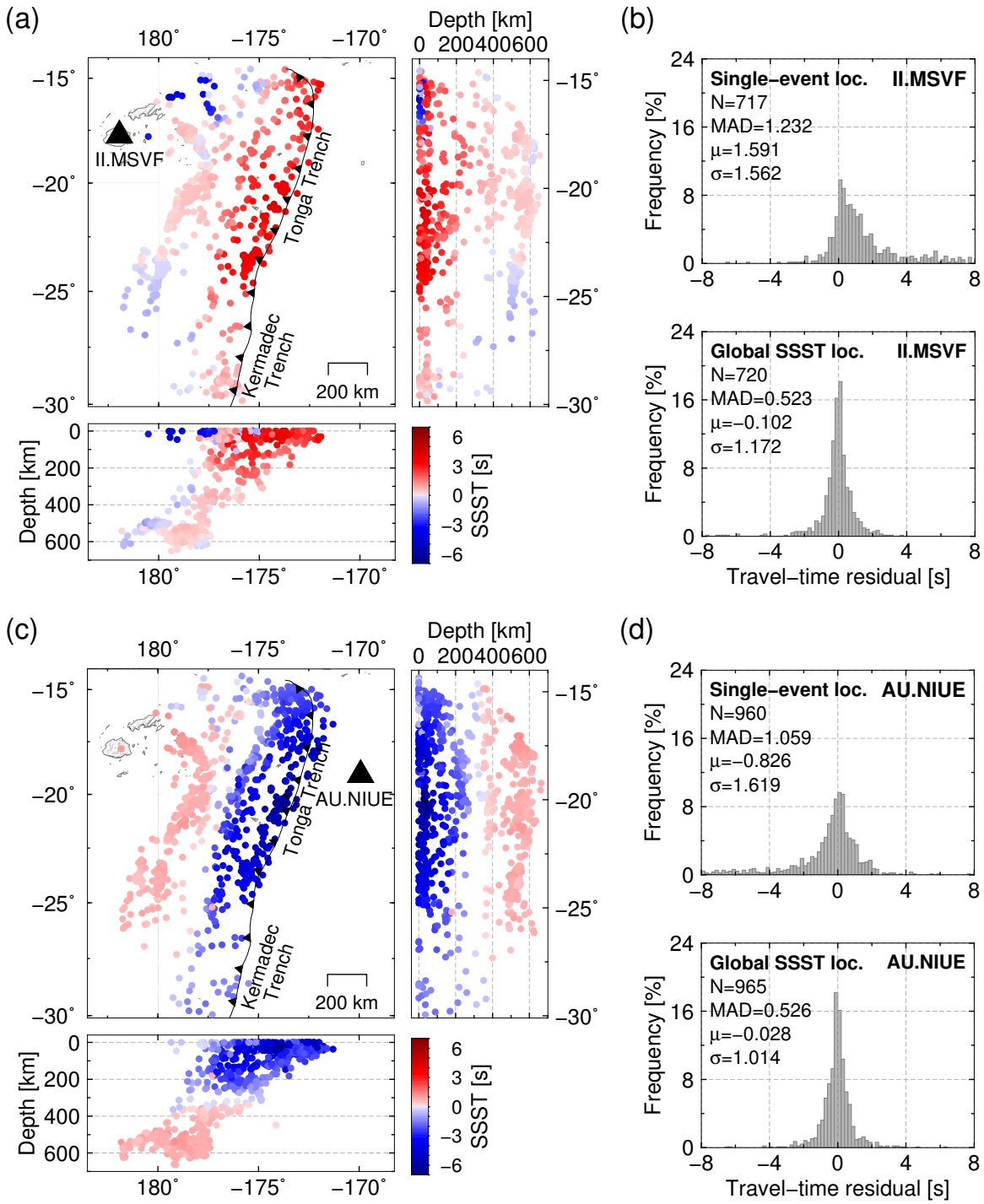

Figure 2.10: *P* SSSTs for particular stations (a) II-MSVF and (c) AU-NIUE, calculated from travel time residuals for earthquakes in the Tonga-Fiji subduction zone recorded by these stations. The SSST values are plotted at the event locations. (b) and (d) Histograms of the travel-time residuals for stations II-MSVF and AU-NIUE before and after global SSST relocation.

a few examples for detailed comparisons. Figs 2.12(a) and 2.12(b) show in map view and cross-sections a comparison of global SSST locations and single-event locations. Because we do not have access to any high resolution local catalogue of events in this region, we consider the spatial seismicity pattern as a qualitative measure of the improvement in global SSST relocations. Relative locations of the events appear to have visibly improved after the SSST relocation. This is visible in the decreased scatter in the new hypocentre locations, which

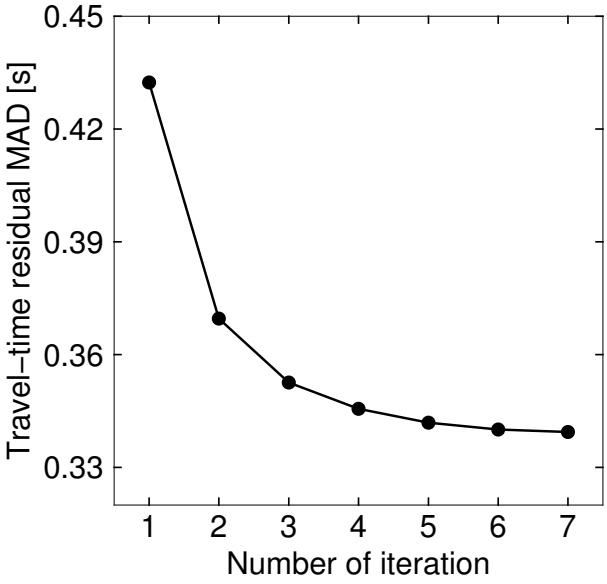

Figure 2.11: Reduction of travel time residual MAD for the 1680 events in the Tonga-Fiji subduction zone with iteration numbers.

better define the slab geometry. Additionally, events whose depths were poorly constrained by the single-event location and were thus previously stuck at the surface now have more plausible depths, removing the horizontal stripe artifacts at shallow depths seen in some cross sections for the single-event locations (Fig. 2.12b). At a smaller scale our SSST locations are improved compared to the single-event locations, as measured by the degree of spatial scattering and alignment of seismicity into planar features, in particular in the deep slab (Fig. 2.12c) where improved clustering can be observed.

Finally, we tried to simulate improvement in regional earthquake location that can be achieved by using pre-computed travel-time corrections. Events with at least 100 picks were selected and first located using only teleseismic observations (28°–95°). Then, they were located using only regional and near-regional phases (2.5°-20°) once without applying any time corrections and once refined with station terms determined by SSST method. These two sets of regional solutions are separately compared with teleseismic locations and shown in Fig. 2.13. Although it leaves room for improved locations, it shows that relocation solutions based on regional phases refined by pre-computed SSSTs are more consistent with teleseismic solutions. This promises the feasibility of using pre-calculated SSSTs to locate small magnitude events recorded regionally, or where fast location based on regional stations is needed.

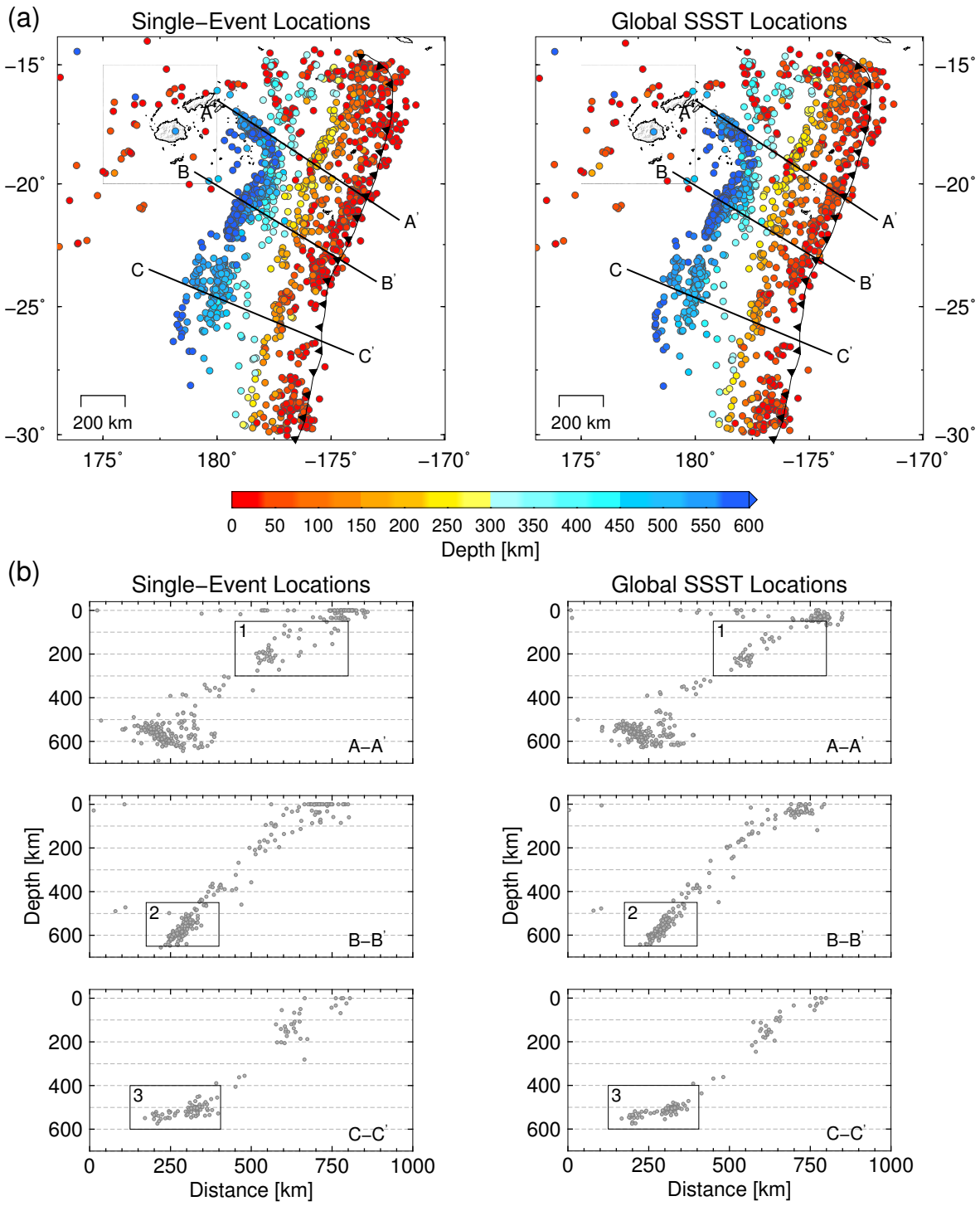

Figure 2.12: (a) Map view and (b) depth cross sections of the 1680 earthquakes in the Tonga-Fiji region determined using (left) single-event location method and (right) global SSST relocation procedure. Boxes in Fig. 2.12b include events shown in Fig. 2.12c. Same events are plotted in corresponding subplots. (c) Single-event (left) and global SSST (right) hypocentres of the events within the boxes shown in Fig. 2.12b.

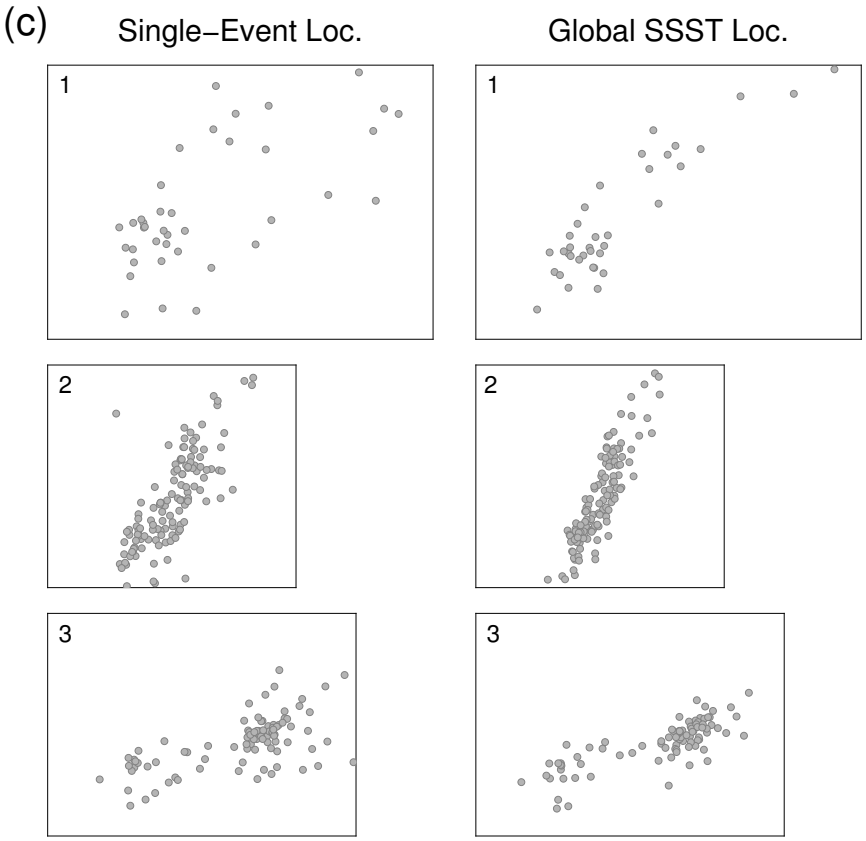

Figure 2.12: (continued)

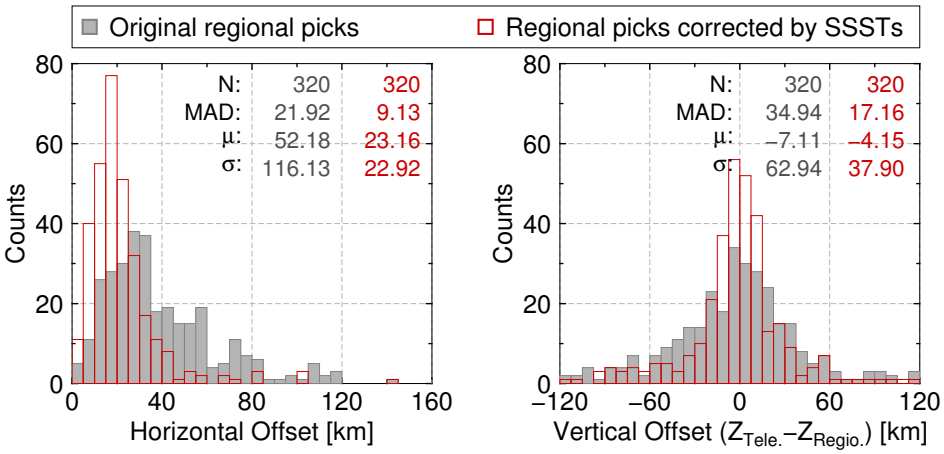

Figure 2.13: Horizontal and vertical relative mislocation of regional solutions without station terms and teleseismic hypocentres (gray) and regional locations corrected by the pre-calculated SSSTs and teleseismic hypocentres (red) are shown as histograms. The event mislocation is reduced when SSST corrections are applied.

2.5 Summary and conclusion

We have successfully implemented and tested a global SSST technique based on the procedures outlined in Richards-Dinger and Shearer (2000) and Lin and Shearer (2005). We adopted the method to a global setting and employed a non-linear, global-search method. We tested the method in two regions with strongly heterogeneous structure, relocating 3103 earthquakes along the Chilean margin and 1680 events in the Tonga-Fiji subduction zone using primary and depth phases recorded at regional and teleseismic stations. For our relocated catalogues of events in the Chilean margin (Tonga-Fiji subduction zone), average shifts relative to single-event locations are ∼18 (12) km in epicentres and ∼10 (13) km in depth. In general, the relocation procedure results in sharpening seismicity features associated with subducting slabs. Substantial improvement of focal depths is one of the highlights of our relocation results, demonstrating how effectively the global SSST approach can handle the model errors associated with regional structures such as subducting slabs, which otherwise can severely bias depth estimation. Furthermore, residual statistics show a strong reduction (∼40–60%) of travel time residual MAD at regional stations, reducing regional biases. In addition to better defining slab geometry by decreasing location scatter and reducing travel time residuals, comparison with high resolution earthquake locations reveal the potential of the SSST method to improve hypocentre locations on a global scale.

Our results represent the first step in an effort to relocate global bulletin data sets in a systematic way. In addition to applying the algorithm to larger catalogues of events and updating the catalogues on a rolling basis in the future as more data become available, some other improvements can be done to the extension of the relocation algorithm. It should be noted that our relocation results at this point represent our best estimates based on phase pick data alone. Further improvements are possible by extending the global SSST method and using differential times obtained via waveform cross correlation to achieve high precision earthquake locations (Shearer et al., 2005; Lin et al., 2007; Matoza et al., 2013). Our future work will focus on developing a global SSST algorithm using cross correlation methods applied to regional and teleseismic phases.

Since our relocation procedure is based on a global-search location method, it could be implemented for a global 3-D tomography model (e.g., LLNL-G3Dv3 model (Simmons et al., 2012)) to achieve further improvement in absolute location accuracy. Travel times from stations to the model spatial grid points can be computed once and saved as travel time grid files and retrieved during the location procedure.

One of the goals of earthquake relocation studies is to integrate the relocation algorithms to near-real-time processing to locate new events with the accuracy of the relocated reference catalogue (e.g., Got et al., 2002; Waldhauser, 2009). Rapid estimation of spatial location and origin time of a new event has particularly useful applications in earthquake and volcano monitoring and geohazard mitigation. For these purposes, relocation of events in near-real-time is a high priority. It is clear that a reprocessing of the whole catalogue is not feasible in this context. Instead, pre-computed SSSTs must be stored in a database at appropriate granularity. The generation of this database requires not only an *a priori* known high resolution catalogue of past seismicity and fast access to an archive of past seismic data, but also an automated SSST procedure that can update the precomputed terms at regular intervals. Moreover, as discussed by (Shearer et al., 2005), since relative location solutions are dependent on all nearby events, adding a new event to the catalogue would affect the locations of older events in the catalogue and the whole data set would need to be relocated for consistency.

Chapter 3

Revision of earthquake hypocentre locations in bulletin data sets using travel-time corrections: technical implementation

The material presented in this chapter has been published as:

Nooshiri, N. (2019): SCOTER - multiple-earthquake location by using static and source-specific Station COrrection TERms. *Scientific Technical Report STR 19/05. GFZ German Research Centre for Geosciences.* doi:10.2312/GFZ.b103-19056.

The software described in this chapter has been published as:

Nooshiri, N., Heimann, S., Tilmann, F., Dahm, T., and Saul, J. (2019): SCOTER – Software package for multiple-earthquake relocation by using static and source-specific station correction terms. *GFZ Data Services.* doi:10.5880/GFZ.2.1.2019.002.

Abstract

There has been growing recognition of the importance of the accurate seismic locations in quantitative seismological studies, such as seismic hazard analyses, fault zone characterization, and Earth's deformation. Accurate estimation of seismic locations is critical since a wrong estimate of the seismic source location will result in wrong interpretations in the subsequent analyses. We present SCOTER, an open-source Python program package that is designed to relocate multiple seismic events by using *P*- and *S*-wave *s*tation *co*rrection *ter*ms. The package implements static and shrinking-box source-specific station terms techniques extended to regional and teleseimic distances and adopted for probabilistic, non-linear, global-search location for large-scale multiple-event location. This program provides robust relocation results for seismic event sequences over a wide range of spatial and temporal scales by applying empirical corrections for the biasing effects of 3-D velocity structure. Written in the Python programming language, SCOTER is run as a stand-alone command-line tool (requiring no knowledge of Python) and also provides a set of sub-commands to develop inputs (dataset, configuration etc) and export results (hypocenter parameters, travel-time residuals etc) – routine but non-trivial tasks that can consume much user time. This package can be used for relocation in local, regional, and teleseimic scales. We describe SCOTER's functionality, design and technical implementation, accompanied by an overview of its use

cases. As an illustration, we demonstrate the applicability of this tool through two examples based on (1) a catalogue of several hundred events in the Arctic plate boundary region using regional and teleseismic arrival times and (2) a small dataset of low-magnitude seismic events recorded by dense, local stations at the western Iberia, central Portugal. The relocated datasets highlight the future potential for applying the SCOTER relocation tool to greatly improve the relative location accuracy among nearby events.

3.1 Introduction

Earthquake hypocentre location using observations of seismic phase arrival times is a classic inverse problem in seismology that has a rich history of conceptual and methodological advancements dating back more than a century. Catalogues of seismic locations are one of the most important and widely-used forms of seismological data providing important information on a number of seismotectonic problems, from the imaging of fault-zone structure to the improvement of seismic-hazard assessment. The degree to which these problems can be resolved depends on the quality of the seismic catalogues, which themselves turn on the reliability of the seismic location methodology.

Improvement in absolute seismic location accuracy is always limited by imperfect knowledge of 3-D variations in the Earth structure (Thurber, 1992; Thurber and Eberhart-Phillips, 1999). However, numerous methods have been developed yielding significant improvements to relative location accuracy through the joint relocation of pairs or clusters of events (Douglas, 1967; Jordan and Sverdrup, 1981; Got et al., 1994; Richards-Dinger and Shearer, 2000; Waldhauser and Ellsworth, 2000; Lin et al., 2007; Myers et al., 2007; Grigoli et al., 2016; Trugman and Shearer, 2017). Although initial catalogues are routinely determined from the phase picks and associated travel times of each event in isolation, relative relocation methods are primarily based on travel-time corrections refined by station terms for a group of events along with differential travel times of pairs of events observed at common stations. This formulation helps mitigate common-mode errors introduced by the biasing effects of unmodelled velocity structure.

Here we present and describe a computer program package designed for relocating seismicity using static and source-specific station terms, which we term SCOTER program and which we are making available to the community as an integrated software package. The program can greatly improve the relative location accuracy among nearby events by applying empirical corrections for the biasing effects of unmodelled velocity heterogeneities. Details about the relocation algorithm adopted in SCOTER are contained in Nooshiri et al. (2017). This package can be used for relocations in local, regional, and global scales. It is an easy-to-use command-line tool that is configured with a plain text file in a human-readable structured data format. SCOTER is an integrated and time-saving program that provides the user with several subcommands for a number of routines, from observation phase file preparation, to travel-time binary grid files computation, to exporting and plotting the relocation results. A strong motivation for designing SCOTER has been to provide a simple and flexible environment that shields the user from the complexities of programming and, therefore, can be used not only by seismologists but also other research geoscientists. SCOTER is written in Python programming language and runs on Linux and Mac OS platforms. As a demonstration of the new software functionality, we use SCOTER to relocate two earthquake data sets contained in the package to show location improvements of the algorithm relative to the typical seismic network locations. The manuscript is a concise but near-complete tour that aims to turn the reader into a productive SCOTER user very quickly. The package is licensed by GNU General Public License (GPL) and freely available to all users at https://gitext.gfz-potsdam.de/nooshiri/scoter.

3.2 Overview of software functionality

In a style similar to Unix shells, SCOTER is invoked as a command-line program by calling `scoter` from the Unix/Linux shell. Its command-line interface uses standard Unix/Linux conventions for its options and arguments. The command-line tool also offers several sub-

commands. The first command below gives a list of available subcommands and a brief summary of them, and the second one provides more information about a subcommand and its different option flags:

```
$ scoter --help
$ scoter <subcommand> --help
```

Options are recognized by their leading double-dashes (e.g. `--format`). In the program documentation, *required* and *optional* arguments are denoted by <···> and [···] punctuation marks, respectively.

SCOTER is part of the Pyrocko ecosystem (Heimann et al., 2017), an open-source community project that develops Python tools for a variety of geophysical tasks hosted by the GFZ Helmholtz Centre Potsdam. SCOTER uses many of Pyrocko's utility functions, as well as Python's numpy, scipy and matplotlib libraries, and relies on NonLinLoc code (Lomax et al., 2000) to do the actual event location part of the calculation, combining them into a more specialized piece of software. SCOTER's functionality can be summarized as follows:

- Parsing earthquake bulletin files in a few different formats (currently supports `QuakeML` and SeisComP3 `autoloc` formats) into NonLinLoc phase files.
- Creating 3-D binary grid files of seismic travel times.
- Parallelising the location calculation by distributing the input data across multiple processes to reduce the runtime of the execution.
- Performing separate location processes; single-event, static station term and source-specific station term (SSST) methods.
- Exporting results in convenient formats for statistical analysis and plotting.
- Diagnostic plots to visualise the performance of the algorithm.

There are several steps that should be taken when using SCOTER in a relocation project, from preparing required input files to exporting results. The basic work-flow can be summarised as follows:

- Setting up a project folder containing required input files.
- Setting up a configuration file for SCOTER.
- Running the program to relocate multiple events.
- Exporting the relocation results.
- Creating result plots for analysis and interpretations.

To use SCOTER with a specific data set, we suggest the folder structure shown in Figure 3.1. Details on required files and data formats, as well as data preparation, are given in the following sections by showing the applicability of the program through examples. Instructions on how to download and install SCOTER is given in Appendix A.1.

3.3 Input files and data

The fundamental input data for the SCOTER algorithm are phase pick data. It also requires input event and station data files that uniquely identify each seismic event (e.g. with an event identifier and possibly reference hypocentre) and each station (e.g. with a station code

```
project_dir/
├── config/ % contains configuration file
│   └── config_arctic.sf
├── data/
│   ├── phase/ % contains observation phase files
│   │   ├── eid_001.nll
│   │   ├── eid_002.nll
│   │   └── ...
│   └── events_arctic.pf
├── meta/ % contains station files
│   ├── stations-ims.sf
│   ├── stations-reg.sf
│   └── ...
├── time/ % contains travel-time grid files
│   ├── fescan.P.DEFAULT.time.buf
│   ├── fescan.P.DEFAULT.time.hdr
│   └── ...
└── run_dir/ % created at runtime, contains relocation results
```

Figure 3.1: Example folder structure when using SCOTER with a specific data set.

and optionally a network code). Additionally, a pre-computed travel-time grid file needs to be provided for each seismic phase considered. Previously determined station terms (either static or source-specific) can be included as a starting point for the location process. Finally, the various inputs to the program, along with algorithm control parameters, are combined in an input configuration file read by the SCOTER upon initial computation.

3.3.1 Observation phase files

The multiple-event relocation algorithm applied in the SCOTER program is adopted for probabilistic, non-linear, global-search location method implemented in the software package NonLinLoc (Lomax et al., 2000). The SCOTER tool relies on this back-end (external program) to do the actual event location part of the calculation (see Nooshiri et al. (2017) for more details). Therefore, the arrival-time data should be provided in the NonLinLoc observation phase file format (`NLLOC_OBS`) for the SCOTER. For each seismic event in the bulletin data set, a separate phase pick file needs to be provided whose name must include the corresponding event name (i.e. resource identifier of the event or eventID). The program offers a simple unified interface to handle and process earthquake bulletin files through `dump-obs` subcommand. The current implementation of SCOTER has the ability of parsing bulletin files in `QuakeML` and SeisComP3 `autoloc` formats into `NLLOC_OBS` phase files.

3.3.2 Station data files

An example of the format of the station data file is given in Table 3.1. It consists of a single line per station providing, in order, the network code, the station code, the latitude in degree (between $-90°$ and $90°$), the longitude in degree (from $-180°$ to $180°$), and the elevation in metre. Any line starting with **#** is considered as a comment line and ignored. The first column, i.e. network code, is optional and a given station data file has either four or five columns, although it is advised to use both network and station codes as sometimes station code alone may be ambiguous. The program can also be provided with multiple station files.

Table 3.1: The station data file

# NetCode (optional), StaCode, Lat, Lon, Elev [m]				
GE	MLR	45.4917	25.9437	1360.0
GE	SUMG	72.5763	-38.4539	3240.0
IM	ARCES	69.5348	25.5057	403.0
IM	SPITS	78.1777	16.3700	323.0
NO	NORES	60.7353	11.5414	302.0
NS	HOPEN	76.5084	25.0109	125.0
⋮		⋮		

3.3.3 Travel-time grid files

For each seismic phase considered, a travel-time grid file needs to be provided. Each grid file is stored with a small, simple ascii header file and a binary data buffer file. Both files have identical names except for the extension. SCOTER does not do the actual computation of the seismic travel times. A separate travel-time modelling code is required to do this. However, SCOTER provides some external software supports in order to make it simple to build a database of pre-calculated travel-time grids. The program includes a front-end tool, `grist`, to create and inspect travel-time grid files:

```
$ grist --help                    # list of available subcommands
$ grist <subcommand> --help       # subcommands with built-in help
```

Two modelling codes, including command-line interfaces, required for `grist` to build and store time grids are: (1) a modified version of the *iaspei-tau* routine (Snoke, 2009), and (2) *LLNL-Earth3D* computer code (Matzel et al., 2014; Simmons et al., 2015). The former computes travel times through a 1-D, spherically-layered earth model and the latter allows for fast calculation of 3-D seismic travel times through global-scale 3-D tomography model LLNL-G3Dv3 (Simmons et al., 2012).

The distribution of *iaspei-tau* code included in the SCOTER package is an extended version of the original routine (Steven Gibbons and Johannes Schweitzer, personal communication, 2018) that calculates the family of IASPEI standard seismic phases, such as *Pg*/*Sg*, *Pb*/*Sb*, *Pn*/*Sn*, *PKPab*, *PKPbc*, *PKPdf* etc. (Storchak et al., 2003). Currently, there are two variations of 1-D layered velocity model files that can be used. The first format is `tvel` ascii file format used by the IASPEI *ttimes* package (Kennett et al., 1995). This format has two comment lines, followed by lines composed of depth, V_p, V_s and density, all separated by white-space (Table 3.2). The second format is `nd` format for "named discontinuities" used by the *TauP* program (Crotwell et al., 1999). The file consists of two types of lines, those that specify velocity at a depth, and those that specify the name of a discontinuity. The former provides, in order, depth, V_p, V_s and density, and the latter specifies one of the three labels, *mantle*, *outer-core* and *inner-core* placed on a line by themselves (Table 3.3). It should be noted that, for both formats, only depth, V_p and V_s are required and the remaining parameter is not needed for travel-time calculations.

The user can create their own custom 1-D model in one of the valid formats to the program described before and use model from saved file to compute the travel times. Alternatively, a model name that is associated with a standard model as part of the program can be specified. Several standard models are included within the distributed package, such as ak135 (Kennett et al., 1995), iasp91 (Kennett and Engdahl, 1991), prem (Dziewonski and Anderson, 1981).

Table 3.2: The `tvel` velocity model file

```
ak135 - P
ak135 - S
   00.0   5.80    3.46    2.72
   20.0   5.80    3.46    2.72
   20.0   6.50    3.85    2.92
   35.0   6.50    3.85    2.92
   35.0   8.04    4.48    3.3198
   77.5   8.045   4.49    3.3455
  120.0   8.050   4.50    3.3713
  165.0   8.175   4.509   3.3985
  210.0   8.300   4.518   3.4258
  210.0   8.300   4.523   3.4258
  260.0   8.482   4.609   3.4561
  310.0   8.665   4.696   3.4864
            ⋮       ⋮
```

Table 3.3: The `nd` velocity model file

```
     00.0    5.80    3.2      2.6
     15.0    5.80    3.2      2.6
     15.0    6.80    3.9      2.9
     24.4    6.80    3.9      2.9
mantle
     24.4    8.111   4.491    3.381
       ⋮               ⋮
   2891.0   13.72    7.265    5.566
outer-core
   2891.0    8.065   0.000    9.903
       ⋮               ⋮
   5150.0   10.36    0.000   12.170
inner-core
   5150.0   11.03    3.504   12.760
       ⋮               ⋮
```

Following command gives a complete list of the built-in 1-D layered velocity models:

```
$ grist list-models-1D
```

Finally, 1-D model travel-time grid file for a specific seismic phase can be easily built by invoking the following subcommand given the epicentral distance range, depth range, a file prefix, and desirably a custom velocity model file or a built-in model name:

```
# 1-D model travel-time calculation
$ grist raytrace-1D <--phase=phase> <--model=name|filename>
↪ <--distances=Xmin:Xmax:deltaX> <--depths=Zmin:Zmax:deltaZ>
↪ <--prefix=file_prefix> [--out-dir=dir_name]
```

Travel-time grid files built through 1-D, spherically-layered earth models are used for multiple stations, meaning that the calculated arrival time at a specific station is a function of only source depth and source-receiver surface distance. As mentioned before, the program provides the user with an interface for station-specific travel-time calculation through the 3-D tomography model LLNL-G3Dv3 (Simmons et al., 2012), which is a global-scale model of the crust and mantle *P*-wave velocity with regional-scale details. It should be noted that computation of travel times through the 3-D model can take 0.1 to 1.0 seconds per grid node depending on complications due to ray multipathing and, therefore, creating a 3-D model travel-time grid file for a specific phase at a single station would be computationally expensive. If the user decides they need for 3-D travel times for a *P*-wave type phase (e.g. *Pg*, *Pb*, *Pn* etc) at a specific station, the command to create such grid files would be:

```
# 3-D P-wave model travel-time calculation
$ grist raytrace-3D <--phase=phase> <--slons=west:east:step>
↪ <--slats=south:north:step> <--sdepths=bottom:top:step>
↪ <--rloc=lat,lon> <--prefix=file_prefix> <--station=sta_code>
↪ [--network=net_code] [--rdepth=elev_km] [--out-dir=dir_name]
```

Table 3.4: The station correction terms file

```
# NetCode (optional), StaCode, Phase, StaTerm [s]
    GE    SUMG     P1    -0.6178
    GE    SUMG     S1     0.6345
    IM    ARCES    P1     2.1970
    IM    SPITS    P1    -0.8363
    IM    SPITS    S1    -0.3579
    NS    HOPEN    P1    -0.4289
    NS    HOPEN    S1    -1.1252
          ⋮              ⋮
```

In the command above, `--slons`, `--slats` and `--sdepths` options specify longitude, latitude and depth (in kilometres) ranges of the source region, respectively. These values help the program define the size, origin and node spacing of the location search grid. For a specific *P*-wave type phase given via `--phase` option, seismic travel times are calculated from all the nodes in the 3-D grid (i.e. potential source points) to the receiver specified by the `--rloc` option. In this case, since the grid file is created for a specific station, the station code and optionally the network code (if it is available in the station file) are also needed in addition to the file prefix to help the program name the output files properly. It should also be mentioned that, the file prefix must remain identical to that of any other files created through 1-D velocity model if a mixture of both 1-D and 3-D model travel times are used in the location process. As an optional argument, the receiver elevation in kilometres can be given via `--rdepth` flag.

3.3.4 Previously determined station term files

Although we do not choose this option in the examples provided here, SCOTER has the ability to start the relocation process using pre-determined station terms (either static or source specific). This functionality can be critical for application in routine near real-time processing where relocating a single-event using previously determined source-specific station terms (SSSTs) for neighbouring events is desired. We can also consider another special case in which the user is interested in rerunning the program for only the SSST location step (e.g. to test a different set of algorithm control parameters) and can make use of this functionality to apply the previously determined static station terms as a starting point for the SSST calculation. In these cases, SCOTER is flexible in its accommodation of pre-existing station terms. Table 3.4 shows an example of the format of the station terms file. Like the station data file (Table 3.1), any line starting with **#** is considered as a comment line and ignored.

3.3.5 Configuration file

SCOTER is configured with a plain text file in YAML format. The YAML format has been chosen because it can represent arbitrarily nested data structures built from mappings, lists, and scalar values. It also provides an excellent balance between human and machine readability. When working with such files, it is good to know that the indentation is part of the syntax and that comments can be introduced with the **#** symbol.

By invoking the subcommand below, a project structure is deployed into a directory and a template configuration file is generated that can be set up and used to relocate multiple events using SCOTER:

```
# Initialise new project structure
$ scoter init <project_dir>
```

Table 3.5 presents the overall structure of a SCOTER configuration file. It has a top-level container (mapping) that is introduced with the line `--- !scoter.Config` and has several child elements, e.g. `path_prefix`, `dataset_config` etc. Some of these entries may again contain their own child elements (indented blocks of lines) or lists (lines introduced with dashes).

The detailed description of the configuration file, parameters used and some tips to set those parameters are provided in Appendix A.2. In summary, main configuration sections in a SCOTER configuration file are:

- `DatasetConfig`: the core of input and data configuration. Here, the user defines where all input data such as observation phase files, input event and station data files, travel-time grid files are stored.
- `StationTermsConfig`: handles the parameters valid for static and source-specific station terms calculation, such as number of iterations, search radius for and minimum and maximum number of nearby events, misfit norm. It also consists of parameters to weight and control the location quality of neighbouring events during station terms calculation.
- `NetworkConfig`: provides the flexibility of using a subset of observed arrival times recorded within a specific surface distance range.
- `NLLocConfig`: the core of event location part of the calculation that provides a unified interface to configure and run the NonLinLoc program.

Table 3.5: Example SCOTER configuration file (YAML format)

```
%YAML 1.1
--- !scoter.Config

# All dataset file paths (input data) referenced below are
# treated relative to the location of this configuration file.
path_prefix: ".."

# Path, where to store output files (run directories)
rundir: "./out"

# ------------------------------------------------------
# Configuration section for dataset (input data)
# ------------------------------------------------------
dataset_config: !scoter.DatasetConfig
  bulletins_template_path: "data/phase/${event_name}.nll"
  stations_paths:
  - "meta/stations.sf"
    ⋮
# ------------------------------------------------------
# Configuration section for station terms
# ------------------------------------------------------
station_terms_config: !scoter.StationTermsConfig
  # Subsection on static station terms (STATIC)
  static_config: !scoter.StaticConfig
    niter: 0
    ⋮
  # Subsection on source-specific station terms (SSST)
  ssst_config: !scoter.SourceSpecificConfig
    niter: 20
    ⋮
  # Subsection on location quality control
  locqual_config: !scoter.LocationQualityConfig
    standard_error_max: 2.0
    ⋮
# ------------------------------------------------------
# Configuration section for station network selection
# ------------------------------------------------------
network_config: !scoter.NetworkConfig
  station_selection: false
  ⋮
# ------------------------------------------------------
# Configuration section for location parameters
# ------------------------------------------------------
nlloc_config: !scoter.NLLocConfig
  trans: !scoter.NLLocTrans
    # Subsection on geographic transformation
    trans_type: "GLOBAL"
    ⋮
```

3.4 Guided tour of use cases

In this section, we describe the computational details underlying the current implementation of SCOTER. Two examples including the Arctic plate boundary region and the western Iberia, Portugal are provided as a demonstration of the package. As we intend this code to be open-source, future releases of the code may include minor modifications and more functionalities to the algorithm presented here. All the location results shown in this section are obtained by setting the configuration parameters to case-specific values. Although our method requires only the phase picks, the station locations, and a set of pre-computed travel-time grid files, careful tuning of some of the parameters is required for different applications to achieve optimal results.

3.4.1 Application to the seismicity along the Arctic plate boundary

3.4.1.1 Data set

Our first data set is a bulletin of 614 seismic events in the Arctic boundary region. The earthquakes occurred from 1998 to 2015 between 70°N−84°N and 9°W−10°E. The magnitude of the events ranges from M2.0 to M6.0. The bulletin has been generated by using high-quality P- and S-wave arrival times. The primary selection criterion was that the events had clear regional P and S onsets at several of the permanent regional stations on both sides of the spreading ridge which are most sensitive to low-magnitude events. A minimum requirement was six phases. The phase arrivals for events with larger magnitudes were augmented by teleseismic P arrivals from the Reviewed Event Bulletin (REB) of the International Data Centre (IDC) with signal-to-noise ratio exceeding 3.0. Supplementary teleseismic phases have been recorded by the distant seismic arrays and three-component stations of the International Monitoring System (IMS). The teleseismic azimuthal coverage provided by the IMS for this source region in the Northern Hemisphere is superb and this increases the likelihood of high epicenter accuracy based on seismic network criteria (Bondár et al., 2004). Fig. 3.2 shows the seismicity in the region of interest together with the distribution of the permanent regional network and IMS stations at far-regional and teleseismic distances. Following is a step-by-step guide explaining how to obtain improved event locations for the seismicity in the Arctic plate boundary region using SCOTER.

3.4.1.2 Data preprocessing

The Arctic earthquake data set is composed of 614 events for which the pick information is included and stored in a single file in `QuakeML` format (Schorlemmer et al., 2011). Following command is issued to load and parse the bulletin file and will write the observation phase files in the `NLLOC_OBS` file format for each seismic event contained in the bulletin file:

```
# Parse QuakeML and dump into NLLOC_OBS
$ scoter dump-obs ./data/Bulletin_Arctic.xml --format=QuakeML
↪ --prefix=eid_ --output-dir=./data/phase/
↪ --output-events=./data/events_arctic.pf
```

The output phase files are automatically named according to the event names (i.e. resource identifiers of the events). Optionally, a prefix and a suffix can be provided for the above subcommand to customise the names of the output phase files by specifying `--prefix` and `--suffix` options. In this example, the name of each output observation file begins with

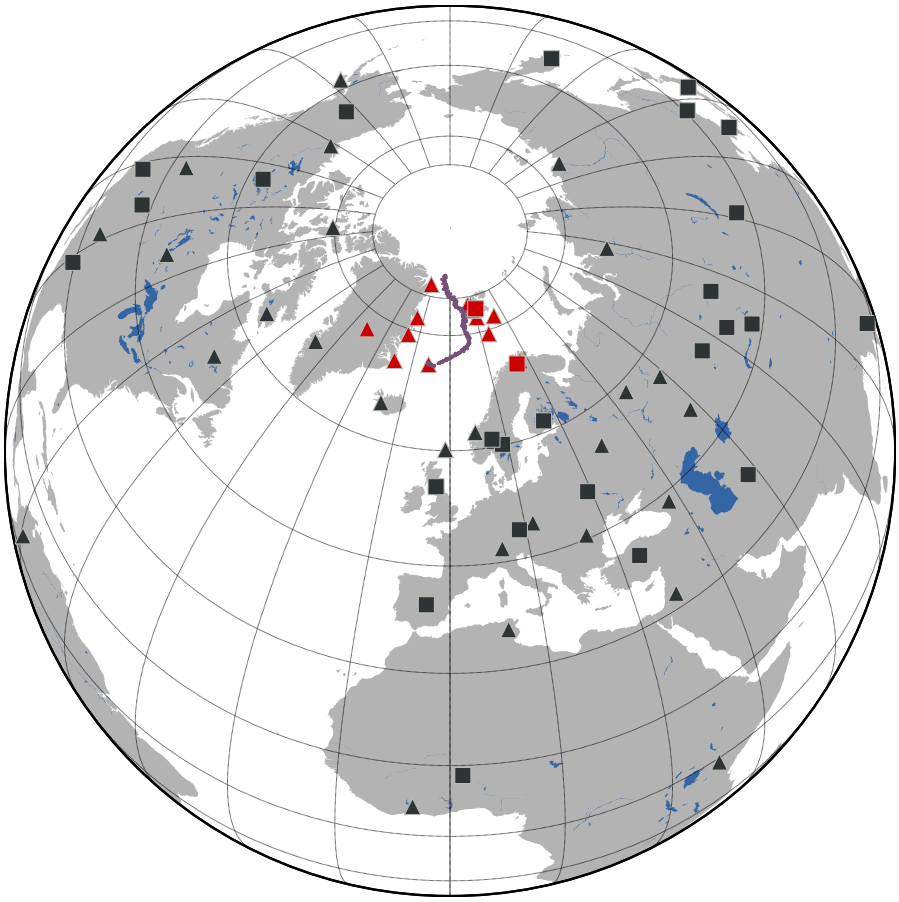

Figure 3.2: Global map showing ridge seismicity in the region of interest from 70°N–84°N together with the regional network displayed in red and the International Monitoring System (IMS) stations at far-regional and teleseismic distances shown in black. Triangle and square symbols indicate permanent three-component stations and seismic arrays, respectively.

`eid_` prefix followed by the event identifier (unique name). The other file output by running the command above, `events_arctic.pf`, is in `Pyrocko` event file format (Heimann et al., 2017) and contains information and possibly reference solutions for all events available in the data set. During the relocation procedure, the program can access the available observation files by looking into possible expansions of a template string containing `${event_name}` placeholder, which is substituted with the event names defined in the events information file mentioned before. It should be noted that SCOTER also lets the user relocate events with a subset of arrival times recorded by stations at a specific epicentral distance range. To take up this option, the user should make sure that their initial bulletin data set provides a reference hypocentre solution for each event, since the station data selection (filtering) in SCOTER is based on the surface distances between the reference (initial) epicentre of the events and seismic stations. In this example, such information is included in the initial bulletin data and will be automatically saved into the events file.

Our data set for the Arctic plate boundary region consists of the first regional *P* phases labelled as *P1*, the first regional *S* phases labelled as *S1*, and teleseismic *P* arrivals. For the velocity model, here we create a custom 1-D model Fennoscandian (FESCAN, Mykkeltveit and Ringdal, 1981) in `tvel` format and use the model from the saved file to compute the seismic travel times. Travel- time grid files for these phases are easily built by invoking the following commands given the epicentral distance range, depth range, a file prefix, and our custom velocity model file:

```
# First regional P and S travel times
$ grist raytrace-1D --phase=P1,S1 --model=model/fescan.tvel
↪ --distances=0:14.95:0.05 --depths=0:35:2.5
↪ --prefix=fescan --out-dir=./time/

# Teleseismic P travel times
$ grist raytrace-1D --phase=P --model=model/fescan.tvel
↪ --distances=13:124.75:0.25 --depths=0:35:2.5
↪ --prefix=fescan --out-dir=./time/
```

It should also be noted that the file prefix must be the same when travel-time grid files are created for different phases. Surface distance and depth values are defined by giving the corresponding minimum, maximum and step-size values in the format of `min:max:step`. In the example command above, the teleseismic P-wave travel times are calculated from sources at a depth range of $0-35$ km with a depth interval of 2.5 km, to the receivers within the epicentral distance range of $13° - 124.75°$ with a distance spacing of $0.25°$.

3.4.1.3 Configuration set-up

To initiate a relocation project for the Arctic earthquake data set, we can run the command below that will create a project directory called `arctic` in the current directory:

```
# Initialise the Arctic project directory
$ scoter init arctic
```

The project folder already contains a configuration file for multiple-event location with SCOTER. Before going further, we need to put the observation phase files and travel-time grid files prepared in Section 3.4.1.2, as well as the station files, in our project directory following the folder structure suggested in Figure 3.1.

The complete configuration file is quite extensive and, for the sake of brevity, the reader is referred to the generated configuration file itself to get familiar with variables needed to be set while it has been tried to provide it as a self-explanatory file. Moreover, Appendix A.2 explains in some detail the many configuration options available in SCOTER. In general, the settings for different configuration sections (see Section 3.3.5) are quite straightforward and the user can easily follow the documentation in the provided configuration file to modify it for their own future purpose.

To refine the event locations in the Arctic bulletin data set, we will first relocate all seismicity with the 1-D velocity model FESCAN (referred to as single-event locations) and then, in an iterative manner, we estimate the direct P- and S-wave SSSTs for each source-receiver ray paths to reduce the biasing effects of the true 3-D earth structure and relocate the events by applying the obtained correction terms. Although we could obtain our initial locations using the static station term method and then use these station terms as a starting point for SSST calculation, we perform a generalisation of this approach that is to continuously reduce the cut-off distance for searching nearby events between first and final iterations. In other words, we start the search radius with a large value to include a large group of events from which we compute the SSSTs, then decrease it to some specified minimum distance to calculate station terms using only the closest events. To relocate events in the Arctic plate boundary region, we perform 20 iterations of SSST computation and gradually reduce the distance cut-off during the iterations from 500 to 50 km. We also use all available

neighbouring events found within a search radius at each iterations.

3.4.1.4 Checking data and configuration

Before beginning the actual relocation process, we can now execute the following subcommand to run some sanity checks:

```
# Check data and configuration
$ scoter check config/config_arctic.sf
```

In particular, SCOTER exercises a subset of application functions needed to determine whether it can access and read the input data and to assure that the configuration parameters are set carefully and the relocation analysis works roughly as expected. It is basically a quick, broad and shallow testing that SCOTER offers to avoid wasting the user's time and effort. The sanity-check information is reported to the standard output.

3.4.1.5 Starting the relocation process

When the configuration file is ready, we can run the relocation procedure by invoking the subcommand `go`:

```
# Run scoter multiple-event location
$ scoter go config/config_arctic.sf --steps=A,C --parallel=8
```

The location process can be run in parallel using multiple CPUs at the same time, which makes the runtime faster. The number of events to process in parallel can be set by specifying `--parallel` option. If -1 is given, all CPUs in the system are used. As mentioned before, SCOTER can be used for single-event relocation without applying any station terms (Single), static station terms relocation (Static), and source-specific station terms relocation (SSST). For simplicity, these steps are named as A, B, C, respectively. Therefore, any desired relocation step(s) can be re-run, for instance, to play around with different configuration parameters. In this example, the relocation procedure starts with single-event location and then, in an iterative manner, estimates the P- and S-wave SSSTs for each source-receiver ray paths to reduce the biasing effect of the true 3-D earth structure and relocates the events by applying the obtained correction terms to P and S phases.

3.4.1.6 Exporting the results

To export the final results (e.g. hypocentre parameters, travel-time residuals), first we need to execute the subcommand `harvest` to cache the results:

```
# Run harvesting to cache scoter results
$ scoter harvest config/config_arctic.sf --parallel=8
```

For iterative steps (i.e. Static and SSST steps), this stores the results for all available iterations. If the user decides that they only need the outputs for the last iteration, they can pass the flag `--last-iteration` (or `--last-iter` as an alias) to the subcommand `harvest`. Specifying the `--weed` flag makes it possible to weed out only those events having at least one phase arrival time corrected by a station term value in each iteration.

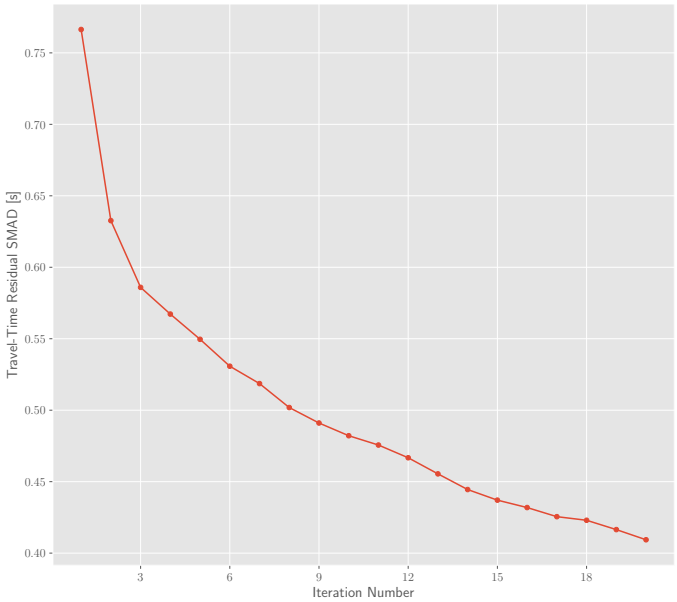

Figure 3.3: Reduction of travel-time residual SMAD for the 614 events in the Arctic plate boundary region with iteration numbers of SSST calculations.

The convergence of the algorithm can be evaluated in terms of the median absolute deviation (MAD) or scaled median absolute deviation (SMAD, a robust measure of the spread of a distribution which is equal to the standard deviation for Gaussian distributions) of the travel-time residuals from one iteration to the next by running the following command:

```
# Plot convergence curve of the SSST calculation
$ scoter plot-convergence config/config_arctic.sf --step=C
↪ --statistic=SMAD --save --format=pdf
```

which creates Figure 3.3 and saves it as a pdf file. The figure shows the reduction of the travel-time residual SMAD from the 614 events with iteration number in our SSST calculation. The SMAD of the residuals drops from 0.135 to 0.1 s.

Moreover, SCOTER offers several subcommands to export some values of interest that can save much user time, such as applied station correction terms, initial and final hypocenter parameters, travel-time residuals before and after applying the station correction terms. The output files are in convenient formats for statistical analysis and plotting and can be easily loaded and used in some other libraries and tools such as numpy and GMT. For example, we can issue the following command to export an ascii file in column format that provides the first *P* phase (labelled as *P1* in the catalogue) station term corrections for a particular regional station SPITS. The station terms for each event recorded at the receiver in question are reported at each event location in the output file:

```
# Export source-specific station terms
$ scoter export-ssst config/config_arctic.sf --phase=P1
↪ --network=IM --station=SPITS --output=export/SSST_SPITS_P1.dat
```

Figure 3.4 shows the final calculated first regional *P*- and *S*-wave SSST values relative to the 1-D velocity model FESCAN for the regional array SPITS. The station terms for each event recorded at the receiver are plotted at each event location. Spatial coherence of the pattern of the SSSTs indicates the existence of heterogeneities in the real velocity structure. Positive

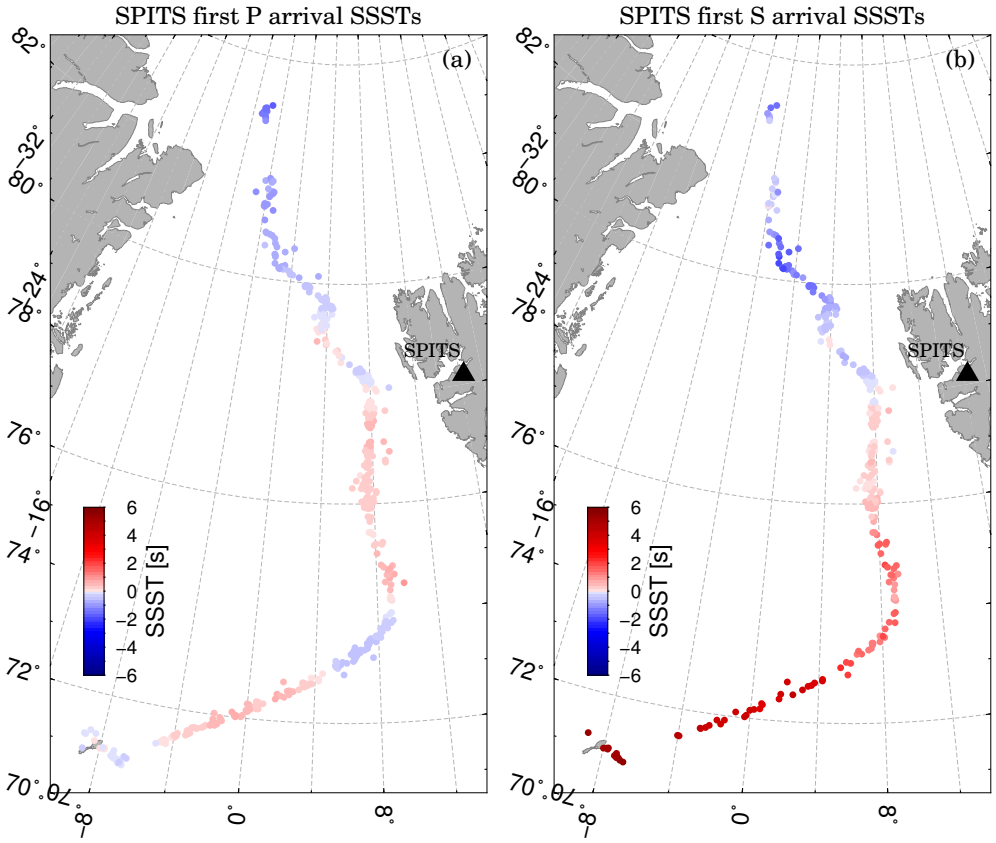

Figure 3.4: Calculated source-specific station terms (SSST) for regional seismic array SPITS for (a) first *P*-wave arrivals and (b) first *S*-wave arrivals. The SSST values are color coded and plotted at the event locations.

correction terms indicate low velocities and negative values reflect high velocity anomalies on the way of the seismic rays travelling from sources to the receiver.

Hypocentre parameter files for each location step can be exported easily by invoking the following commands:

```
# Export hypocentre parameter files
# Single-event location (step: A)
$ scoter export-events config/config_arctic.sf --step=A
↪ --format=columns --output=export/events_Single_loc.dat

# SSST location (step: C)
$ scoter export-events config/config_arctic.sf --step=C
↪ --format=columns --output=export/events_SSST_loc.dat
```

The output files can be exported in either column or `Pyrocko` event file format. Figure 3.5a-b shows in map view a comparison of SSST locations and single-event locations. Here, the spatial scattering and alignment of seismicity into planar features can be considered as a qualitative measure of the improvement in the SSST relocations. This is visible in the decreased scatter and improved clustering in the new hypocentre locations, which better define the Arctic plate boundary. Figure 3.5c reveals that the SCOTER algorithm provides relative location improvements comparable to the BayesLoc program by Myers et al. (2007) shown by previous studies (Gibbons et al., 2017a). The BayesLoc algorithm does provide

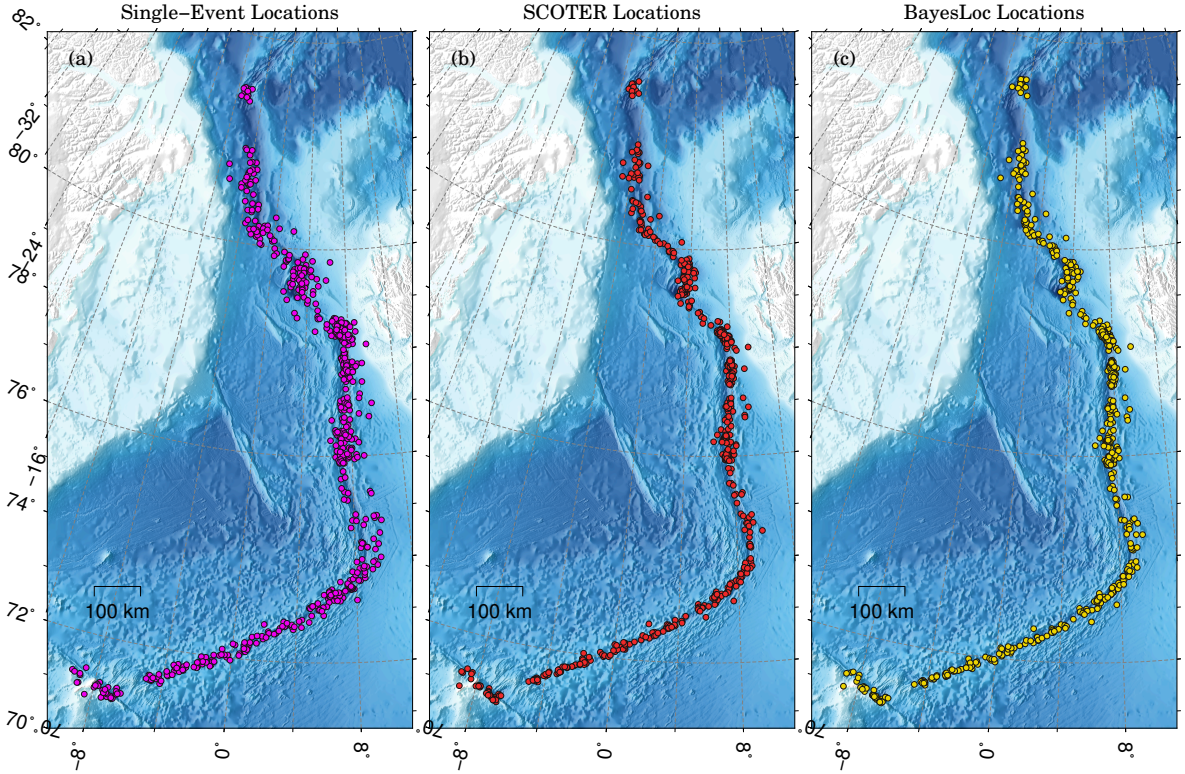

Figure 3.5: Relocated seismicity in the Arctic Ridge using (a) a single-event, non-linear algorithm and (b) source-specific station correction terms (SSSTs) implemented in the SCOTER program, and (c) BayesLoc locations presented in Gibbons et al. (2017a).

an extensive list of algorithm control parameters relating BayesLoc probability model and MCMC sampler and the optimal parameter choices required to obtain the best locations may not be always obvious to the user. Although SCOTER has its own set of parameter choices, we designed them to be as few and as straightforward as possible.

The travel-time residuals for a particular seismic phase can be simply obtained for each recording station in the dataset and stored as plain-text files by issuing the subcommand `export-residuals`, which extracts the residuals at a given seismic station before and after application of computed station correction terms:

```
# Export travel-time residuals
$ scoter export-residuals --phase=P1 --network=IM --station=SPITS
↪ --output=export/residuals_SPITS.dat
```

The output file is in column format and can be comfortably used in different plotting tools to make and compare histograms of residual distributions. Figure 3.6 compares histograms of first P and first S travel-time residuals at the regional network SPITS from single-event and SSST locations and depicts significant improvements to residual reduction achieved by using station correction terms. Applying SSST values leads to the SMAD reduction of 68 per cent and 58 per cent for P and S arrival times, respectively, at the regional network SPITS.

The program also provides the user with the subcommand `plot-residuals` to make figures that summarize residual analysis as a function of event-station distance. As an example, figures similar to the sub-plots on the left column in Figure 3.7 can be created by invoking the following command:

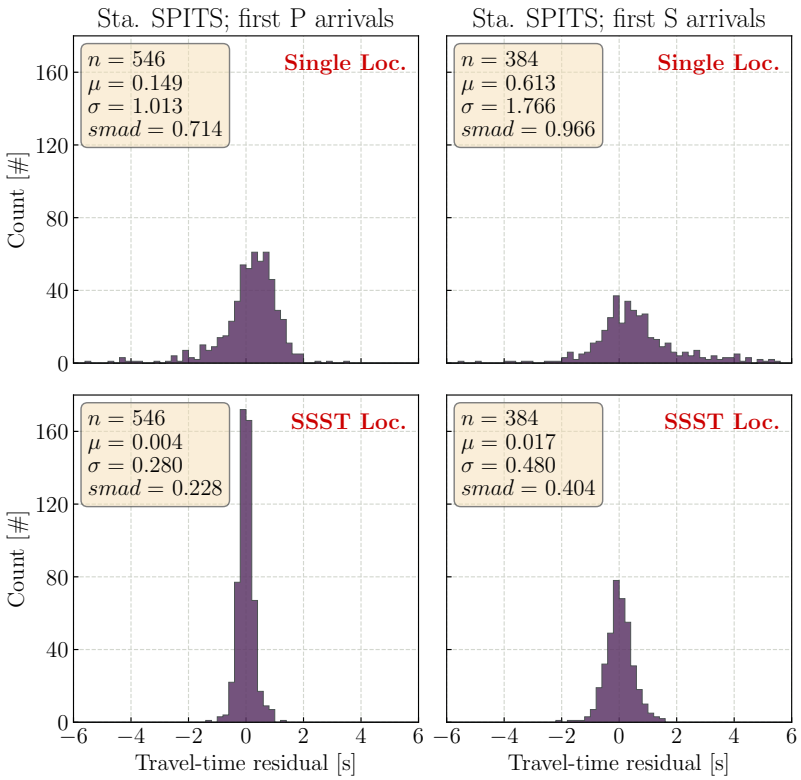

Figure 3.6: Histograms of the travel-time residuals from (top) single-event and (bottom) the SSST relocations for the station shown in Fig. 3.4. The scaled median absolute deviation (smad), mean, and sample standard deviation of each distribution are indicated on each panel.

```
# Plot travel-time residual heat maps (2-D histograms)
$ scoter plot-residuals --phase=P1 --steps=A,C --distances=0:15:1
↪ --residuals=-10:10:0.2 --colormap=gist_heat
```

It should be mentioned that the frequency of occurrence (heat plots) of the residuals are normalized in the given distance range so that the residual bin with the largest number of hits (the scaling cell) is assigned a value of 1. In the command above, distance and residual ranges are specified by giving the corresponding minimum, maximum and bin-width values in the format of `min:max:bin-width`. Figure 3.7 reveals that strong variations in initial *P*- and *S*-wave residuals are smoothed out in the final residuals from events and peaks in the near-regional and regional distances where the effect of lithospheric velocity anomalies is strong.

3.4.2 Application to the seismicity in western Iberia, central Portugal

As the second demonstration of the program, we use SCOTER to relocate low-magnitude, local-scale earthquake clusters in western Iberia, Portugal. The seismic data were recorded by a local broadband array (DOCTAR array) deployed in the Western Ossa Morena Zone (WOMZ) between June 2011 and September 2012 (Matos et al., 2018). The data set was also complemented with data recorded by nearby permanent and temporary stations.

In this example, we relocate the earthquakes using a 3-D tomographic velocity model. Specifically, we use the 3-D Preliminary Reference Iberia Seismic Model (PRISM3D) (Arroucau et al., 2017), which is a three-dimensional *P*- and *S*-wave velocity model for Iberia

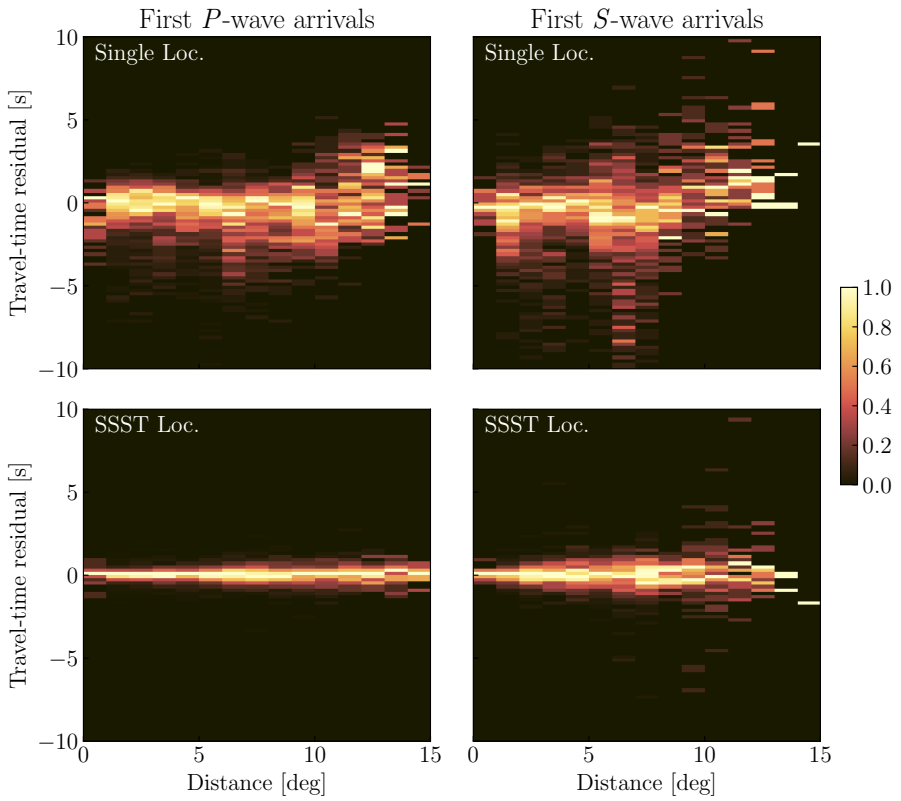

Figure 3.7: Frequency of occurrence (heat plots) of travel-time residuals for (top) single-event and (bottom) the SSST locations. The heat plots are normalized in each distance range so that the residual bin with the largest number of hits (the scaling cell) is assigned a value of 1. All other bins in that distance range are linearly scaled from zero to one by dividing the number of hits by the number of hits in the scaling cell.

and north Africa based on several previously published geophysical models (e.g. tomographic models, receiver functions and active source studies). Although 3-D velocity information provides enhanced absolute hypocentre locations, the tomography model is relatively smooth and cannot account for small-scale velocity structure that can also introduce bias and scatter in event locations. Thus, to further refine the event locations, we combine the shrinking-box SSST method and 3-D model location. Our strategy is to first relocate all events using the PRISM3D model. Then, to constrain the absolute locations, we calculate a set of well-constrained static station terms using a group of 3-D relocated events with at least four recording stations, an azimuthal gap $< 180°$ and at least one station within 20 km of the event. These *a priori* static station terms are then included in the SSST location process in which the SSST values for P- and S-wave picks are computed from the travel-time residuals of nearby events and subtracted from the arrival-time picks, and the 3-D relocation process is repeated with the adjusted arrival-time data. Here, we perform five iterations of 3-D location and SSST computation. The distance cut-off for SSST calculation is reduced gradually during the iterations from 50 km to 10 km. The relocation results are shown in Figure 3.8. The notable differences between two sets of locations are that the newly located hypocentres show improved clustering and sharpen seismogenic source zones in the region. For the new catalogue relocated using SSSTs, average shifts relative to single-event locations are ∼4.5 km in epicenters and ∼3.2 km in depth. Overall, the location uncertainties of SSST locations are about $30 - 40$ per cent those of the single-event locations (Figure 3.9). Furthermore, Figure 3.9 reveals that the new locations appear to be more clustered and some substructure can be seen.

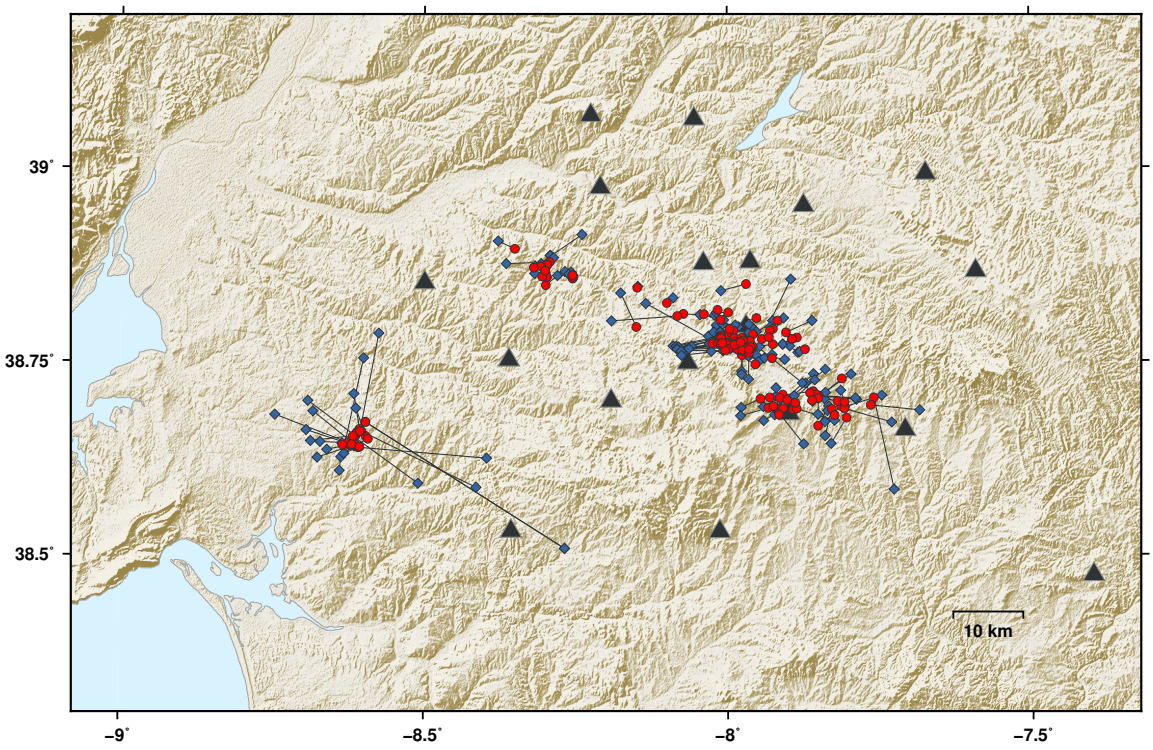

Figure 3.8: Map view of the seismicity in the Iberia region, Portugal. Non-linear, single-event locations and SSST locations are shown by blue diamonds and red circles, respectively. Solid lines indicate mislocations between corresponding hypocentres. Triangles represent seismic stations.

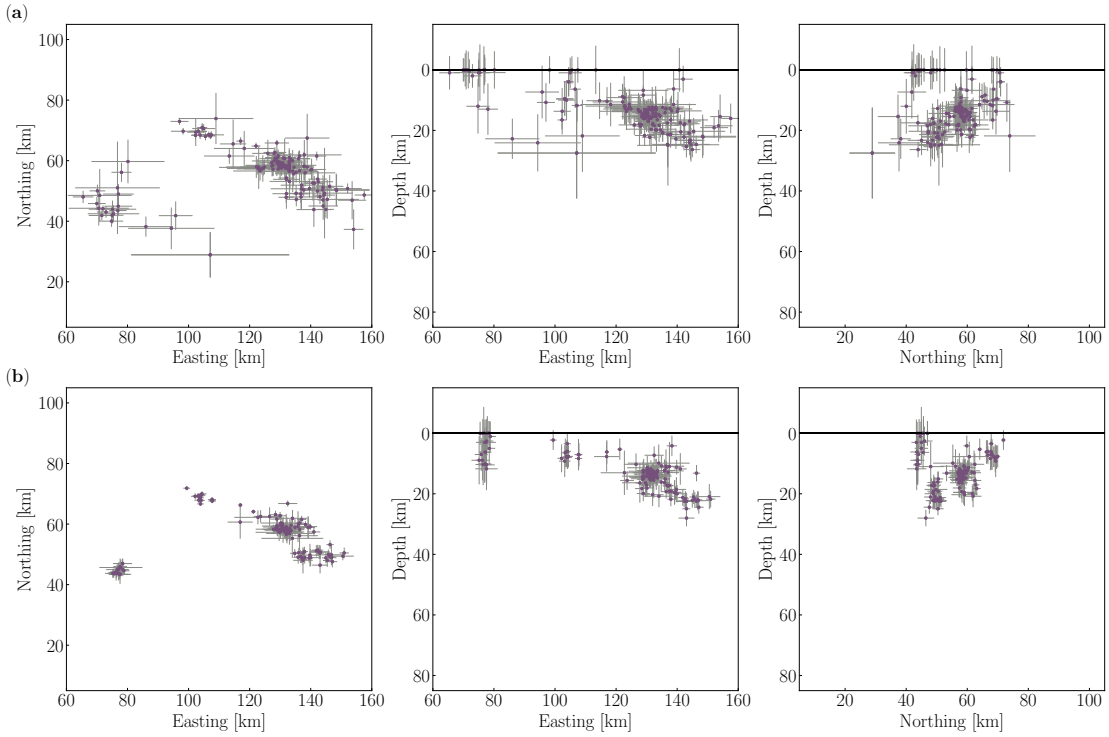

Figure 3.9: (a) Horizontal view and vertical cross sections of the non-linear, single-event locations and the associated 68% uncertainty bounds. (b) The same as Figure 3.9a but for SSST locations. The reference point $(X, Y) = (0, 0)$ corresponds with the point $(\lambda, \phi) = (-9.50, 38.25)$ in the geographic coordinates system.

3.5 Summary

SCOTER is an open-source earthquake relocation tool that applies deterministic static and source-specific station terms to improve the relative location accuracy among nearby events. The algorithm is adopted for probabilistic, non-linear, global-search location and enables more robust relocation results. This package can be used for relocation of large numbers of distributed earthquakes in local, regional, and teleseismic scales. It provides the user with a number of powerful tools that are useful and handy for preparing the input data and post-processing and visualising the relocation results. Functionality, design and technical implementation of the new tool is in the pursuit of providing a simple and flexible environment for the user. SCOTER's main functionalities and performance were demonstrated through examples. The encouraging results for these examples showed the scientific potential for large-scale relocation efforts using the SCOTER tool.

The SCOTER relocation codes described in this chapter comprise an open-source software package under the GNU General Public License, Version 3.0 (GPLv3). The latest version of the SCOTER source distribution, which includes source codes, a user guide, an example data set, and a change history, is publicly available for download via the project repository at https://gitext.gfz-potsdam.de/nooshiri/scoter.

Chapter 4

Toward near real-time relative event location using long-term archives of earthquake bulletins

Abstract

We evaluate the potential of a relative location technique in a simulated near real-time manner to improve the location of new earthquakes relative to past events with accurately known locations. The relocation procedure uses phase arrival times of new events and of past events by accessing the long-term seismic archives. Using the routine location of new events, an existing base catalogue is searched for the best-suited reference events in the neighbourhood of the new events. The reference events should be homogeneously located around the new event, have a magnitude > 4.5 and secondary teleseismic azimuthal gap $< 180°$, and be recorded at a very similar set of regional and teleseismic stations. A set of travel-time corrections is computed for each receiver as the average of the residuals from reference neighbouring events. The calculated station terms are added to the theoretical travel times computed for the new events to reduce the biasing effects of lateral velocity heterogeneities and improve the accuracy of routine location of new seismic events. In this relocation procedure, new events can be relocated relative to a set of master events in near real-time. By relocating a set of reliable ground-truth events and using locally stored ISC-EHB bulletin data set, that is a groomed version of the Internation Seismological Centre (ISC, 2019) bulletin containing teleseismically well constrained events selected from the ISC Bulletin and are relocated using an update of the EHB methodology (Engdahl et al., 1998), as our base, high-resolution catalogue, we assess the performance of the new proposed method and demonstrate that applying such technique significantly reduces the bias in routine locations and enhance the ability to locate the lower magnitude events (M$<$ 4.0) using only regional arrival times.

4.1 Introduction

Rapid and accurate estimation of seismic event locations is a fundamental task in near real-time seismic monitoring. Earthquake locations provide information on the area of potential damage due to strong ground shaking. Moreover, the estimated hypocentre location may influence rapid source mechanism studies and can be already an indicator of whether the event has a potential to generate a tsunami. Furthermore, a location is required to determine the size of an earthquake. Therefore, estimates of location of a new seismic event are crucial for efficient disaster reduction response. In general, earthquake locations are computed on a routine basis and subsequently communicated to authorities and the public. The hypocentral information and associated meta-data such as phase arrival times are produced during routine operations and are typically archived in large databases. These archives are primary resources for the scientific community to perform quantitative seismological analyses, such as seismic hazard analyses, fault-zone characterization, and assessments of seismicity and strain rates in the Earth.

Most seismological agencies process seismic waveforms from new events in near real-time to measure seismic phase arrival times (either automatically or manually, or a combination of both) and associate them to individual earthquakes and compute the location of the events. In routine location procedures, events are located one at a time by an inversion of the phase arrival times using an assumed 1-D velocity model. Although such single-event location procedures are fast and relatively robust, the uncertainties in the locations are often significant mostly because of deviations of the true velocity model from the model used to compute the theoretical travel times (Pavlis, 1986). Particularly for regional stations, where the velocity structure strongly deviates from the assumed 1-D model, large travel-time residuals are observed even for clear arrivals with small picking uncertainties, resulting in systematically biased locations.

Several studies have demonstrated improved travel-time prediction accuracy using tomographic velocity models (Smith and Ekström, 1996; Antolik et al., 2001; Chen and Brudzinski, 2001; Myers et al., 2015). However, although the obtained velocity information provides enhanced absolute hypocentre locations by reducing the biasing effects of large-scale velocity structure, usually only a smooth model can be obtained, which cannot effectively account for small-scale velocity heterogeneities, particularly when applied to global earthquake location. Moreover, computation of travel times through 3-D models can be relatively expensive and therefore travel times through 3-D models are most commonly precomputed from each station to a grid of geographic points. However, this approach may not be practical for routine processing that utilises many hundreds or thousands of stations. Despite advances in the development and application of 3-D models, radially symmetric global models such as ak135 (Kennett et al., 1995) remain the standard for routine seismic location.

There have been numerous studies that developed and applied multiple-event location methods to improve on the low-spatial resolution of catalogued routine single-event locations through the joint relocation of pairs or clusters of events to determine their relative hypocentre position (Douglas, 1967; Jordan and Sverdrup, 1981; Got et al., 1994; Richards-Dinger and Shearer, 2000; Shearer, 2002; Waldhauser and Ellsworth, 2000; Lin et al., 2007; Myers et al., 2007; Grigoli et al., 2016; Nooshiri et al., 2017; Trugman and Shearer, 2017). By relocating multiple events simultaneously, these approaches are able to minimize the bias in routine locations due to errors in the assumed velocity model. Relative relocation methods have been used extensively to improve the resolution in routine catalogue locations and study the detailed structure of tectonic faults and spatio-temporal behaviour of seismicity in areas of special interest.

Despite their ability to yield significant improvements to relative location accuracy, such advanced relocation techniques have not been implemented into the near real-time earthquake location performed by seismological surveys. One reason for this may be that the use of multiple-event location methods in near real-time processing requires an *a priori* known high-resolution catalogue of past seismicity and fast access to an archive of past seismic data. Another reason may be that relative location solutions are dependent on all nearby events and adding a new event to the catalogue would affect the locations of older events in the catalogue and the whole data set would need to be relocated for consistency. It is clear that a reprocessing of the whole catalogue is not feasible in this context.

In this study, we present the first step in an effort to the near real-time application of a relative relocation method in a global monitoring context. We evaluate the potential of source-specific station terms (SSST) technique (Lin and Shearer, 2005; Nooshiri et al., 2017) to improve, in near real-time, the location of new events relative to an *a priori* known high-resolution global catalogue of past seismicity. The simulated near real-time location procedure utilises phase picks of new events and of past events by accessing the seismic archives. More precisely, it uses the location information to search in an existing base catalogue for the best-suited reference events in the neighbourhood of the new event and computes a set of travel-time correction terms for each receiver as the average of the residuals from reference neighbouring events which have picks at the station in question. We use the ISC-EHB data set (Weston et al., 2018) as the base catalogue, which is the most robust, high-resolution global data set of earthquake locations available, that contains teleseismically well-constrained events selected from the ISC bulletin and relocated using the EHB algorithm (Engdahl et al., 1998). We evaluate the performance of the proposed technique to improve the location accuracy and reduce the location uncertainty of new earthquakes relative to the historic seismicity by relocating a set of reliable ground-truth (GT) events having high-confidence epicentral estimates and high-quality arrival times.

4.2 Data set

4.2.1 ISC-EHB bulletin

Validation and neighbouring reference events are selected from the ISC-EHB bulletin, which is a groomed version of the ISC bulletin and contains teleseismically well-constrained events from 1960 to 2014 (Weston et al., 2018). The original EHB data set (Engdahl et al., 1998) stopped in 2008 and since then the volume and quality of data has significantly improved. To take this into account, the event selection, data preparation and processing, and location procedure have been updated at the ISC seismological center. As a consequence, a cleaner and more robust data set of events from 2000 to 2014 has been produced and this new data set has replaced the equivalent years in the original EHB bulletin (Weston et al., 2018). Therefore, we use 15 years of the ISC-EHB database covering the modern period 2000-2014 for event selection. The data set is split into two sets with no overlap; from 2010 to 2014 to select validation events, and the other one from 2000 to 2009 for finding nearest events (reference events) in the vicinity of each validation event. In this way, we simulate relocating a new seismic event (here, belongs to the first set) by applying deterministic travel-time correction terms that are computed using a long-term seismic archive (the second set of events).

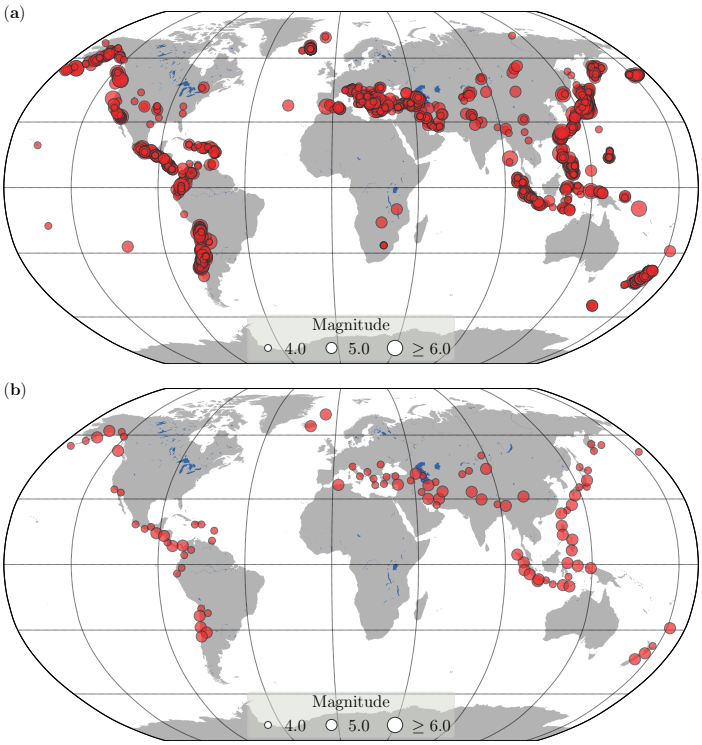

Figure 4.1: (a) Ground truth (GT) data set selected from the ISC-EHB bulletin in the period 2010-2014. (b) Validation data set, that is a subset of GT data set. GT selection criteria and the selection procedure for validation events are described in Section 4.2.2.

4.2.2 Selection of validation events

Location accuracy is our first consideration in the selection of validation events. Here, we adopt the terminology of Bondár et al. (2004), who introduced the nomenclature of "ground truth" categories and defined "GT$X_{C_{per\,cent}}$", where X designates epicenter location accuracy in kilometres and $C_{per\,cent}$ is the percentage confidence (i.e. the true epicenter lies within X km of the estimated epicenter at C per cent confidence). As a special case, GT$0_{95\%}$ is defined as well-recorded explosion event with known hypocenter location and origin time (Myers et al., 2015). Making use of explosion reference events with exactly known epicenters, Bondár et al. (2004) developed GT$5_{95\%}$ accuracy criteria for earthquake epicenters constrained by a local seismic network (wholly within 2.5° of the event). A GT$5_{95\%}$ location must be located with: (1) at least 10 recording stations, (2) an azimuthal gap of less than 110°, (3) a secondary azimuthal gap (largest azimuthal gap filled by a single station) of less than 160°, and (4) at least one station within 30 km of the event to constrain the depth. Based on Monte Carlo simulations of network geometry, Bondár et al. (2004) found that event locations are accurate to 5 km at a 95% confidence level when they meet these criteria. In our validation studies, we consider only events categorized as GT$0_{95\%}$ or GT$5_{95\%}$ (hereafter for brevity, referred to as GT events). Figure 4.1 shows the location map of the GT events selected from the ISC-EHB data set in the period 2010-2014.

We restrict the study to the first P-wave arrival times observed at regional ($2.5° - 20°$) and teleseismic ($22° - 90°$) distances, labelled as Pn and P phases in the ISC-EHB catalogue, respectively. We do not use S-wave arrival times in our relocation process since the identification of the S phases is difficult to implement in real-time automatic algorithms, and therefore they are seldom used in (near) real-time automatic solutions. Events meeting GT criteria explained above are sorted based on (1) the number of Pn arrivals, (2) the number

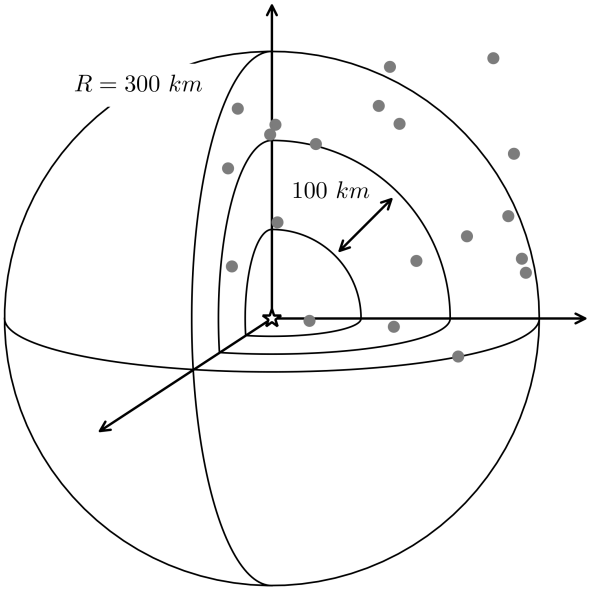

Figure 4.2: Schematic illustrating the search scheme for neighbouring reference events. A limited number of events (dots) are collected within each quadrant of increasingly thicker spherical layers. The star symbol represents validation event's routine location. See Section 4.2.3 for discussion.

of P arrivals, and (3) the seismic network azimuthal gap. These categories are intended to provide fairly reasonable sampling of regional and teleseismic ray-paths, as well as events with good network geometry for relocation tests. To select validation events, we perform an iterative procedure in which the top-ranked event in each of the three categories, without duplication, is selected and all events within 3° of the selected events are removed from the candidate list. The process is repeated until the pool of candidate events is exhausted. Therefore, our validation data set has nominal event spacing of 3° for each of the three categories. The resulting set of validation events consists of 103 seismic events with 8,848 Pn and 25,903 P-wave arrival times.

4.2.3 Selection of neighbouring reference events

When searching for neighbouring reference events, the goal is to find events in the ISC-EHB base catalogue that are close enough to the validation event's routine location and share common ray-paths to common stations. Therefore, the travel-time residuals to a given station are spatially correlated among these close-by events because they are affected by almost similar structure. In areas with large clusters of correlated events, a pure nearest neighbour search may collect all or an abundance of nearby reference events within large multiplets of which the validation event is not a member. In order to perform a spatially homogeneous sub-sampling, we select nearby events within each of three concentric, spherical layers of increasing thickness (Figure 4.2). Each layer is split to its eight quadrants and only a limited number of events are collected from each of the 24 sub-regions. In our application, we set the radii of the layers to evenly-spaced values within 100-300 km interval with 100 km spacing between two adjacent layers, and select the most recent five events, and desirably with magnitude > 4.5, from each quadrant searching the locally stored ISC-EHB bulletin. It should be noted that the event selection criteria applied in creating the ISC-EHB assures that our neighbouring reference events have a secondary teleseimic azimuthal gap $< 180°$ (Weston et al., 2018).

4.3 Method

4.3.1 Location procedure

The SCOTER program is used to relocate events one at a time for the validation tests. SCOTER is an open-source Python program package for multiple-event relocation using station correction terms. The location routine employs static and so-called shrinking-box source-specific station terms technique extended to regional and teleseimic distances and adopted for probabilistic, non-linear, global-search location (Nooshiri et al., 2017). Here, we use a modified version of the station correction terms algorithm that constrains a new event (i.e. validation event) relative to its neighbouring reference events in the ISC-EHB base catalogue. The basic algorithm is described by the following steps:

(1) Travel-time correction terms, s, are computed for each receiver, j, as the mean (or median in case of L1-norm) of the residuals from N neighbouring reference events located within a sphere of R around the routine location of the new event (i.e. validation event).

(2) Arrival times, T^{obs}, are corrected by the calculated travel-time corrections ($T_j^{\prime obs} = T_j^{obs} - s_j$).

(3) The new event and all of its neighbouring reference events are relocated with corrected arrival times.

(4) The above steps are repeated iteratively until they converge to a stable set of travel-time corrections and new event location.

In our relocation procedure, the station correction terms are specific to the new event and are computed by smoothing the residuals over adjacent reference events. The degree of the smoothing is determined by the number of nearby reference events N within the cut-off radius R. In order to model large to small scale of lateral velocity heterogeneities, we continuously decrease the value of N between first and last iteration by shrinking the cut-off distance R. In practice, we have found in most cases that convergence to a stable set of location and correction terms is rapid and requires only a few iterations. Here, we set the number of iterations to three and the size of the smoothing sphere to 300, 200 and 100 km during the iterations (i.e. the corresponding values of N are 120, 80 and 40, respectively).

In our relocation method, we constrain changes in the hypocentral parameters of the reference events that are assumed to be well located. This is performed by defining a 3-D search grid of 4 km size around the location of each neighbouring reference event given from the ISC-EHB catalogue. In general, this procedure results in very small changes in the reference events while the new event moves towards its optimal location. Our relocation algorithm has some similarity to the master-event location technique (Evernden, 1969), except that in the master-event method many slave events are relocated with respect to one master event, while in our procedure one slave event is relocated relative to a set of reference events (master events).

The nearby reference events are also weighted according to dynamically adjusted weights that account for effective inter-event distance during individual iterations. In order to efficiently reduce the effect of the velocity heterogeneities for neighbouring events with large separation distances, each nearby event is weighted as a function of both its distance to the new event, d_i, and the angle, α_i, between its position vector relative to the new event location and the ray take-off direction computed at the new event location with respect to the recording station (Figure 4.3):

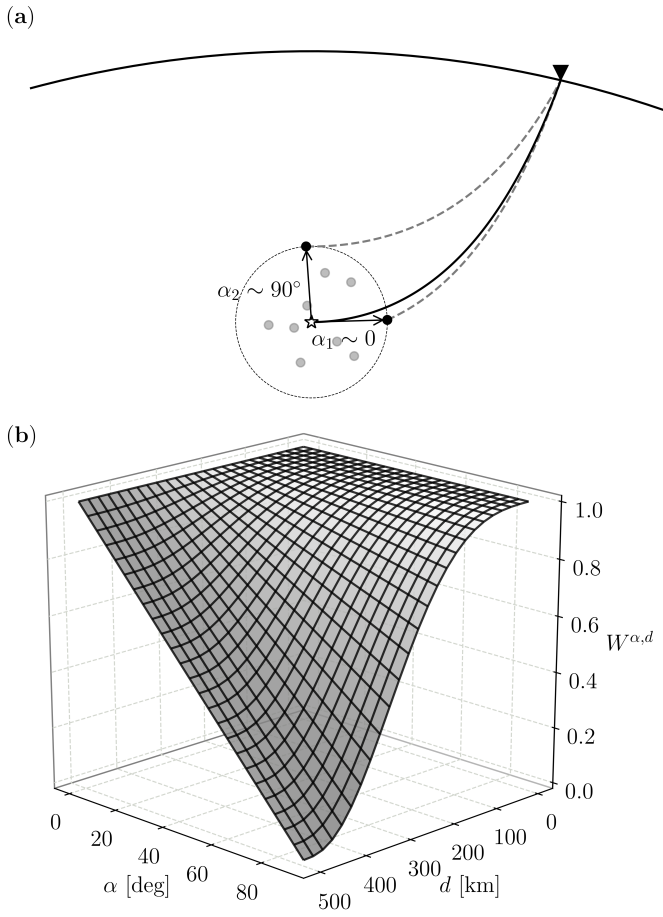

Figure 4.3: Illustration of the effective distance weighting function. (a) Schematic description of the opening angle, α, between the relative position vector of neighbouring event and the ray take-off direction computed at the target event location (solid line) with respect to the recording station. (b) Surface representing effective inter-event distance weights as a function of inter-event distance, d, and opening angle, α.

$$W_i^{\alpha,d} = 1 - \left(\left(1 - W_i^d \right) \cdot \frac{\alpha_i}{90} \right), \tag{4.1}$$

where W_i^d is a bi-cubic function stated as below:

$$W_i^d = \left(max \left\{ 0, 1 - \left(\frac{d_i}{R} \right)^3 \right\} \right)^3. \tag{4.2}$$

In this way, reference events whose relative position vectors are along the ray take-off direction ($\alpha \sim 0$) are given higher weights, since they share more common ray paths with the new event outside the focal area, regardless of their distance to the new event. This weighting approach is specially useful in our global relocation test where seismic rays leave the sources at different angles relative to the new event ray take-off direction.

4.3.2 Assessment of errors

We evaluate location errors by creating 10 random realizations of the arrival times for each validation event with a specified number of regional and teleseismic picks. When a large chunk of arrival times are observed at a limited azimuthal range, random sub-sampling of data will frequently result in network configurations with large azimuthal gaps. This causes

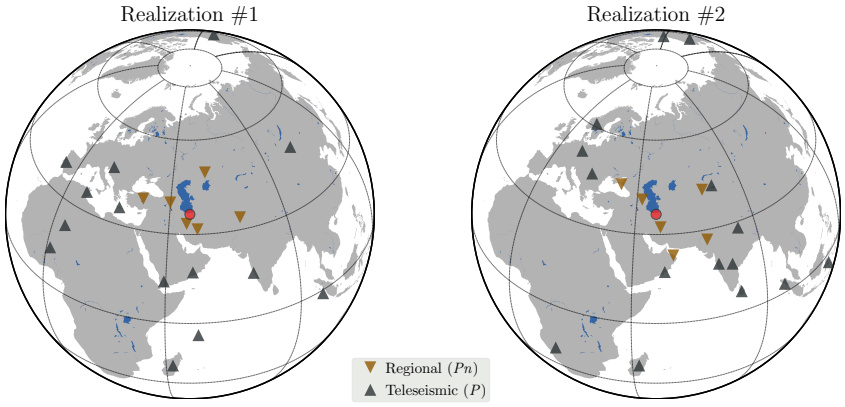

Figure 4.4: Example of two random network realizations. In this example, 6 *Pn* and 15 *P* arrivals are randomly selected from a larger pool of arrival data. Event location reported in the ISC-EHB catalogue is shown by red circle.

poor location regardless of the use of the travel-time corrections. To diminish this potential problem, we divide the seismic network into three circular sectors of 120° and randomly select a sector first, then randomly pick an arrival time from the selected sector.

The difference between GT and relocated epicenters is our metric to assess the location errors. We calculate the median epicenter error for 10 network realizations for all validation events as error for the specified number of regional and teleseismic observations. Moreover, to estimate the epicenter bias, vector averages are computed for the 10 realizations for each event. Then, the scalar bias for each event is averaged for the specified number of regional and teleseismic data. We do not use depth and origin time as metrics on account of the trade-off between these two parameters, particularly when crustal events are located using *P*-wave data alone.

Figure 4.4 shows two of the 10 realizations and travel-time residuals for the estimated locations. Vector mislocations for the 10 network realizations and summary statistics are shown in Figure 4.5. In this example, 6 regional (*Pn*) and 15 teleseismic (*P*) arrival times are randomly selected from a larger pool of seismic phase observations. It can be seen that the median epicenter error is significantly smaller when deterministic travel-time corrections are applied. Moreover, epicenter vector errors are more randomly oriented, which indicates the lack of significant bias.

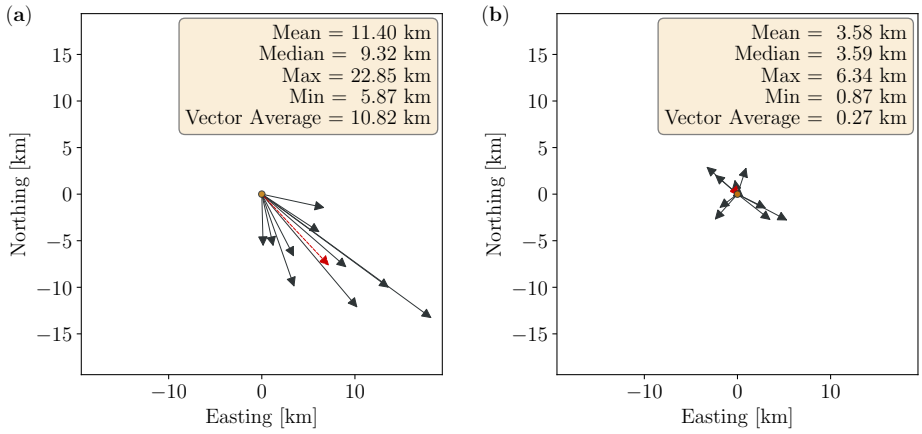

Figure 4.5: Vector mislocation for 10 network realization including summary statistics for the example event and seismic network configuration shown in Figure 4.4. (a) Single-event location, and (b) relative relocation using travel-time correction terms. Median vector epicentre error is shown by red dashed arrow.

4.4 Results

4.4.1 Epicentre error

It is well known that travel-time prediction error, phase picking error, station azimuthal gap, and the number of observed arrival times all affect earthquake epicentre error. Here, we report on average epicentre error and the vector average of epicentre error when either original arrival times or corrected arrival times are used to locate events and other variables are held constant. Average epicentre error provides an estimate of expected error for future earthquakes if similar data sets and station configurations are used, and vector average of epicentre error gives a measure of location bias.

Figure 4.6 shows the median epicentre error for validation events that are located using varying numbers of regional *Pn* and teleseismic *P* arrival times. Epicentre error is expected to decrease by increasing the number of observation data at a rate related to the inverse square root of the number of data (Myers et al., 2015), and epicentre errors in Figure 4.6 follows just such a relationship. Epicentre error decreases with faster rate until about 20 *Pn* or *P* arrivals are used to constrain location. Stabilization of epicentre accuracy occurs both because model-dependent errors are averaged and network azimuthal gap decreases. The level of accuracy for locations that are constrained by more than 20 *Pn* or *P* arrivals is between 9.5 and 10 km when events are located routinely (original phases), and between 6 and 6.5 km when they are relatively located (adjusted picks), which is a reduction in epicentre error of approximately 30 per cent. Moreover, it can be seen that the percentage reduction in epicentre error steadily increases when travel-time corrections are applied to more arrival data. This is a promising result for global seismic monitoring because it means that more accurate epicentre location can be determined by bringing more first-arriving *P*-wave data to influence a location if deterministic correction terms are added to the travel times predicted through global 1-D model.

3-D histograms of average epicentre error for combinations of *Pn* and *P* arrivals are shown in Figure 4.7. Using our relocation procedure reduces the average epicentre error relative to routine single-event location for every combination of *Pn* and *P* arrivals tested. The prominent trend in the Figure 4.7a (routine location without any correction terms) is increasing epicentre error when no teleseismic *P* phases are used and the number of regional *Pn* arrivals increases. In the absence of teleseismic data, *Pn* arrivals tend to increase the 1-D model epicentre error. However, when the condition is the same but travel-time path corrections are used through our relocation process, epicentre location error steadily decreases. This supports the conclusion that the relocation method presented here has the potential to improve the epicentre location in near real-time processing and enhance the ability to locate the lower magnitude events that are only recorded regionally.

Here, we report median vector epicentre error (MVEE) as a measure of epicentre location bias. When the direction of epicentre errors is random, MVEE will be closer to zero than when epicentre errors tend to be biased (i.e. almost in the same direction). Location bias is predominately caused by correlated travel-time prediction errors (Bondár and McLaughlin, 2009), that are related to the assumed velocity model errors (Rodi and Myers, 2013). Therefore, it can be concluded that reduced location bias is an indicator of reduced model-dependent errors of calculated travel times.

Figure 4.8 shows MVEE as a function of the number of regional *Pn* or teleseismic *P* arrivals. MVEE for *Pn* data and global 1-D model ak135 is observed to start to slightly increase when more *Pn* arrivals are used. This is a strong support for the conclusion that using global 1-D models and regional data can result in location biases. Unlike the routine location results, MVEE for our relative relocation continues to decrease with increasing

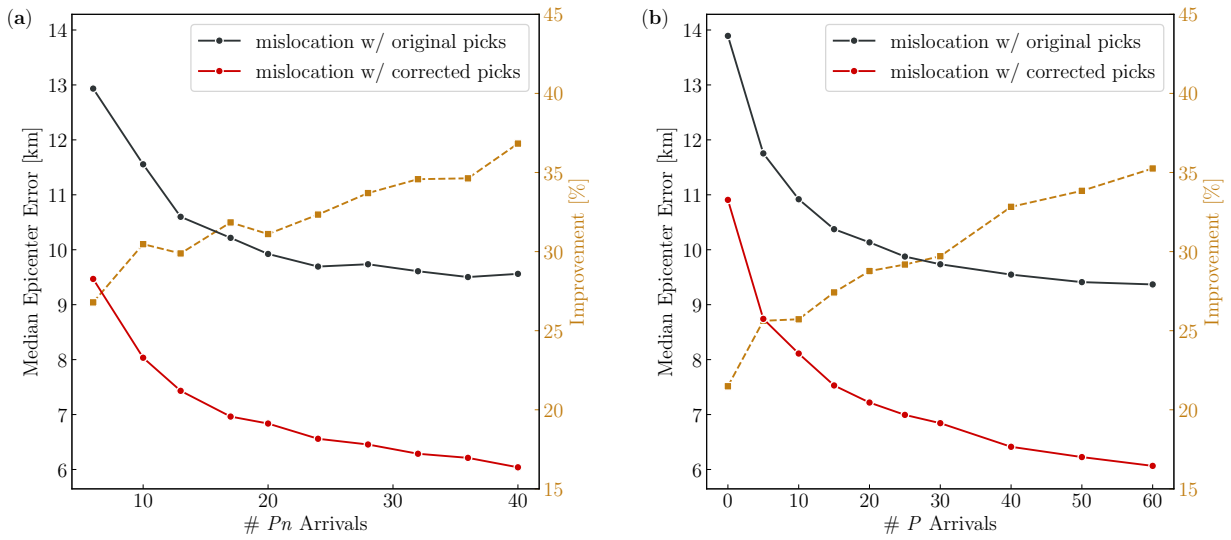

Figure 4.6: Curves of median epicentre errors as a function of (a) the number of regional *Pn* and (b) the number of teleseismic *P* arrival times. The percentage improvement in epicentre error is also shown in dashed line (right ordinate).

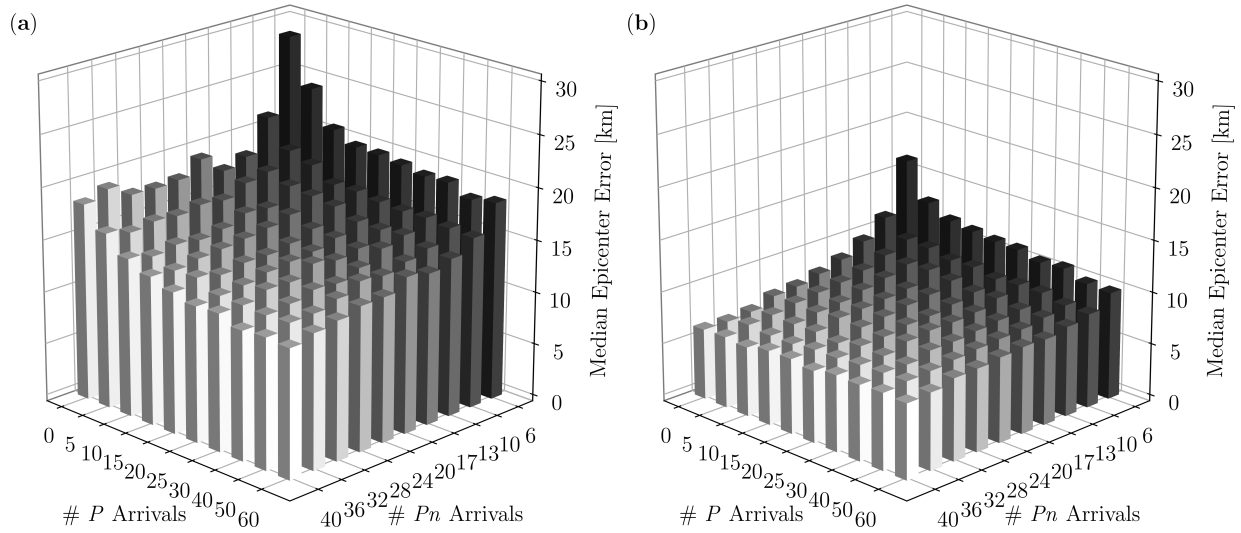

Figure 4.7: Histogram of median epicentre errors versus number of *Pn* and *P* phases (a) routine single-event location, and (b) relative relocation using travel-time correction terms.

number of *Pn* arrivals. Moreover, the percent improvement in MVEE steadily increases from approximately 25 per cent (20 per cent) for 6 *Pn* (5 *P*) arrivals to almost 35 per cent (32 per cent) for 40 *Pn* (60 *P*) data. Similar to median epicentre error results, MVEE for relocated validation events is reduced by approximately 30 per cent with respect to routine single-event locations.

Histograms of MVEE versus combinations of *Pn* and *P* data are shown in Figure 4.9. MVEE is lower for relocated events than routine locations in all cases, and the overall topology of the histogram surfaces are similar to those observed for median epicentre error (Figure 4.7). This result suggests that the more accurate, unbiased locations can be determined using the relocation process introduced here.

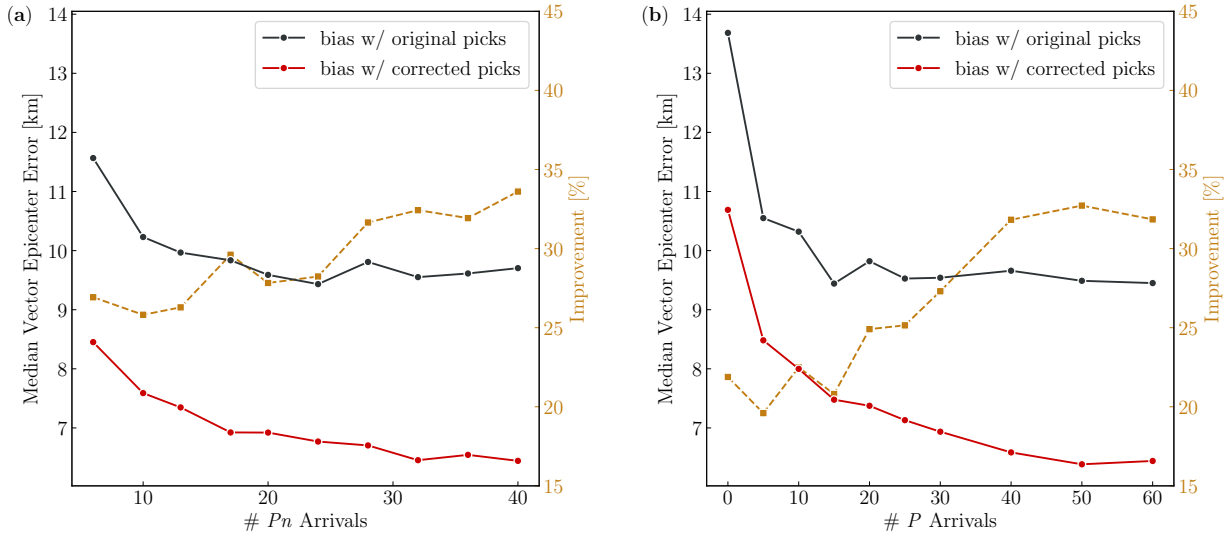

Figure 4.8: Curves of average median vector epicentre error (MVEE) as a function of (a) number of *Pn* and (b) number of *Pn* arrivals. The percentage improvement in epicentre error is also shown in dashed (right ordinate).

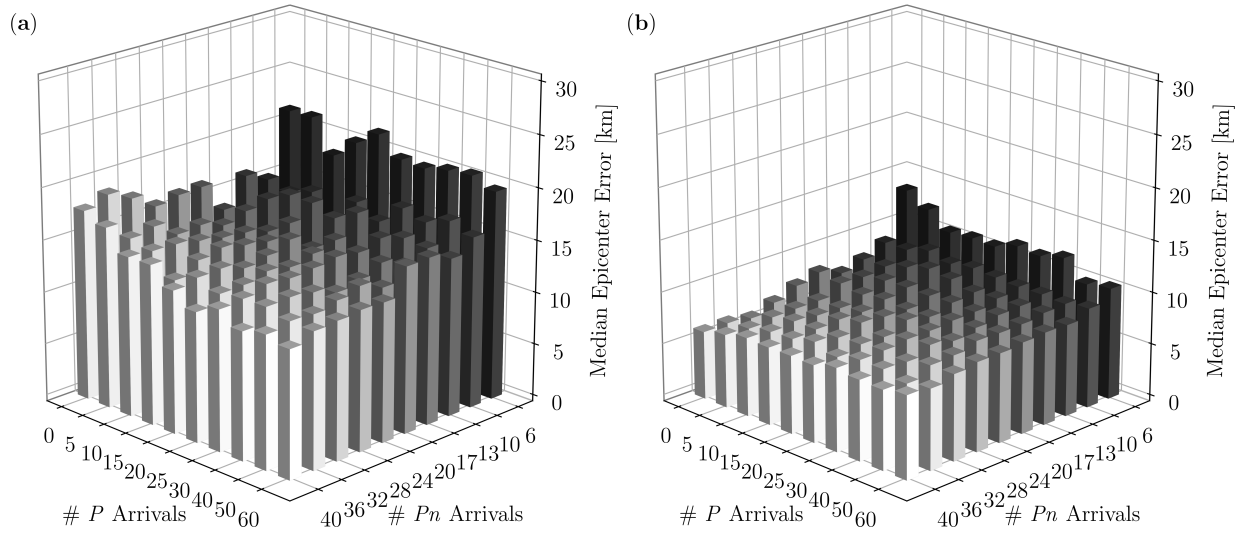

Figure 4.9: Histogram of median vector epicentre error (MVEE) versus number of *Pn* and *P* phases (a) single-event locations, and (b) relative relocation using travel-time correction terms.

4.4.2 Travel-time residuals

Travel-time residual analysis as a function of event-station distance is shown in Figure 4.10. The spread of the *Pn*-wave residuals for routine, single-event locations rapidly increases with distance from events and peaks in the triplication distances ($\Delta \geq 13°$). At teleseismic distances, the spread of the *P*-wave residuals decrease and remains approximately constant (stationary) out to 94°. The *Pn* residuals for relative locations exhibit a small increase in spread in the triplication distances, but the trend is far weaker than it is for single-event locations. At this distance range, relative residuals are dramatically reduced compared to single-event location residuals. relative residuals are smallest at teleseismic distances (*P*-wave residuals), and the residuals are approximately stationary throughout this distance range.

Figure 4.11 shows a comparison of the histograms of the *Pn*- and *P*-wave travel-time

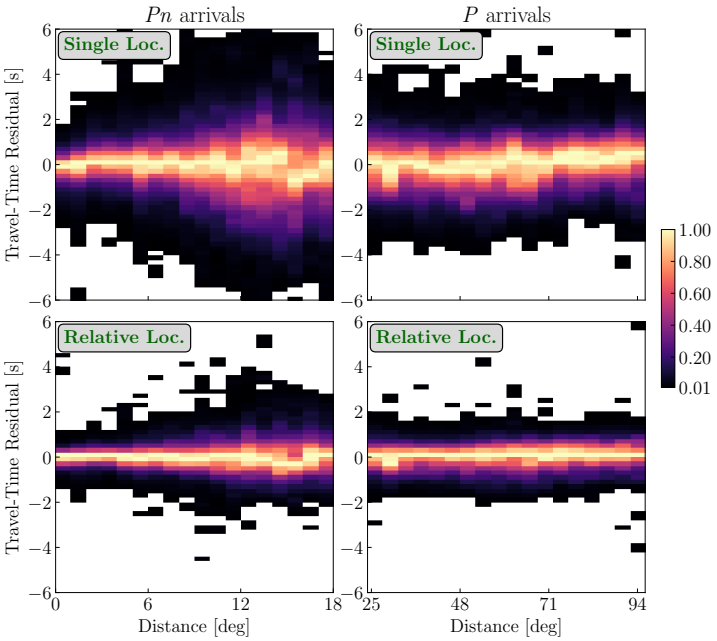

Figure 4.10: Frequency of occurrence (heat plots) of travel-time residuals for (top) single-event and (bottom) the relative locations. The heat plots are normalized in each distance range so that the residual bin with the largest number of hits (the scaling cell) is assigned a value of 1. All other bins in that distance range are linearly scaled from zero to one by dividing the number of hits by the number of hits in the scaling cell. Bins with zero hits are assigned no color (and they are transparent).

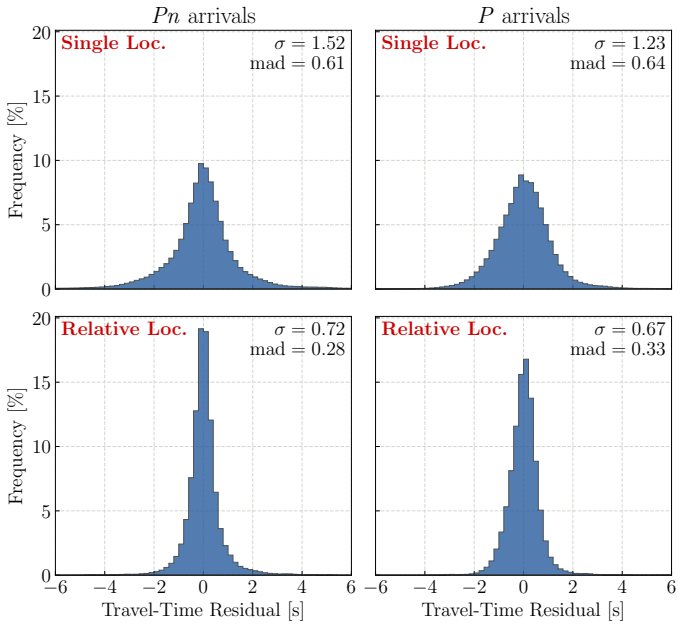

Figure 4.11: Histograms of travel-time residuals from (top) single-event locations, and (bottom) relative relocations. The sample standard deviation (σ), and median absolute deviation (MAD) of each distribution are indicated on each sub-plot.

residuals for the single-event locations and relative locations. The standard deviation (σ) and median absolute deviation (MAD) of each distribution are indicated on each sub-plot. The MAD is a measure of spread that is less sensitive to outliers in the data set than the standard deviation and so often more appropriate in the presence of non-Gaussian errors. A substantial reduction of spread is observed after relative relocation, which leads to the MAD reduction of 54 per cent and 48 per cent for *Pn* and *P* residuals, respectively.

4.5 Concluding remarks

We have successfully designed and tested a relative relocation process that implements a simulation of near real-time location of new earthquakes relative to a high-resolution data set of past seismicity. The locations of 103 back-testing GT events represent a considerable improvement over the corresponding routine locations. We achieve epicentre location improvement of approximately 30 per cent. Epicentre locations improve in all areas. The increase of the percentage reduction in epicentre error when more arrival times are available is one of the highlights of the obtained results and is a promising result for global seismic monitoring and near real-time processing. More accurate epicentre locations can be determined by bringing more arrival time data to bear on a routine location if the proposed relocation approach is used. Moreover, our relocation results revealed that, in the absence of teleseismic picks, the epicentre error continues to decrease with increasing number of regional arrivals. This strongly supports the conclusion that our relocation process can be used to locate smaller magnitude events, that are recorded regionally, with higher accuracy, or where fast location based on regional stations is needed. Similar to median epicentre error results, median vector epicentre error, which is a measure of location bias, for relocated validation events is reduced by approximately 30 per cent with respect to routine single-event locations. Furthermore, residual statistics show a strong reduction (∼48–54 per cent) of travel-time residual MAD, reducing the biasing effects of lateral velocity heterogeneities. In out test-bed implementation, the final solutions are computed within a few tens of seconds (in less than a minute) after receiving the initial locations and phase information. New events that occur in areas of dense seismicity with numerous strongly correlated reference events may take longer because of additional time spent on accessing a larger set of nearby events and selecting a sub-set of suitable reference events.

Having critical event density near a new seismic event to achieve high-precision location is crucial in this approach. The precision with which new events are located using this technique will improve with time, helped by the continued increase in density of recorded earthquakes and growth of high-resolution seismic archives such as ISC-EHB bulletin used in out test-bed. The year-over-year increase in the number of reference events in any given area is a main contributor to the increase in location precision as well as the feasibility of applying this approach to many new events.

A difficulty with using the method in (near) real-time is that the location solutions for new events are dependent on all linking reference events. In principle, the locations of all previous nearby seismicity would be affected by a newly added event, and the whole catalogue would have to be relocated whenever a new event is added. A reasonable compromise is to periodically relocate the entire catalogue, e.g. once per year, to generate a new, updated base catalogue. During these periods, new events can be relocated while holding all prior events in the base catalogue fixed. Periodic catalogue relocation guaranties that the locations of events in the base catalogue, which do not change once that catalogue has been established, are adequately represented by the data of newer events.

The location procedure presented here could be modified to work in any region where a sufficient pick archive exists. Such an approach has the benefit of being able to be implemented, tested, and evaluated while assuring the uninterrupted and consistent production of catalogues and bulletins during existing routine network operations. Future work will be dedicated to full integration of the relocation process into the real-time system such as GEOFON seismological infrastructure to allow a more seamless interaction with the existing databases and archiving systems for more comprehensive data mining purposes.

Chapter 5

Source time function and depth estimates of seismic events

The material presented in this chapter has been published in the following article:

Gaebler, P., Ceranna, L., **Nooshiri, N.**, Barth, A., Cesca, S., Frei, M., Grünberg, I., Hartmann, G., Koch, K., Pilger, C., Ross, J. O., and Dahm, T. (2018): A multi-technology analysis of the 2017 North Korean nuclear test. *Solid Earth*, 10(1):59–78. doi:10.5194/se-10-59-2019.

This chapter describes the procedure developed by myself for the simultaneous inversion of the source time function and hypocentre depth, and its application to the 2017 North Korean nuclear test, also including seismological moment tensor analysis to which I contributed. The full multi-disciplinary paper is provided in Appendix B.

Abstract

We developed and implemented an inversion method to determine source time function and focal depth of seismic sources using direct waveform fitting. It uses theoretical Green's function and a time-domain deconvolution to estimate the source time function from the teleseismic P waveforms. The source time function is discretised by using a set of orthogonal basis functions, so that the method does not impose constraints on the source process and therefore can be applied to seismic events with different mechanisms, such as tectonic earthquakes, explosions, and cavity collapses. The depth of the seismic event is also determined in the process by using a grid search approach, where the depth of the point source Green's functions is sampled at different depths and the waveform misfits for every depth solution are estimated and stored for final evaluation. We applied this method to estimate the source time function and hypocentre depth of an abnormal seismic event, the 2017 North Korean nuclear test, using high-frequency array beam waveforms. The results suggest at least a partial collapse of the explosion cavity immediately after the explosion and a centroid depth between 400 and 800 m, which are in good agreement with the results of several other independent studies.

5.1 Introduction

Seismic moment rate function – often referred as source time function (STF) – offers an integrated view of the seismic source process. Its duration and peak value are used to infer the global characteristics of the seismic event and in particular stress or strain drop (Tocheport et al., 2007; Vallée, 2013). Moreover, it contains the broad-band spectrum of the source process, therefore it can be used to calculate the radiated energy (Vassiliou and Kanamori, 1982), and to explore how the source spectrum behaves with respect to theoretical models (Aki, 1967, 1972). STF is therefore an efficient tool to quickly determine abnormal seismic events such as the tsunami earthquakes and nuclear explosion tests, for which the seismic moment and radiated wave energy obey a different scaling compared to tectonic earthquakes.

STF is closely related to the seismic waveforms (e.g. P waves) observed at teleseimic distances (epicentral distance range of $30° - 90°$). It is well known that in an infinite medium without attenuation and for a point source representation, STF is directly the P-wave displacement scaled by the radiation pattern and propagation properties (Lay and Wallace, 1995). Therefore for depths such that the end of the seismic rupture occurs before the arrival of surface-reflected waves (the so-called depth phases pP and sP), resolving the STF is relatively straight forward. When the earthquake is shallow, the direct P-wave interferes with pP and sP waves creating a more complex P-wave train and adding difficulties to the STF extraction. In this case, STF has to be determined together with earthquake depth. The modelling of the wavelet consisting of depth phases and STF can potentially help in such a case.

Thanks to this close link with the observed seismograms, STF is known to be one of the most robust characterisation of the seismic source process and has the potential to be provided rapidly and routinely. Here, we present a method for STF and depth estimation of seismic sources from a set of teleseismic body-wave records directly through waveform fitting. As the shape of underlying STF is never known in reality, we parametrise the STF as a weighted sum of multiple orthogonal basis functions to determine the actual shape of the STF. The inversion method can be applied for fast and accurate estimates of STF and depth of moderate-size seismic events. Moreover, to circumvent the difficulty of depth phase identification arising for shallow earthquakes, we perform array beamforming for teleseismic depth phase analysis (Kriegerowski et al., 2016) to enhance the signal-to-noise ratio (SNR) at teleseismic distances. We use this inversion method to illustrate the potential of this technique for special event analysis and event screening by estimating the depth and STF of the 2017 North Korean nuclear explosion test.

5.2 Method

5.2.1 Parametrisation of the source time function

The displacement seismogram (e.g. vertical component) from a moment-tensor source at point $\mathbf{r}_s$ and observed at time t at a receiver with coordinates $\mathbf{r}_r$ is represented by (Madariaga, 2007):

$$u(t) = \sum_{jk} G_{j,k}(\mathbf{r}_s, \mathbf{r}_r, t) * M_{jk}(t), \tag{5.1}$$

where $*$ indicates time-domain convolution, $G_{j,k}$ are the spatial derivatives of the Green's function, $\partial G_j / \partial x_k$, and M_{jk} denotes the elements of the moment tensor. We define $\mathbf{M}_0(t)$ a symmetric tensor whose components are independent functions of time. Very often in

seismology it is assumed that the geometry of the source can be separated from its time variation, so that the moment tensor can be written in the simpler form:

$$\mathbf{M}_0(t) = \mathbf{M}m(t), \tag{5.2}$$

where $\mathbf{M}$ is a time-invariant tensor that describes the geometry of the source and $m(t)$ is the scalar source time function (STF), the time variation of the seismic moment determined by seismologists. In other words, it is assumed that all moment tensor components, M_{jk}, have the same time dependency, which is described as normalised moment function $m(t)$ with $m(t \to \infty) = 1$. For instance, the rupture along a planar fault, where the slip direction and magnitude would not vary with time, fulfils such a condition. Employing Equation 5.2, we can write Equation 5.1 as:

$$u(t) = \sum_{jk} M_{jk} G_{j,k}(t) * m(t). \tag{5.3}$$

The displacement in the far-field is controlled by the time derivative of $m(t)$, which is declared as moment rate function, $\dot{m}(t)$. This explains that the far-field body wave pulses from earthquakes are single-sided pulses (Dahm and Krüger, 2014). Since we are interested in only the far-field wave fields, the Green's function terms in Equation 5.3 are replaced by far-field Green's functions, $G^{(\mathrm{ff})}$, and $m(t)$ is replaced by $s(t) = \dot{m}(t)$. Here, we use the notation $s(t) = \dot{m}(t)$ for the source time function, the signal emitted by the source in the far field (Madariaga, 2007). The resulting formulation will be linear in $s(t)$, so that $s(t)$ can be determined by deconvolving the far-field Green's function from observed beam seismograms if the moment tensor, $\mathbf{M}$, is considered fixed. However, the real STF is always unknown and could be complicated. Utilizing a multiple time-window strategy, we parametrise $s(t)$ using half-overlapping triangular basis functions, $h(t)$, where each basis function is T s-wide and satisfies (Figure 5.1a):

$$\int h_l(t)\mathrm{d}t = 1, \tag{5.4}$$

to solve for a source time function of D duration ($M = 2D/T - 1$ basis functions) using displacement seismogram data. Parametrisation to solve for the weighting coefficients (amplitudes), β_l of the triangular basis functions, $h(t - \tau_l)$, where τ_l is the centre time of the l-th basis function, yields:

$$u(t) = \sum_{l=1}^{M} \beta_l \sum_{jk} M_{jk} G^{(\mathrm{ff})}_{j,k}(t) * h(t - \tau_l), \tag{5.5}$$

which is a linear inverse problem for β_l (heights of triangles in Figure 5.1b), and which models the actual shape of the source time function (blue curve in Figure 5.1b).

The discretised inverse problem can be written as:

$$\mathbf{d} = \mathbf{A}\boldsymbol{\beta}, \tag{5.6}$$

which is formulated in terms of a composite data vector, $\mathbf{d}$, of length NS, where N is the number of samples in each seismogram (beam waveform) and S is the total number of stations (arrays) in the data set, and a very sparse system matrix, $\mathbf{A}$, of size NS by M. The rows of matrix $\mathbf{A}$ are given by time-reversed responses of the system to appropriate unit-height basis functions, which are easily generated using convolution and time shift operations. Matrices like $\mathbf{A}$ in which the elements along diagonals are constant are called Toeplitz matrices (Horn and Johnson, 2012).

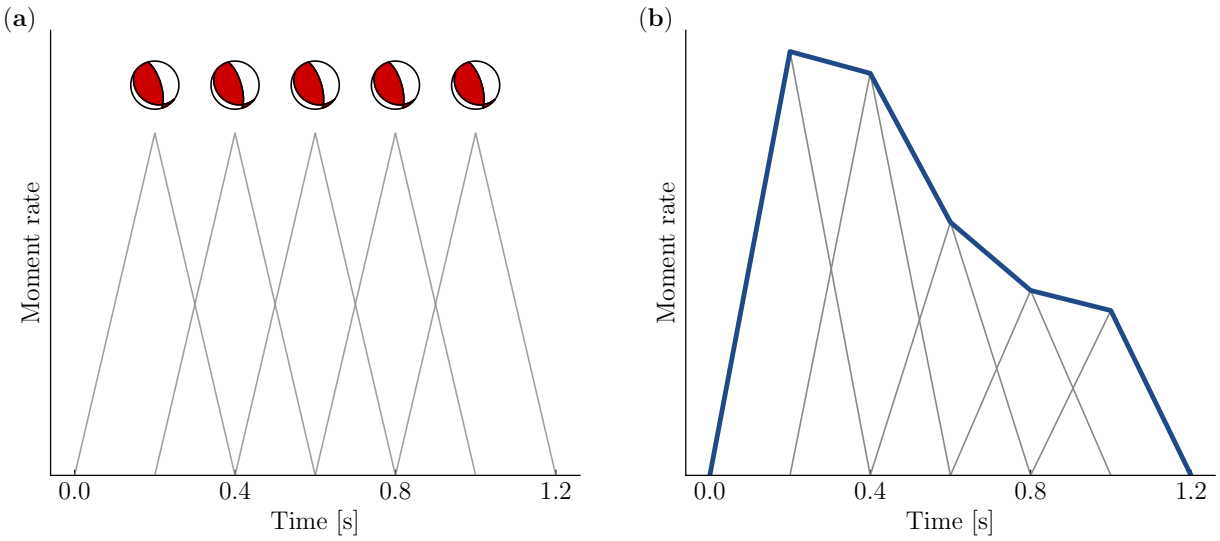

Figure 5.1: (a) Schematic sketch of five triangular basis functions $h_l(t)$ with equal weight of 1 and with a duration of $T = 0.4$ s each. The focal sphere symbols indicate that the orientation of the source mechanism is assumed constant during the rupture process. (b) Simulation of a complex moment rate function (blue line) by applying different weights to $h_l(t)$ and linear superposition.

The resulting system of equations is solved for the weighting coefficients β_l, assembled into the composite vector $\boldsymbol{\beta}$, in a least squares sense using the L_2 norm (Dahm and Krüger, 2014). However, because of the noise in the data and the sparsity of the forward operator, $\mathbf{A}$, we will not be able to solve Equation 5.6 exactly. Therefore, we need to regularise our solution to the inverse problem to obtain a model that has minimum norm and adequately fits the data. Moreover, we prefer to obtain a solution that minimises the norm of the second derivative of $\boldsymbol{\beta}$, reflecting a preference for a "smooth" source time function. We then solve the regularised least squares problem:

$$\min \left\| \begin{bmatrix} \mathbf{A} \\ \alpha\boldsymbol{\Gamma} \end{bmatrix} \boldsymbol{\beta} - \begin{bmatrix} \mathbf{d} \\ \mathbf{0} \end{bmatrix} \right\|_2^2, \tag{5.7}$$

where α is a regularization parameter, and $\boldsymbol{\Gamma}$ is a matrix used to differentiate $\boldsymbol{\beta}$ for the purpose of regularization commonly referred to as roughening matrix (Aster et al., 2013):

$$\boldsymbol{\Gamma} = \begin{bmatrix} 1 & -2 & 1 & & & & \\ & 1 & -2 & 1 & & & \\ & & \ddots & \ddots & \ddots & & \\ & & & 1 & -2 & 1 & \\ & & & & 1 & -2 & 1 \end{bmatrix}. \tag{5.8}$$

In Equation 5.7, $\boldsymbol{\Gamma}\boldsymbol{\beta}$ represents a finite-difference approximation that is proportional to the second derivative of $\boldsymbol{\beta}$.

Finally, we employ the generalised singular value decomposition, or GSVD (Hansen, 1998) to solve the regularization problem. The source time function is reconstructed from basis function weights as:

$$s(t) = \sum_{l=1}^{M} \beta_l h(t - \tau_l). \tag{5.9}$$

5.2.2 Picking the regularization parameter

The regularization parameter, α, determines the relative importance of the data residual and the penalty term (semi-norm term $\|\mathbf{\Gamma}\boldsymbol{\beta}\|_2$ in Equation 5.7). For all practical applications, a balance between them is sought in order to stabilise the solution, although this stability comes in the expense of limited resolution (i.e. fitting to the data). Various techniques have been proposed for proper selection of a regularization parameter without requiring *a priori* knowledge of the noise to obtain a regularised inverse solution (e.g. Wahba, 1990; Hansen, 1998). In geophysical problems, L-curve criterion has gained much attention for picking the value of the regularization parameter (e.g. van Wijk et al., 2002; Sen and Roy, 2003). When plotted on a log-log scale, the trade-off curve, the curve of regularised solution norm versus residual norm as α varies, often takes on a characteristic 'L' shape in linear– or linearised–inverse problems. The preferred regularization parameter is then chosen by estimating the so-called 'elbow' of the L-curve, which is the point of maximum curvature. It is a convenient graphical approach in which the L-curve is computed for a range of values of α by minimising the objective function for each value. In large-scale geophysical problems, this can be computationally intensive and expensive. Here, we follow the methodology of Belge et al. (2002) and use a minimum distance function (MDF) for fast and efficient approximation of the regularization parameter. MDF provides a simple and efficient fixed-point iterative algorithm that converges with only a few iterations.

The L-curve consists of the points with following coordinates:

$$x(\alpha) = \|\mathbf{A}\boldsymbol{\beta}_\alpha - \mathbf{d}\|_2, \tag{5.10}$$

$$y(\alpha) = \|\mathbf{\Gamma}\boldsymbol{\beta}_\alpha\|_2. \tag{5.11}$$

The MDF is defined as the distance from a properly selected origin (x_0, y_0) to the L-curve. The coordinate of the origin is selected as:

$$(x_0, y_0) = \left(\log\left[x(\sigma^2_{min})\right], \log\left[y(\sigma^2_{max})\right]\right), \tag{5.12}$$

where σ_{min} and σ_{max} denote the smallest and largest singular values of the forward operator, $\mathbf{A}$, respectively. Therefore, the distance function is defines as below:

$$r^2(\alpha) = \left|\log\left[x(\alpha)\right] - x_0\right|^2 + \left|\log\left[y(\alpha)\right] - y_0\right|^2. \tag{5.13}$$

The following iterative algorithm is then used to minimise the Equation 5.13 to find the optimum regularization parameter (Belge et al., 2002):

$$\alpha^{k+1} = \frac{y(\alpha^k)}{2x(\alpha^k)} \frac{\log\left[x(\alpha^k)\right] - x_0}{\log\left[y(\alpha^k)\right] - y_0}, \tag{5.14}$$

where α^k is the regularization parameter in k-th iteration. The algorithm starts with initial value $\alpha^0 \in [\sigma^2_{min}, \sigma^2_{max}]$ and runs until the $|\frac{\alpha^{k+1}}{\alpha^k} - 1|$ becomes less than a given tolerance. Figure 5.2 shows an example L-curve together with the origin point (x_0, y_0) and the distance function $r^2(\alpha)$. It can been seen that the selected regularization parameter (indicated by the red circle on the curve) minimizes the $r^2(\alpha)$ function.

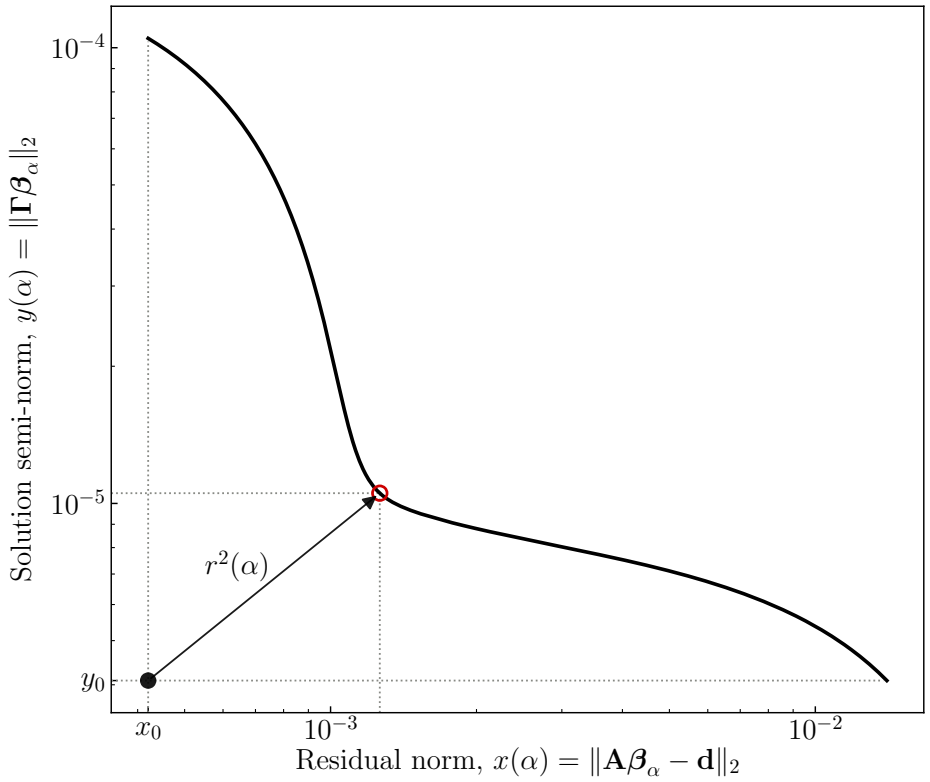

Figure 5.2: Example L-curve together with the origin point (x_0, y_0) and the distance function $r^2(\alpha)$. The red circle on the curve indicates the optimal regularization parameter selected using MDF algorithm.

5.3 Application to the 2017 North Korean nuclear test

On 3 September 2017 official channels of the Democratic People's Republic of Korea announced the successful test of a thermonuclear device. Only seconds to minutes after the alleged nuclear explosion at the Punggye-ri nuclear test site in the mountainous region in the country's north-east at 03:30:02 (UTC) hundreds of seismic stations distributed all around the globe picked up strong and distinct signals associated with an explosion. Different seismological agencies reported body wave magnitudes of well above 6.0, consequently estimating the explosive yield of the device in the order of hundreds of kilotons TNT equivalent. The 2017 event can therefore be assessed being multiple times larger in energy than the two preceding North Korean events in January and September 2016. This would be a major step in the nuclear program of North Korea. From a scientific point of view, therefore, the depth of the event, its strength in terms of radiated high- and low-frequency seismic energy, and the near-surface damage in the test area are key questions to be answered. In the following, we try to approach these questions based on the modelling technique described before. As there is no easy concept to verify and characterize nuclear explosions, especially in a country where direct observations are difficult to assess, results obtained in this study demonstrate and emphasize the screening capabilities of the applied method for dealing with unusual or suspect events.

5.3.1 Moment tensor inversion of the nuclear test

Seismic signals of the 2017 North Korean test show a great similarity to those generated by the previous four nuclear tests conducted in 2009, 2013, and 2016. Especially long period waveforms with periods above 10 s recorded at regional distances show a high waveform

similarity and a substantially increased amplitude, revealing a very similar radiation pattern of all events and a larger moment release for the 2017 nuclear test. In recent years, MTIs have been performed for nuclear tests in North Korea, including those carried out in 2009, 2013 and 2016 (Ford et al., 2010; Barth, 2014; Vavryčuk and Kim, 2014; Cesca et al., 2017; Hartmann et al., 2017). All MTI were performed by fitting low-frequency full waveform seismic data at regional distances, either in the time or in the frequency domain. The majority of these solutions revealed a significant positive isotropic component. For the 2013 nuclear test an extraordinary high double couple (DC) component was found, indicating differences in containment or near source damaging effects (Barth, 2014; Vavryčuk and Kim, 2014). For the 2017 test the seismic moment tensor is inverted by fitting the low frequency amplitude spectra (epicentral distances up to 1200 km) and full displacement waveforms (epicentral distances up to 600 km) in the frequency range from 0.02 to 0.04 Hz following the approach by Cesca et al. (2013, 2017). For the moment tensor optimization the *Grond* algorithm (Heimann et al., 2018) is used, which searches the parameter space by random search first and later by an increasingly denser search around the best solutions. The algorithm finally resolves the full moment tensor components, the centroid location and centroid time, and also provides information on model uncertainties and source parameters trade-offs. Full waveforms and their spectra are calculated assuming a layered crustal model proposed by Ford et al. (2010). Example full waveform displacement and amplitude spectra fits are shown in Figure 5.3.

The moment tensor solution for the 2017 test shows a dominant positive isotropic part of 60%, 16% positive compensated linear vector dipole (CLVD), and 24% of DC. The best solution, found at a depth of around 2 km, has a scalar moment of 2.33×10^{17} Nm, equivalent to an M_W of 5.55. The centroid depth is poorly resolved and good waveform fits are found for very shallow sources down to 2.5 km. This result confirms the very shallow depth of 400-800 m accurately resolved by the analysis of depth phases in Subsection 5.3.2. The moment tensor optimization resolves a broad ensemble of well fitting moment tensor solutions. They are plotted using a source type diagram in Figure 5.4 and are characterized by strong deviations from a pure DC model (mapping in the center of the diagram), a typical model for tectonic earthquakes. Instead, acceptable solutions are either dominated by a positive isotropic component (positive values of the y-axis in the plot), a negative vertical CLVD (positive values of the x-axis), or a combination of both. The variability among these type of solutions has been attributed to trade-off among moment tensor components for very shallow sources (Cesca and Heimann, 2017; Cesca et al., 2017). This range of moment tensor solutions includes alternative moment tensor configurations as proposed for previous nuclear explosions in North Korea (e.g. Barth, 2014).

In the aftermath of the nuclear test, a seismic event took place in its direct vicinity around eight minutes later. The estimated scalar moment and M_W are 1.88×10^{16} Nm and 4.81, respectively, and thus the scalar moment is only ∼8% of the one of the nuclear test.

5.3.2 Estimation of hypocentre depth and seismic moment

The source depth is needed to estimate the explosion process and strength of the seismic source. However, constraining the depth of a shallow source is difficult from regional and teleseismic data without a close station within a focal depth's distance from the source. The modelling of the wavelet consisting of a surface-reflected P-phase, so-called depth phase, and STF can potentially help in such a case. Such a wavelet modelling approach resembles the inverted and time-shifted STF and needs high-frequency waveforms above 1 Hz to resolve the onset of the depth phase, and may be difficult to be performed from single station recordings

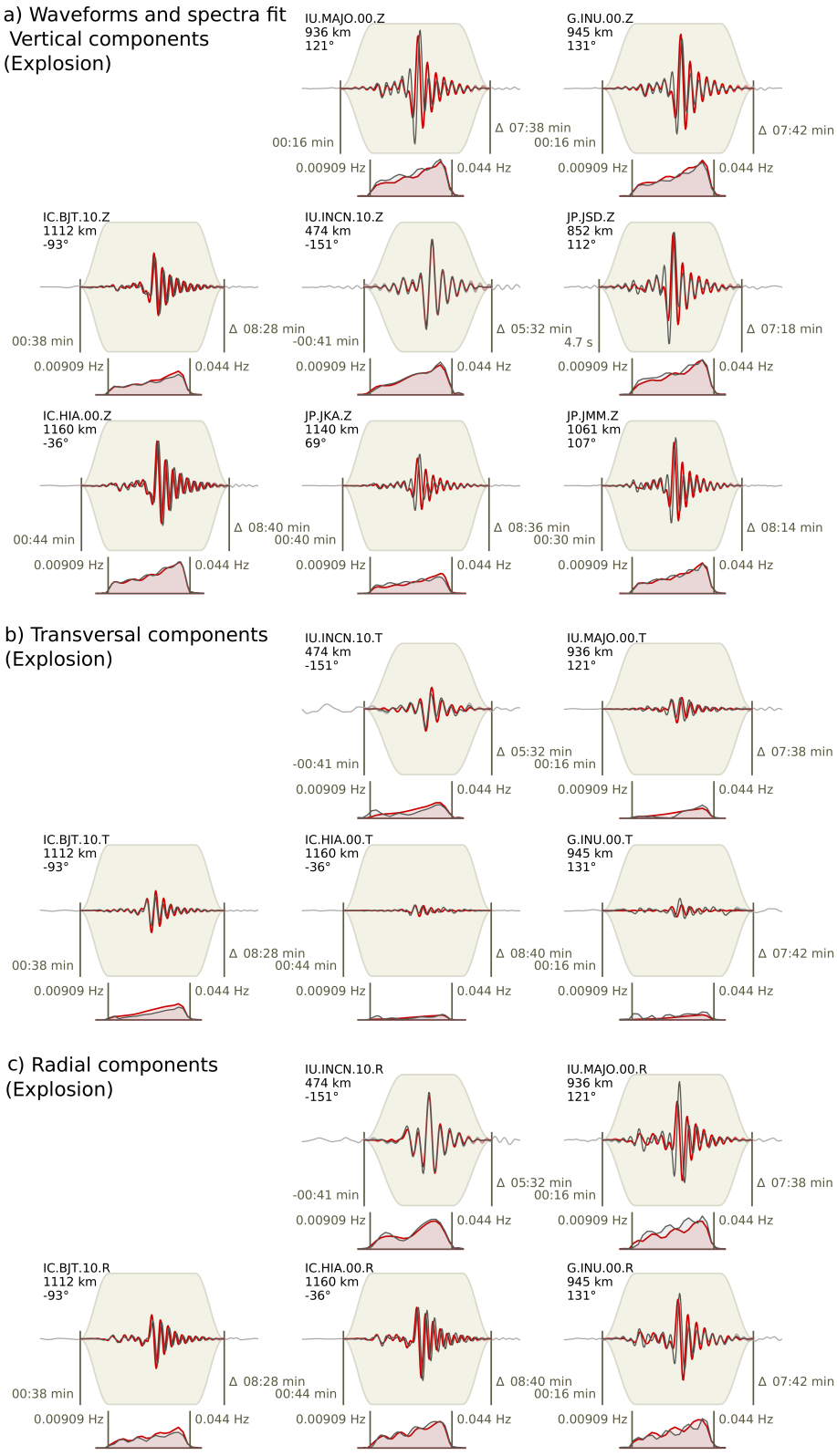

Figure 5.3: Full waveform displacement and amplitude spectra fits (gray and red lines denote observations and synthetics, respectively) are shown for the nuclear explosion for the vertical (a), transversal (b), and radial components (c). Top left side of each plot reports the trace component (network, station, location, and component codes), epicentral distance, and azimuth. Waveform plots report the starting time (relative to the origin time) and duration (in minutes and seconds) of the time window used (the gray background represents the applied taper), while spectra plots report the frequency range in Hz.

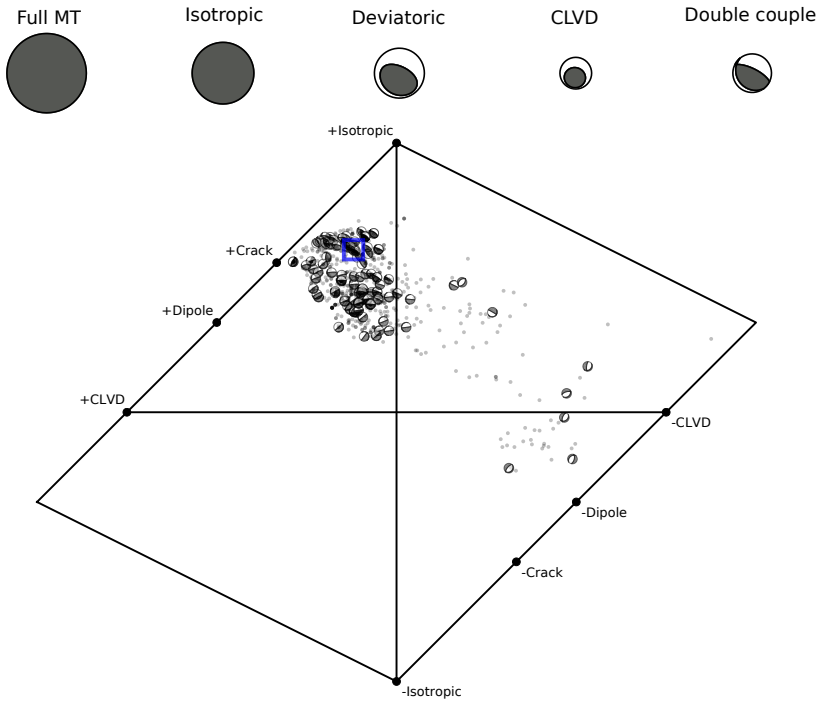

Figure 5.4: (top) Best moment tensor decomposition. The moment tensor decompositions reports the focal sphere for the full moment tensor, and its isotropic and deviatoric components. The deviatoric component is further decomposed into CLVD and DC terms. The relative size of focal spheres scale with their relative magnitude. (bottom) Source type plots. The source type diagram after Hudson et al. (1989) is used to judge the moment tensor decomposition, illustrating the ensemble of best fitting solutions. Figure shows both solutions based on all available data, as well as using data sub-samples upon bootstrapping. The position of each solution (circles, focal sphere for selected solutions) illustrates the MT decomposition, while the focal spheres (shown for selected solutions only) illustrate the geometry of the DC term. The decomposition of the best solution is denoted by a blue square.

if the signal to noise ratio (SNR) is poor at teleseimsic distances. An approach uncommon for nuclear test studies is used, which was established for the analysis of induced seismicity, where waveform beams are calculated at several small-aperture, short-period arrays to enhance the SNR (Figure 5.5a).

The beam waveforms represent a superposition of direct and reflected waves. Using our method, we are able to estimate the depth of the explosion and the underlying STF by comparing observed and synthetic beam waveforms (Figure 5.5d), which are calculated for the best moment tensor solution described in Subsection 5.3.1, a common STF and varying depths.

Calculated Green's functions depend strongly on source depth, so that a misestimation of source depth will strongly distort the shape of the STF. Therefore, the STF is inverted for every single trial depth. The length of the STF is constrained to 1.5 s, where 0.5 s are considered before the arrival of the *P*-wave. It should be noted that, with shorter length of STF, the details of the STF with a complex structure are difficult to resolve. On the other hand, with longer length of the STF, i.e. larger number of basis functions, the fitted curve oscillates wildly and gives a very poor representation of the model, which is known as over-fitting. The length of the STF mentioned before was chosen to reach a compromise, after examining the residual misfit in total signal variance computed for different lengths of source time function. In order to compensate travel-time residuals occurring along the mantle ray, zero-lag Green's functions are correlated with *P*-wave beams at every array, and the travel-time corrections are considered before the inversion. The source depth itself

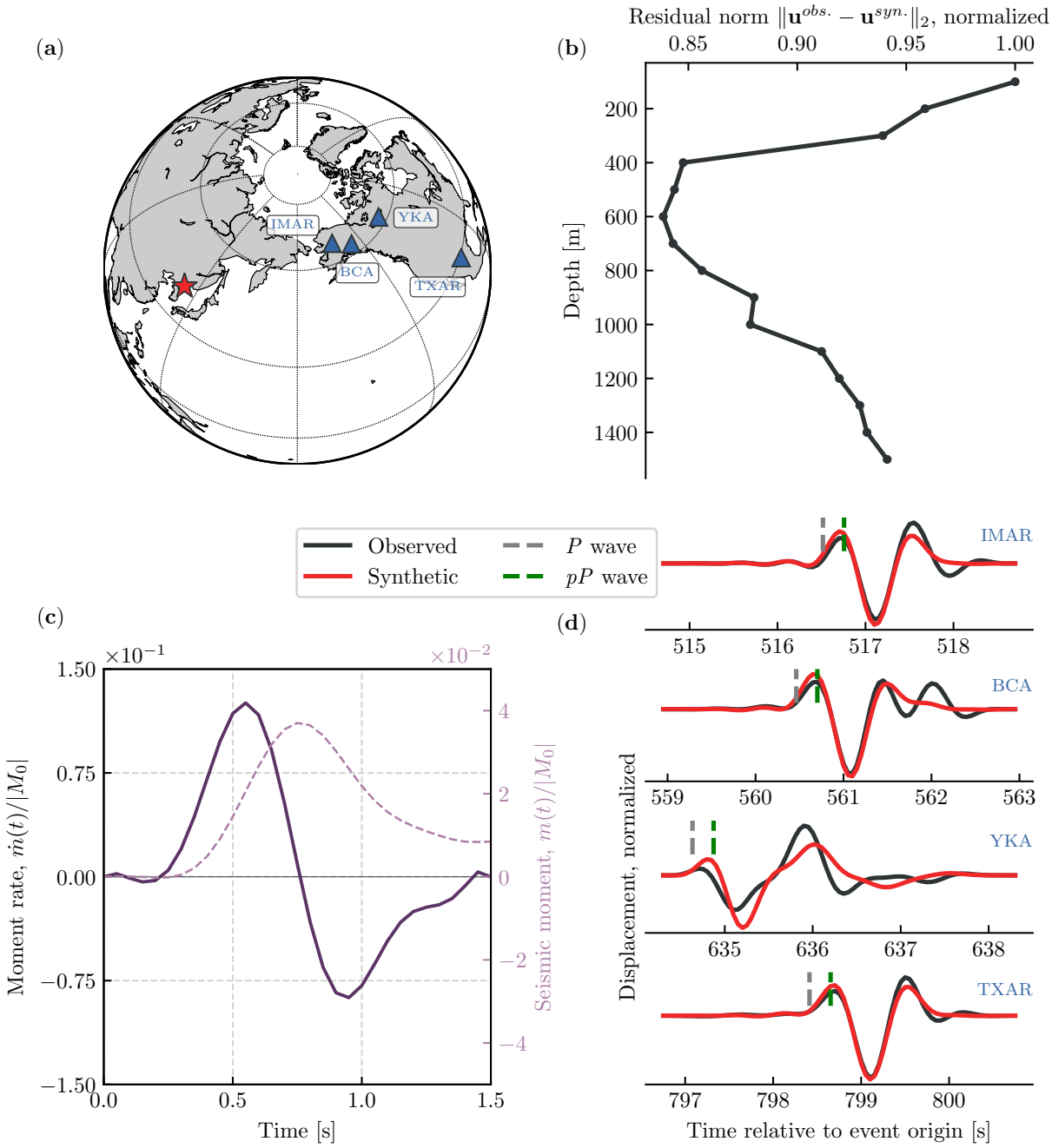

Figure 5.5: (a) Setup of the depth analysis with the 2017 North Korean nuclear test marked as red star and the four small-aperture, short-period arrays marked as bluish triangles. The epicentral distances to arrays IMAR, BCA, YKA and TXAR are 48°, 54°, 65° and 94°, respectively. (b) Residuals between observed and synthetic waveforms (L_2- norm) as a function of depth of the explosion. (c) Least squares source time function associated with the best-fit regularized solution. Solid and dashed lines are the normalized moment rate and moment function, respectively. (d) Observed (black) and synthetic (red) waveforms for the best-fit regularized solution at 600 m depth. The gray and green dashed lines indicate the theoretical arrival times of the P- and pP-phases, respectively. The traces are bandpass-filtered between 0.5 and 2.5 Hz.

is estimated using a grid search approach, where the depth of the point source Green's functions is sampled from 0 to 1500 m in 100 m steps. For every depth solution the residuals are estimated and stored for final evaluation.

Green's functions are calculated using the code QSEIS (Wang, 1999), where source and station specific crustal models can be considered. 1-D global velocity model ak135 (Kennett et al., 1995) is used for the mantle, while different crustal profiles for source and station

regions are taken from CRUST2.0 (Bassin et al., 2000). Intrinsic attenuation for P-waves is manually set to a large value, since otherwise high frequencies are damped out at teleseismic distances. The sampling frequency is 20 Hz. The grid search depth phase modelling has been applied previously to different cases of induced seismicity (Dahm et al., 2007) and the 2016 nuclear explosion (Cesca et al., 2017), but the simultaneous STF inversion is implemented for the first time in this study.

The full waveforms of beams, their peak heights and peak distances are well fitted in a joint inversion of four arrays. The best fits are obtained at depths between 400 to 800 m (Figure 5.5b). However, it should be noted that the depth value obtained from the inversion procedure might be overestimated due to the use of an unperturbed velocity model. Perturbations in the velocity model for example through potential fracturing above the explosion, which would substantially reduced P-wave velocity, were neglected. If the source of the synthetic beams is placed deeper or shallower, the duration and appearance of the P-, pP- and sP-pulses changes and residuals increase. Of interest are the retrieved moment rate and moment function, which show a clear double pulse and overshoot, respectively (Figure 5.5c). Such an overshoot is not expected for the rupture process of tectonic earthquakes, where the moment rate and moment functions of the P-wave are single-sided pulse and monotonically increasing functions, respectively. However, this feature is commonly observed for nuclear explosions. This can be explained by at least a partial collapse of the explosion cavity immediately after the explosion. In this case, the final moment is only 23% of the peak moment in Figure 5.5c. The inversion of long-period waves led to a seismic moment M_0 of 2.33×10^{17} Nm, representing the time after the overshoot. The peak seismic moment is thus estimated in the range of $M_0^{(\mathrm{peak})} \approx 1.02\times10^{18}$ Nm. The associated low- and high-frequency moment magnitudes (M_W) are M_W=5.55 and $M_W^{(\mathrm{peak})}$=5.97, respectively, and can explain the large difference between the long period M_W and the estimated high-frequency m_b of 6.2 which emerged during the magnitude estimation described in Gaebler et al. (2019).

5.3.3 Implications of the explosion source characterization

The full waveform moment tensor inversion of the 2017 North Korean nuclear test indicates a centroid depth within the range of about 2 km but has a relatively poor resolution because of the long wavelength of low-pass-filtered data. The depth phase modelling of the P waveform was performed at 2.5 Hz and found a centroid depth between 400 and 800 m. According to the crustal profile at the source side, the expected P-wave wavelength is ∼1000 m, which indicates that the source depth is still resolved. This is the best absolute centroid depth estimate possible from seismological data far from the source. Depth estimations in this study are comparable to results from Wang et al. (2018). The authors used numerical models to minimize the misfit between predicted and observed surface displacements and specified a depth of 450 ± 100 m.

The explosive character of the 2017 event is confirmed by moment tensor inversion analysis, which indicates a dominant isotropic source part of around 60%. These results are supported by studies by Liu et al. (2018) and Han et al. (2017), who also revealed a dominant positive isotropic source part. Resolved moment rate and moment functions for the nuclear test using our inversion technique show a clear double-pulse and overshoot, respectively. This suggests a partial collapse of the explosion cavity or might hint at some kind of break-in process immediately after the explosion test. This finding is supported by a large aftershock of local magnitude m_L 4.1 detected following the nuclear test, around 8 min later. According to Liu et al. (2018), the aftershock can qualitatively be interpreted as a rapid destruction of an explosion-generated cracked rock chimney due to cavity collapse.

5.4 Summary and conclusion

Here we have introduced and implemented a methodology that can be applied for automatically and rapidly estimating the STF and hypocentre depth of seismic events by using direct waveform fitting. We applied the method to determine an abnormal seismic event, the 2017 North Korean nuclear test, using high-frequency beam waveforms calculated at several small-aperture, short period seismic arrays and a database of precomputed Green's function. Using our inversion method, we are able to resolve simultaneously the complex STF and the hypocentre depth of the nuclear explosion test. The obtained seismic moment rate function shows a clear double pulse leading to the conclusion that at least a partial cavity collapse formed in the vicinity of the nuclear test immediately after the explosion. Moreover, the depth-phase modelling locates the event within the test site at a depth of approximately 600 m below the surface. These findings are supported by and comparable to the results from other studies.

While we performed a moment tensor inversion before the STF inversion and depth determination in this study, focal mechanism solutions from the first step could always be taken from existing catalogues, previous studies, or various agencies. Once the STF inversion is performed, seismic source properties such as radiated energy and stress drop could be rapidly obtained. This indicates that the method certainly has the potential to be performed in near real-time analysis with satisfactory results.

The parametrisation of the STF using orthogonal basis functions offers advantages over routine estimation of seismic source parameters in near real-time. Standard moment tensor inversion procedure has the limitation of the *a priori* choice of STF, such as triangular or half-sinusoid STFs. The formulation presented here allows recasting the problem as an iterative inversion. In this case the misfit function to be minimised would be a function of both basis function weights and the elements of the moment tensor. The minimisation can then be performed with a two-step iterative procedure (Frohlich, 1979), where in the first step the STF is assumed to be known *a priori* and the problem is solved for the elements of the moment tensor, and then in the second step the moment tensor is held fixed and the objective function is minimised with respect to the basis function weights. These steps can be repeated until they converge to a set of stable solutions. As an efficient regularisation and smoothing has been introduced, the developed method can be applied to estimate unusual long STFs, as for instance expected during landslide events or from seismic events accompanying volcanic caldera collapses. Furthermore, the STF parametrisation introduced here allows to set up the inversion procedure for multiple STFs to obtain the source time histories of the moment tensor terms. In other words, the results would be multiple time series imaging the temporal evolution of the seismic moment tensor components. Such results can be interpreted in the context of improved experimental and numerical modelling under realistic physical conditions.

It should be noted that in our inversion technique, we intrinsically impose that the STF is absolute, meaning that the STF is the same at all stations. This is not a serious concern for moderate to large events (up to $M_W \sim 7.0$–7.5) because directivity effects, which cause changes in the STF at each station, are generally weak. However, for larger events, these effects increase and using a unique STF for all stations becomes a poor approximation. Our future work will focus on modifications of the method to incorporate source complexities and taking into account the directivity effects applied to large earthquakes.

Chapter 6

Summary and outlook

This research is a contribution to improve routine analysis of seismic sources by combining different advanced seismological methods. Specifically, the focus of this work is towards robust estimation of the hypocentre location and temporal evolution of seismic sources based on teleseismic and regional recordings, and developing stable and reliable methods that have the potential for implementing in routine and ultimately in near real-time processing.

The first contribution of this dissertation is to provide a method for large-scale multiple event location (by consideration of several events simultaneously) that applies deterministic travel-time path corrections which compensate for inadequacies in the assumed 1-D velocity model. It is also employs a non-linear, global search location technique. This relocation techniques has been applied to multiple events in complex tectonic environments, such as subduction zones and plate boundary regions. Relocation results for multiple seismic events using station correction terms demonstrate that the method provides substantial reduction in travel-time residuals, both at regional and teleseismic stations. In general, the relocation procedure results in sharpening seismicity features associated with tectonic environments, e.g. the pattern of Wadati-Benioff zones or of seismicity lineaments along fault zones. Moreover, substantial improvement of focal depths is one of the highlights of the relocation results, demonstrating how effectively this method can handle the model errors associated with regional structures such as subducting slabs, which otherwise can severely bias depth estimation.

To meet the computational demands of this location problem, a new software package has been developed in the scope of this thesis to efficiently relocate large sets of seismic events. The tool allows to relocate seismicity in local, regional, and global scales. The updated code and extensive documentation are freely available for both scientific and applied purposes, and it might serve as user-friendly tool broadening the use of relative relocation technique. A strong motivation for designing the tool has been to provide a simple and flexible environment that shields the user from the complexities of programming and can be used by not only seismologists but also other research geoscientists. The two demonstrated applications to the Arctic plate boundary (regional and teleseismic) and Iberia, Portugal (local) were motivated by requests from external scientists.

One of the goals of earthquake relocation studies is to integrate the relocation algorithms to near real-time processing to locate new events with the accuracy of the relocated reference catalogue. For this aim the potential of the new relocation algorithm to be integrated to near real-time processing has been investigated through a realistic simulation. The locations of a set of back-testing ground-truth events represent a considerable improvement over the corresponding routine locations. The increase of the percentage reduction in epicentre error when more arrival times are available is one important obtained result and is a promising result for global seismic monitoring and near real-time processing. Moreover, the relocation

results revealed that, in the absence of teleseismic observations, the epicentre error continues to decrease with increasing number of regional arrivals. This is a strong support for the conclusion that our relocation process can be used to locate smaller magnitude events, that are recorded regionally, with higher accuracy, or where fast location based on regional stations is needed. As the (near) real-time method has been developed in cooperation with the scientists from the GEOFON processing team, it is suited for a potential implementation in the routine processing flow in the GEOFON project.

Finally, a flexible and reasonably efficient inversion technique has been developed to retrieve the seismic source time function; a source parameter that is particularly useful in seismic monitoring to detect destructive tsunami earthquakes and nuclear explosions, and have the potential to be provided in near real-time. The parametrisation of the source time function using orthogonal basis functions allows to resolve the complexities of the underlying source time function with satisfactory resolution. The recast inverse problem offers advantages over routine estimation of seismic source parameters in near real-time and allows for inversion of seismic moment tensor, source time function, and hypocentre depth simultaneously. An application example of the inversion method in this dissertation concerns North Korea's sixth underground nuclear test conducted on 3 September 2017. In this case study, the retrieved source time function shows a clear double pulse leading to the conclusion that at least a partial cavity collapse formed in the vicinity of the nuclear test immediately after the explosion. Moreover, the depth-phase modelling locates the event within the test site at a depth of approximately 600 m below the surface.

The presented work and application case studies in this dissertation represent the first step in an effort to establish a framework for automatic, routine generation of reliable catalogues of seismic event locations and source time functions. It was a satisfactory experience to see that it is possible to find solutions and to create valuable new tools to handle each encountered link in this elaborate chain of challenges.

Future work: As with any scientific achievement, there is a lot of room for improvements. Our relocation technique at this point represents our best estimates based on phase pick data alone. Further improvements are possible by extending the relocation method and using differential times obtained via waveform cross correlation to achieve high precision earthquake locations. Additionally, the algorithm can be applied to larger catalogues of events and updating the catalogues on a rolling basis in the future as more data become available.

Since our relocation procedure is based on a global-search location method, it could be implemented for a global 3-D tomography model to achieve further improvement in absolute location accuracy. Despite advances in ray tracing methods and computer hardware, calculation of travel times through a 3-D model is computationally expensive, can take 0.1 to 1.0 s, depending on complications due to ray multipathing. Real time monitoring systems require computational times on the order of a millisecond or faster. A promising approach is to use deep neural networks technique to emulate seismic-phase travel time calculation through 3-D models. In this context, my future goal is to establish a computationally efficient way to implement 3-D velocity models in (near) real-time monitoring systems and enable routine utilization of 3-D models in basic research.

In our source time function inversion technique, I intrinsically impose that the source time function is absolute, meaning that it is the same at all stations. This is not a serious concern for moderate to large events (up to $M_W \sim 7.0$–7.5) because directivity effects, which cause changes in the source time function at each station, are generally weak. However, for

larger events, these effects increase and using a unique source time function for all stations becomes a poor approximation. My future work will focus on modifications of the method to incorporate source complexities and taking into account the directivity effects applied to large earthquakes.

Bibliography

Adam, N., Parizzi, A., Eineder, M., and Crosetto, M. (2009). Practical persistent scatterer processing validation in the course of the Terrafirma project. *Journal of Applied Geophysics*, 69(1):59 – 65. Advances in SAR Interferometry from the 2007 Fringe Workshop.

Aki, K. (1967). Scaling law of seismic spectrum. *Journal of Geophysical Research*, 72(4):1217–1231.

Aki, K. (1972). Scaling Law of Earthquake Source Time-Function. *Geophysical Journal International*, 31(1-3):3–25.

Antolik, M., Ekström, G., and Dziewonski, A. (2001). Global event location with full and sparse data sets using three-dimensional models of mantle P-wave velocity. *Pure and Applied Geophysics*, 158(1):291–317.

Arnold, L. and Pyne, K. (2001). The first trial — grapple. In *Britain and the H-Bomb*, pages 131–150. Palgrave Macmillan UK, London.

Arroucau, P., Custódio, S., Civiero, C., Dias, N. A., and Silveira, G. (2017). PRISM3D: a preliminary 3D reference seismic model of the crust and upper mantle beneath Iberia. In *EGU General Assembly Conference Abstracts*, volume 19, page 16801.

Assink, J., Averbuch, G., Shani-Kadmiel, S., Smets, P., and Evers, L. (2018). A seismo-acoustic analysis of the 2017 North Korean nuclear test. *Seismological Research Letters*.

Assink, J. D., Averbuch, G., Smets, P. S. M., and Evers, L. G. (2016). On the infrasound detected from the 2013 and 2016 DPRK's underground nuclear tests. *Geophysical Research Letters*, 43(7):3526–3533.

Aster, R., Borchers, B., and Thurber, C. (2013). *Parameter Estimation and Inverse Problems*. Elsevier, 2nd edition.

Barth, A. (2014). Significant release of shear energy of the North Korean nuclear test on February 12, 2013. *Journal of Seismology*, 18(3):605–615.

Bassin, C., Laske, G., and Masters, G. (2000). The current limits of resolution for surface wave tomography in North America. *Eos*, 81.

Beck, S., Rietbrock, A., Tilmann, F., Barrientos, S., Meltzer, A., Oncken, O., Bataille, K., Roecker, S., Vilotte, J.-P., and Russo, R. M. (2014). Advancing subduction zone science after a big quake. *Eos, Transactions American Geophysical Union*, 95(23):193–194.

Becker, A., Wotawa, G., De Geer, L.-E., Seibert, P., Draxler, R. R., Sloan, C., D'Amours, R., Hort, M., Glaab, H., Heinrich, P., Grillon, Y., Shershakov, V., Katayama, K., Zhang, Y., Stewart, P., Hirtl, M., Jean, M., and Chen, P. (2007). Global backtracking of anthropogenic radionuclides by means of a receptor oriented ensemble dispersion modelling system in support of Nuclear-Test-Ban Treaty verification. *Atmospheric Environment*, 41:4520–4534.

Belge, M., Kilmer, M. E., and Miller, E. L. (2002). Efficient determination of multiple regularization parameters in a generalized L-curve framework. *Inverse Problems*, 18(4):1161–1183.

Bilham, R. (2013). Societal and observational problems in earthquake risk assessments and their delivery to those most at risk. *Tectonophysics*, 584:166–173.

Billings, S. D., Sambridge, M. S., and Kennett, B. L. N. (1994). Errors in hypocenter location: Picking, model, and magnitude dependence. *Bulletin of the Seismological Society of America*, 84(6):1978–1990.

Bondár, I. and McLaughlin, K. (2009). Seismic location bias and uncertainty in the presence of correlated and non-Gaussian travel-time errors. *Bulletin of the Seismological Society of America*, 99(1):172–193. doi:10.1785/0120080922.

Bondár, I., Myers, S. C., Engdahl, E. R., and Bergman, E. A. (2004). Epicentre accuracy based on seismic network criteria. *Geophysical Journal International*, 156(3):483–496.

Bormann, P. (2012). *New Manual of Seismological Observatory Practice (NMSOP-2)*. Deutsches GeoForschungszentrum GFZ ; IASPEI, Potsdam.

Boucher, G., Ryall, A., and Jones, A. E. (1969). Earthquakes associated with underground nuclear explosions. *Journal of Geophysical Research*, 74(15):3808–3820.

Bowers, D., Marshall, P. D., and Douglas, A. (2001). The level of deterrence provided by data from the SPITS seismometer array to possible violations of the Comprehensive Test Ban in the Novaya Zemlya region. *Geophysical Journal International*, 146(2):425–438.

Cansi, Y. (1995). An automatic seismic event processing for detection and location: The P.M.C.C. Method. *Geophysical Research Letters*, 22(9):1021–1024.

Cesca, S. and Heimann, S. (2017). Challenges in regional moment tensor resolution and interpretation. In D'Amico, S., editor, *Moment Tensor Solutions - A Useful Tool for Seismotectonics*. Springer Natural Hazards.

Cesca, S., Heimann, S., Kriegerowski, M., Saul, J., and Dahm, T. (2017). Moment Tensor Inversion for Nuclear Explosions: What Can We Learn from the 6 January and 9 September 2016 Nuclear Tests, North Korea? *Seismological Research Letters*, 88(2A):300.

Cesca, S., Rohr, A., and Dahm, T. (2013). Discrimination of induced seismicity by full moment tensor inversion and decomposition. *Journal of Seismology*, 17(1):147–163.

Che, I.-Y., Park, J., Kim, I., Kim, T. S., and Lee, H.-I. (2014). Infrasound signals from the underground nuclear explosions of North Korea. *Geophysical Journal International*, 198(1):495–503.

Chen, Q.-f. and Willemann, R. J. (2001). Global test of seismic event locations using three-dimensional earth models. *Bulletin of the Seismological Society of America*, 91(6):1704–1716.

Chen, W. P. and Brudzinski, M. R. (2001). Evidence for a large-scale remnant of subducted lithosphere beneath Fiji. *Science*, 292:2475–2479.

CNN (2018). North Korea blows up tunnels at Punggye-ri nuclear test site. https://edition.cnn.com/2018/05/24/asia/north-korea-nuclear-test-site-intl/index.html.

Coblentz, D. and Pabian, F. (2015). Revised Geologic Site Characterization of the North Korean Test Site at Punggye-ri. *Science & Global Security*, 23(2):101–120.

Crotwell, H. P., Owens, T. J., and Ritsema, J. (1999). The TauP Toolkit: Flexible seismic travel-time and ray-path utilities. *Seismological Research Letters*, 70(2):154.

CTBTO (2018). Preparatory Commission for the Comprehensive Nuclear-Test-Ban Treaty Organization. https://www.ctbto.org/.

Dahm, T. and Krüger, F. (2014). Moment tensor inversion and moment tensor interpretation. In Bormann, P., editor, *New Manual of Seismological Observatory Practice (NMSOP-2), IASPEI, GFZ German Research Centre for Geosciences, Potsdam; http://nmsop.gfz-potsdam.de*. Deutsches GeoForschungsZentrum GFZ, Potsdam, Germany.

Dahm, T., Küger, F., Stammler, K., Klinge, K., Kind, R., Wylegalla, K., and Grasso, J.-R. (2007). The 2004 Mw 4.4 Rotenburg, Northern Germany, Earthquake and Its Possible Relationship with Gas Recovery. *Bulletin of the Seismological Society of America*, 97(3):691.

Douglas, A. (1967). Complex morphology of subducted lithosphere in the mantle beneath the Tonga trench. *Nature*, 215:47–48.

Drob, D. P., Picone, J. M., and Garcés, M. (2003). Global morphology of infrasound propagation. *Journal of Geophysical Research*, 108(D21):13–1–13–12. 4680.

Dziewonski, A. M. and Anderson, D. L. (1981). Preliminary reference Earth model. *Physics of the Earth and Planetary Interiors*, 25(4):297 – 356.

Engdahl, E. R., van der Hilst, R., and Buland, R. (1998). Global teleseismic earthquake relocation with improved travel times and procedures for depth determination. *Bulletin of the Seismological Society of America*, 88(3):722.

Evernden, J. F. (1969). Identification of earthquakes and explosions by use of teleseismic data. *Journal of Geophysical Research*, 74(15):3828–3856.

Evers, L. G. and Haak, H. W. (2007). Infrasonic forerunners: Exceptionally fast acoustic phases. *Geophysical Research Letters*, 34(10). L10806.

Font, Y., Kao, H., Lallemand, S., Liu, C.-S., and Chiao, L.-Y. (2004). Hypocentre determination offshore of eastern Taiwan using the Maximum Intersection method. *Geophysical Journal International*, 158(2):655–675.

Ford, S. R., Dreger, D. S., and Walter, W. R. (2010). Network sensitivity solutions for regional moment-tensor inversions. *Bulletin of the Seismological Society of America*, 100(5A):1962.

Frohlich, C. (1979). An efficient method for joint hypocenter determination for large groups of earthquakes. *Computers and Geosciences*, 5(3-4):387–389.

Gaebler, P., Ceranna, L., Nooshiri, N., Barth, A., Cesca, S., Frei, M., Grünberg, I., Hartmann, G., Koch, K., Pilger, C., Ross, J. O., and Dahm, T. (2019). A multi-technology analysis of the 2017 North Korean nuclear test. *Solid Earth*, 10(1):59–78.

Gaebler, P. J. and Ceranna, L. (2017). The seismic network of the International Monitoring System (IMS). In Pilger, C., Ceranna, L., and Bönnemann, C., editors, *Monitoring Compliance with the Comprehensive Nuclear-Test-Ban Treaty (CTBT). Contributions by the German National Data Center*, pages 69–90. Schweizerbart Science Publishers, Stuttgart, Germany.

Gatelli, F., Monti Guamieri, A., Parizzi, F., Pasquali, P., Prati, C., and Rocca, F. (1994). The wavenumber shift in SAR interferometry. *IEEE Transactions on Geoscience and Remote Sensing*, 29(4):855 – 865.

Geiger, L. (1921). Probability method for the determination of earthquake epicenters from the arrival time only. *Bulletin of Saint Louis University*, 8:60–71.

GEOFON Data Centre (1993). GEOFON seismic network. Deutsches GeoForschungsZentrum GFZ.

GFZ and CNRS-INSU (2006). IPOC seismic network. Integrated Plate boundary Observatory Chile - IPOC.

Gibbons, S. J., Harris, D. B., Dahl-Jensen, T., Kværna, T., Larsen, T. B., Paulsen, B., and Voss, P. H. (2017a). Locating seismicity on the Arctic plate boundary using multiple-event techniques and empirical signal processing. *Geophysical Journal International*, 211(3):1613–1627.

Gibbons, S. J., Pabian, F., Näsholm, S. P., Kværna, T., and Mykkeltveit, S. (2017b). Accurate relative location estimates for the North Korean nuclear tests using empirical slowness corrections. *Geophysical Journal International*, 208:101–117.

Glasstone, S. and Dolan, P. J. (1977). *The Effects of Nuclear Weapons*. U.S. Government Printing Office.

Gleyzes, M. A., Perret, L., and Kubik, P. (2012). Pleiades System Architecture and Main Performances. *ISPRS - International Archives of the Photogrammetry, Remote Sensing and Spatial Information Sciences*, pages 537–542.

Gorbatov, A. and Kennett, B. (2003). Joint bulk-sound and shear tomography for Western Pacific subduction zones. *Earth and Planetary Science Letters*, 210(3–4):527–543.

Got, J.-L., Fréchet, J., and Klein, F. W. (1994). Deep fault plane geometry inferred from multiplet relative relocation beneath the south flank of Kilauea. *Journal of Geophysical Research*, 99(B8):15375–15386.

Got, J. L., Okubo, P., Machenbaum, R., and Tanigawa, W. (2002). A real-time procedure for progressive multiplet relative relocation at the Hawaiian Volcano Observatory. *Bulletin of the Seismological Society of America*, 92(5):2019–2026.

Grigoli, F., Cesca, S., Krieger, L., Kriegerowski, M., Gammaldi, S., Horalek, J., Priolo, E., and Dahm, T. (2016). Automated microseismic event location using Master-Event Waveform Stacking. *Scientific Reports*, 6:25744 EP –. Article.

Gurnis, M., Ritsema, J., Van Heijst, H.-J., and Zhong, S. (2000). Tonga slab deformation: The influence of a lower mantle upwelling on a slab in a young subduction zone. *Geophysical Research Letters*, 27(16):2373–2376.

Gutenberg, B. (1945a). Amplitudes of P, PP, and S and magnitude of shallow earthquakes. *Bulletin of the Seismological Society of America*, 35(2):57.

Gutenberg, B. (1945b). Magnitude determination for deep-focus earthquakes. *Bulletin of the Seismological Society of America*, 35(3):117.

Han, L., Wu, Z., Jiang, C., and Liu, J. (2017). Properties of three seismic events in September 2017 in the northern Korean Peninsula from moment tensor inversion. *Science Bulletin*, 62(23):1569 – 1571.

Hansen, P. (1998). *Rank-Deficient and Discrete Ill-Posed Problems: Numerical Aspects of Linear Inversion*. SIAM, Philadelphia.

Hartmann, G., Barth, A., Ross, J. O., Grünberg, I., and Frei, M. (2017). Verification of the North Korean Nuclear Explosions 2006, 2009, 2013, and 2016. In Pilger et al. (2017), pages 137–165.

Heimann, S., Isken, M., Kühn, D., Sudhaus, H., Steinberg, A., Vasyura-Bathke, H., Daout, S., Cesca, S., and Dahm, T. (2018). Grond - A probabilistic earthquake source inversion framework. GFZ Data Services, http://doi.org/10.5880/GFZ.2.1.2018.003.

Heimann, S., Kriegerowski, M., Isken, M., Cesca, S., Daout, S., Grigoli, F., Juretzek, C., Megies, T., Nooshiri, N., Steinberg, A., Sudhaus, H., Vasyura-Bathke, H., Willey, T., and Dahm, T. (2017). Pyrocko - An open-source seismology toolbox and library. GFZ Data Services, http://doi.org/10.5880/GFZ.2.1.2017.001.

Horn, R. A. and Johnson, C. R. (2012). *Matrix Analysis*. Cambridge University Press, New York, NY, USA, 2nd edition.

Hudson, J. A., Pearce, R. G., and Rogers, R. M. (1989). Source type plot for inversion of the moment tensor. *Journal of Geophysical Research: Solid Earth*, 94(B1):765–774.

Husen, S. and Hardebeck, J. L. (2010). Earthquake location accuracy. *Community Online Resource for Statistical Seismicity Analysis*, 10.

ISC (2019). International Seismological Centre: On-line Bulletin. *International Seismological Centre*, UK. http://www.isc.ac.uk.

Jordan, T. H. and Sverdrup, K. A. (1981). Teleseismic location techniques and their application to earthquake clusters in the south-central pacific. *Bulletin of the Seismological Society of America*, 71(4):1105–1130.

Kalinowski, M., Axelsson, A., Bean, M., Blanchard, X., Bowyer, T., Brachet, G., Hebel, S., McIntyre, J., Peters, J., Pistner, C., Raith, M., Ringbom, A., R. J. Saey, P., Schlosser, C., J. Stocki, T., Taffary, T., and Ungar, K. (2010). Discrimination of nuclear explosions against civilian sources based on atmospheric Xenon isotopic activity ratios. *Pure and Applied Geophysics*, 167:517–539.

Kampes, B. M. (2006). *Radar Interferometry – Persistent Scatterer Technique*. Springer Netherlands.

Kennett, B. L. N. and Engdahl, E. R. (1991). Traveltimes for global earthquake location and phase identification. *Geophysical Journal International*, 105(2):429–465.

Kennett, B. L. N., Engdahl, E. R., and Buland, R. (1995). Constraints on seismic velocities in the earth from traveltimes. *Geophysical Journal International*, 122(1):108–124.

Koch, K. and Pilger, C. (2018). Infrasound observations from the site of past underground nuclear explosions in North Korea. *Geophysical Journal International*, page ggy381.

Korean Meterological Agency (2018). Earthquake catalogue, available at http://www.weather.go.kr/weather/earthquake_volcano/domesticlist.jsp?startTm=2017-09-01&endTm=2018-12-13&startSize=999&endSize=999&startLat=41.2&endLat=41.4&startLon=129&endLon=129.2&lat=&lon=&dist=&keyword=&x=36&y=11.

Kriegerowski, M., Cesca, S., Heimann, S., and Dahm, T. (2016). Abedeto – a tool to constrain event depth by depth phase modelling and visualization. In *35th General Assembly of the European Seismological Commission*, page 553.

Lange, D., Tilmann, F., Barrientos, S. E., Contreras-Reyes, E., Methe, P., Moreno, M., Heit, B., Agurto, H., Bernard, P., Vilotte, J.-P., and Beck, S. (2012). Aftershock seismicity of the 27 February 2010 Mw 8.8 Maule earthquake rupture zone. *Earth and Planetary Science Letters*, 317âĂŞ318:413–425.

Lay, T. and Wallace, T. C. (1995). *Modern Global Seismology*. Academic Press, San Diego, California.

Le Pichon, A., Blanc, E., and Hauchecorne, A. (2010). *Infrasound Monitoring for Atmospheric Studies*. Springer.

Lin, G. and Shearer, P. (2006). The COMPLOC earthquake location package. *Seismological Research Letters*, 77(4):440–444.

Lin, G. and Shearer, P. M. (2005). Tests of relative earthquake location techniques using synthetic data. *Journal of Geophysical Research*, 110(B4). B04304.

Lin, G., Shearer, P. M., and Hauksson, E. (2007). Applying a three-dimensional velocity model, waveform cross correlation, and cluster analysis to locate southern California seismicity from 1981 to 2005. *Journal of Geophysical Research*, 112(B12). B12309.

Lippitsch, R., White, R. S., and Soosalu, H. (2005). Precise hypocentre relocation of microearthquakes in a high-temperature geothermal field: the TorfajÃűkull central volcano, Iceland. *Geophysical Journal International*, 160(1):371–388.

Liu, J., Li, L., Zahradník, J., Sokos, E., Liu, C., and Tian, X. (2018). North Korea's 2017 test and its nontectonic aftershock. *Geophysical Research Letters*, 45(7):3017–3025.

Lomax, A. (2005). A reanalysis of the hypocentral location and related observations for the great 1906 California earthquake. *Bulletin of the Seismological Society of America*, 95(3):861–877.

Lomax, A. (2019). The NonLinLoc software guide. http://alomax.free.fr/nlloc/index.html. last accessed January 2019.

Lomax, A. and Curtis, A. (2001). Fast, probabilistic earthquake location in 3d models using oct-tree importance sampling. *Geophysical Research Abstracts*, 3:955.

Lomax, A., Michelini, A., and Curtis, A. (2009). Earthquake location, direct, global-search methods. In Meyers, R. A., editor, *Encyclopedia of Complexity and Systems Science*, pages 1–33. Springer New York.

Lomax, A., Virieux, J., Volant, P., and Berge-Thierry, C. (2000). Probabilistic earthquake location in 3-D and layered models. In Thurber, C. H. and Rabinowitz, N., editors, *Advances in Seismic Event Location*, volume 18 of *Modern Approaches in Geophysics*, pages 101–134. Springer Netherlands.

Madariaga, R. (2007). Seismic source theory. In Schubert, G., editor, *Treatise on Geophysics*, volume 4, chapter 4.02, pages 59–82. Elsevier, Amsterdam.

Massonnet, D., Rossi, M., Carmona, C., Adragna, F., Peltzer, G., Feigl, K., and Rabaute, T. (1993). The displacement field of the Landers earthquake mapped by radar interferometry. *Nature*, 364:138–142.

Matos, C., Custódio, S., Batlló, J., Zahradník, J., Arroucau, P., Silveira, G., and Heimann, S. (2018). An active seismic zone in intraplate west Iberia inferred from high-resolution geophysical data. *Journal of Geophysical Research: Solid Earth*, 123(4):2885–2907.

Matoza, R. S., Shearer, P. M., Lin, G., Wolfe, C. J., and Okubo, P. G. (2013). Systematic relocation of seismicity on Hawaii Island from 1992 to 2009 using waveform cross correlation and cluster analysis. *Journal of Geophysical Research*, 118(5):2275–2288.

Matzel, E., Simmons, N. A., and Myers, S. (2014). *LLNL-Earth3D User Manual*. Lawrence Livermore National Laboratory. https://www-gs.llnl.gov/content/assets/docs/LLNL-Earth3D_User_Manual_032814.pdf.

Murphy, J. R. (1981). P Wave Coupling of Underground Explosions in Various Geologic Media. In Husebye, E. S. and Mykkeltveit, S., editors, *Identification of Seismic Sources — Earthquake or Underground Explosion*, pages 1201–205. Springer Netherlands, Dordrecht.

Mutschlecner, J. P. and Whitaker, R. W. (2005). Infrasound from earthquakes. *Journal of Geophysical Research: Atmospheres*, 110(D1).

Myers, S. C., Johannesson, G., and Hanley, W. (2007). A Bayesian hierarchical method for multiple-event seismic location. *Geophysical Journal International*, 171(3):1049–1063.

Myers, S. C. and Schultz, C. A. (2000). Improving sparse network seismic location with Bayesian kriging and teleseismically constrained calibration events. *Bulletin of the Seismological Society of America*, 90(1):199–211.

Myers, S. C., Simmons, N. A., Johannesson, G., and Matzel, E. (2015). Improved regional and teleseismic P-wave travel-time prediction and event location using a global 3D velocity model. *Bulletin of the Seismological Society of America*, 105(3):1642–1660.

Mykkeltveit, S. and Ringdal, F. (1981). Phase identification and event location at regional distance using small-aperture array data. In Husebye, E. S. and Mykkeltveit, S., editors, *Identification of Seismic Sources — Earthquake or Underground Explosion*, pages 467–481, Dordrecht. Springer Netherlands.

Nichols, J. M. and Beavers, J. E. (2008). World earthquake fatalities from the past: Implications for the present and future. *Natural Hazards Review*, 9(4):179–189.

Nooshiri, N., Saul, J., Heimann, S., Tilmann, F., and Dahm, T. (2017). Revision of earthquake hypocentre locations in global bulletin data sets using source-specific station terms. *Geophysical Journal International*, 208(2):589–602.

Nuclear Safety and Security Commission (2017). Press Release: Radionuclide Detection After the 6th North Korea Nuclear Test. http://www.nssc.go.kr/_custom/nssc/_common/board/download.jsp?attach_no=20247.

Pabian, F. and Coblentz, D. (2017). Surface Disturbances at the Punggye-ri Nuclear Test Site: Another Indicator of Nuclear Testings? *Los Alamos National Laboratory. Report posted on 38north.org, final version issued March 15, 2017.*

Park, J., Che, I.-Y., Stump, B., Hayward, C., Dannemann, F., Jeong, S., Kwong, K., McComas, S., Oldham, H. R., Scales, M. M., and Wright, V. (2018). Characteristics of infrasound signals from North Korean underground nuclear explosions on 2016 January 6 and September 9. *Geophysical Journal International*, 214(3):1865–1885.

Pavlis, G. L. (1986). Appraising earthquake hypocenter location errors: A complete, practical approach for single-event locations. *Bulletin of the Seismological Society of America*, 76(6):1699–1717.

Pavlis, G. L. and Booker, J. R. (1983). Progressive multiple event location (PMEL). *Bulletin of the Seismological Society of America*, 73(6A):1753–1777.

Pilger, C., Ceranna, L., and Bönnemann, C., editors (2017). *Monitoring Compliance with the Comprehensive Nuclear-Test-Ban Treaty (CTBT). Contributions by the German National Data Center*. Schweizerbart Science Publishers, Stuttgart, Germany.

Poupinet, G., Ellsworth, W. L., and Frechet, J. (1984). Monitoring velocity variations in the crust using earthquake doublets: An application to the Calaveras Fault, California. *Journal of Geophysical Research*, 89(B7):5719–5731.

Pysklywec, R., Mitrovica, J., and Ishii, M. (2003). Mantle avalanche as a driving force for tectonic reorganization in the southwest pacific. *Earth and Planetary Science Letters*, 209(1):29 – 38.

Richards-Dinger, K. B. and Shearer, P. M. (2000). Earthquake locations in southern California obtained using source-specific station terms. *Journal of Geophysical Research*, 105(B5):10939–10960.

Ringbom, A., Axelsson, A., Aldener, M., Auer, M., Bowyer, T., Fritioff, T., Hoffman, I., Khrustalev, K., Nikkinen, M., Popov, V., Popov, Y., Ungar, K., and Wotawa, G. (2014). Radioxenon detections in the CTBT international monitoring system likely related to the announced nuclear test in North Korea on February 12, 2013. *Journal of Environmental Radioactivity*, 128:47 – 63.

Ringdal, F., Marshall, P. D., and Alewine, R. W. (1992). Seismic yield determination of Soviet underground nuclear explosions at the Shagan River test site. *Geophysical Journal International*, 109(1):65–77.

Rodi, W. L. and Myers, S. C. (2013). Computation of traveltime covariances based on stochastic models of velocity heterogeneity. *Geophysical Journal International*, 194(3):1582–1595. doi:10.1093/gji/ggt171.

Ross, J. O., Bollhöfer, A., and Schlosser, C. (2017). The IMS radionuclide network supported by Atmospheric Transport Modelling (ATM). In Pilger, C., Ceranna, L., and Bönnemann, C., editors, *Monitoring Compliance with the Comprehensive Nuclear-Test-Ban Treaty (CTBT). Contributions by the German National Data Center*, pages 123–136. Schweizerbart Science Publishers, Stuttgart, Germany.

Schorlemmer, D., Euchner, F., Kästli, P., and Saul, J. (2011). QuakeML: status of the XML-based seismological data exchange format. *Annals of Geophysics*, 54(1):59–65.

Schultz, C. A., Myers, S. C., Hipp, J., and Young, C. J. (1998). Nonstationary Bayesian kriging: A predictive technique to generate spatial corrections for seismic detection, location, and identification. *Bulletin of the Seismological Society of America*, 88(5):1275–1288.

Schurr, B., Asch, G., Hainzl, S., Bedford, J., Hoechner, A., Palo, M., Wang, R., Moreno, M., Bartsch, M., Zhang, Y., Oncken, O., Tilmann, F., Dahm, T., Victor, P., Barrientos, S., and Vilotte, J.-P. (2014). Gradual unlocking of plate boundary controlled initiation of the 2014 Iquique earthquake. *Nature*, 512(7514):299–302.

Sen, M. K. and Roy, I. G. (2003). Computation of differential seismograms and iteration adaptive regularization in prestack waveform inversion. *Geophysics*, 68(6):2026–2039.

Shearer, P., Hauksson, E., and Lin, G. (2005). Southern California hypocenter relocation with waveform cross-correlation, part 2: Results using source-specific station terms and cluster analysis. *Bulletin of the Seismological Society of America*, 95(3):904–915.

Shearer, P. M. (2002). Parallel fault strands at 9-km depth resolved on the Imperial Fault, Southern California. *Geophysical Research Letters*, 29(14). doi:10.1029/2002GL015302.

Simmons, N. A., Myers, S. C., Johannesson, G., and Matzel, E. (2012). LLNL-G3Dv3: Global P wave tomography model for improved regional and teleseismic travel time prediction. *Journal of Geophysical Research*, 117(B10). B10302.

Simmons, N. A., Myers, S. C., Johannesson, G., Matzel, E., and Grand, S. P. (2015). Evidence for long-lived subduction of an ancient tectonic plate beneath the southern Indian Ocean. *Geophysical Research Letters*, 42(21):9270–9278.

Smith, G. P. and Ekström, G. (1996). Improving teleseismic event locations using a three-dimensional Earth model. *Bulletin of the Seismological Society of America*, 86(3):788–796.

Snoke, J. A. (2009). Traveltime tables for iasp91 and ak135. *Seismological Research Letters*, 80(2):260.

Stein, A. F., Draxler, R. R., Rolph, G. D., Stunder, B. J. B., Cohen, M. D., and Ngan, F. (2015). NOAAâĂŹs HYSPLIT Atmospheric Transport and Dispersion Modeling System. *Bulletin of the American Meteorological Society*, 96(12):2059–2077.

Storchak, D. A., Schweitzer, J., and Bormann, P. (2003). The IASPEI standard seismic phase list. *Seismological Research Letters*, 74(6):761.

Suzuki, S., Osawa, Y., Hatooka, Y., Kankaku, Y., and Watanabe, T. (2009). Overview of Japan's Advanced Land Observing Satellite-2 mission. In Roland Meynart, Steven P. Neeck, H. S., editor, *Sensors, Systems, and Next-Generation Satellites XIII*, volume 7474.

Tarantola, A. and Valette, B. (1982). Inverse problems = quest for information. *Journal of Geophysics*, 50:159–170.

Tessmer, E., Kosloff, D., and Behle, A. (1992). Elastic wave propagation simulation in the presence of surface topography. *Geophysical Journal International*, 108(2):621–632.

Thurber, C. and Eberhart-Phillips, D. (1999). Local earthquake tomography with flexible gridding. *Computers and Geosciences*, 25(7):809 – 818.

Thurber, C. H. (1992). Hypocenter-velocity structure coupling in local earthquake tomography. *Physics of the Earth and Planetary Interiors*, 75(1):55 – 62.

Tocheport, A., Rivera, L., and Chevrot, S. (2007). A systematic study of source time functions and moment tensors of intermediate and deep earthquakes. *Journal of Geophysical Research: Solid Earth*, 112(B7).

Trugman, D. T. and Shearer, P. M. (2017). GrowClust: A hierarchical clustering algorithm for relative earthquake relocation, with application to the Spanish Springs and Sheldon, Nevada, earthquake sequences. *Seismological Research Letters*, 88(2A):379.

Vallée, M. (2013). Source time function properties indicate a strain drop independent of earthquake depth and magnitude. *Nature communications*, 4:2606.

van der Hilst, R. D. (1995). Complex morphology of subducted lithosphere in the mantle beneath the Tonga trench. *Nature*, 374:154–157.

van Wijk, K., Scales, J. A., Navidi, W., and Tenorio, L. (2002). Data and model uncertainty estimation for linear inversion. *Geophysical Journal International*, 149(3):625–632.

Vassiliou, M. and Kanamori, H. (1982). The energy release in earthquakes. *Bulletin of the Seismological Society of America*, 72(2):371–387.

Vavryčuk, V. and Kim, S. G. (2014). Nonisotropic radiation of the 2013 North Korean nuclear explosion. *Geophysical Research Letters*, 41(20):7048–7056.

Wahba, G. (1990). *Spline Models for Observational Data*. Society for Industrial and Applied Mathematics.

Waldhauser, F. (2009). Near-real-time double-difference event location using long-term seismic archives, with application to northern California. *Bulletin of the Seismological Society of America*, 99(5):2736–2748.

Waldhauser, F. and Ellsworth, W. L. (2000). A double-difference earthquake location algorithm: Method and application to the northern Hayward fault, California. *Bulletin of the Seismological Society of America*, 90(6):1353–1368.

Wang, R. (1999). A simple orthonormalization method for stable and efficient computation of Green's functions. *Bulletin of the Seismological Society of America*, 89(3):733.

Wang, T., Shi, Q., Nikkhoo, M., Wei, S., Barbot, S., Dreger, D., Bürgmann, R., Motagh, M., and Chen, Q.-F. (2018). The rise, collapse, and compaction of Mt. Mantap from the 3 September 2017 North Korean nuclear test. *Science*.

Wei, M. (2017). Location and source characteristics of the 2016 January 6 North Korean nuclear test constrained by InSAR. *Geophysical Journal International*, 209(2):762–769.

Weston, J., Engdahl, E. R., Harris, J., Di Giacomo, D., and Storchak, D. A. (2018). ISC-EHB: reconstruction of a robust earthquake data set. *Geophysical Journal International*, 214(1):474–484. doi:10.1093/gji/ggy155.

Zhang, M. and Wen, L. (2013). High-precision location and yield of North Korea's 2013 nuclear test. *Geophysical Research Letters*, 40(12):2941–2946.

Zhao, L., Xie, X., Wang, W., and Yao, Z. (2014). The 12 February 2013 North Korean Underground Nuclear Test. *Seismological Research Letters*, 85(1):130–134.

Zhao, L.-F., Xie, X.-B., Wang, W.-M., Hao, J.-L., and Yao, Z.-X. (2016). Seismological investigation of the 2016 january 6 north korean underground nuclear test. *Geophysical Journal International*, 206(3):1487–1491.

Appendix A

SCOTER software package

A.1 Installation and updating

The latest version of SCOTER is freely available to all users at https://gitext.gfz-potsdam.de/nooshiri/scoter. After installing `git`, the SCOTER's source code can be downloaded and installed using:

```
$ cd ~/src/   # or wherever you keep your source packages
$ git clone https://gitext.gfz-potsdam.de/nooshiri/scoter.git
$ cd scoter
$ sudo python setup.py install
```

When SCOTER is installed, its dependencies are automatically installed except for NonLinLoc program. The original software is developed and maintained by Anthony Lomax (Lomax, 2019). The latest version of NonLinLoc modified and packaged as SCOTER backend can be downloaded and installed by:

```
$ cd ~/src/   # or wherever you keep your source packages
$ git clone https://gitext.gfz-potsdam.de/nooshiri/scoter_NLL.git
$ cd scoter_NLL/src
$ sudo make -R all
```

For updating an existing manual installation of SCOTER, the source code needs to be updated using:

```
$ cd scoter   # change to the directory where SCOTER was cloned
$ git pull origin master
```

and then reinstalled as described above.

A.2 The SCOTER configuration in more detail

A.2.1 The `DatasetConfig` section

`path_prefix`: Defines a prefix which is prepended to all paths in the configuration.

`${event_name}`: Placeholder that is substituted with the event names defined in `events_path` file.

`events_path`: File with the hypocenter information and possibly reference solutions.

`bulletins_template_path`: Template path for the files with phase pick observations.

`stations_paths`: List of the files with station information.

`traveltimes_path`: Directory of the travel-time grid files.

`traveltimes_prefix`: File prefix for the travel-time grid files.

`takeoffangles_template_path`: Template path for the files with pre-computed takeoff angles.

`starting_delays_path`: File(s) with the previously determined station correction terms.

A.2.2 The `StationTermsConfig` section

`StaticConfig` subsection:

`niter`: Number of iterations for static station terms calculation.

`phase_list`: List of direct *P*- and *S*-wave type phases for which static terms are computed.

`nresiduals_min`: Minimum number of residuals required to compute static term for each station.

`SourceSpecificConfig` subsection:

`niter`: Number of iterations for source-specific station terms (SSST) calculation.

`phase_list`: List of direct *P*- and *S*-wave type phases for which SSST values are calculated.

`start_cutoff_dist`, `end_cutoff_dist`: Starting and ending distance cut-off (R_{max}) for the SSST calculation. For intermediate iterations, R_{max} is set to values spaced evenly in logarithmic scale *Unit: m*

`start_nlinks_max`, `end_nlinks_max`: Starting and ending maximum number of nearby events (N) for the SSST calculation. For intermediate iterations, N is set to values spaced evenly in logarithmic scale.

`nlinks_min`: Minimum number of nearby events (i.e. residuals) required to compute SSST values for each source-receiver path.

`ndelays_min`: Minimum number of adjusted picks (i.e. station terms) for an event required to consider it as a neighbouring event in SSST iterations.

`WeightConfig` subsection:

`distance_weighting`: How to weight nearby events located around a target event. This option is valid only for SSST computation. Available choices are `"uniform"`, `"distance"`, `"effective_distance"`. *Default: "uniform"*

`apply_outlier_rejection`: Whether to apply residual outliers rejection. Used to detect large travel-time residuals that should not be included in station terms calculation. *Default: true*

`outlier_rejection_type`: Cut-off threshold type for residual outliers. Available choices are `"static"`, `"dynamic"`. *Default: "dynamic"*

`outlier_rejection_level`: Cut-off threshold level for residual outliers. For "static" cut-off, it is the absolute threshold in seconds. For "dynamic" cut-off, it is a factor to multiply the scaled median absolute deviation (SMAD) of the residuals. *Default:* 6

`LocationQualityConfig` subsection:
Events with low-quality locations (i.e. do not satisfy one or more of the following conditions) are not used in station terms calculation.

`standard_error_max`: Maximum location RMS. *Unit: s*

`secondary_azigap_max`: Maximum secondary azimuthal gap *Unit: deg*

`largest_uncertainty_max`: Maximum semi-major axis of the confidence ellipsoid (corresponding to the largest location uncertainty). *Unit: m*

A.2.3 The `NetworkConfig` section

`station_selection`: Whether to select (filter) station data based on epicentral (surface) distances. The distances are calculated based on the initial locations of the events defined in `events_path` file. *Default: false*

`station_dist_min`, `station_dist_max`: Minimum and maximum source-receiver surface distance. *Unit: deg*; *Default:* 0, 180

A.2.4 The `NLLocConfig` section

`NLLocTrans` subsection:
Geographic transformation parameters.

`trans_type`: Sets geographic to working coordinates transformation parameters. Available choices are `"GLOBAL"` (spherical mode, referred to as *Global*) and `"SIMPLE"`, `"NONE"`, `"SDC"`, `"LAMBERT"` (rectangular mode, referred to as *Non-Global*).

The following three additional parameters need to be included and set if the `trans_type` is one of `"SIMPLE"`, `"SDC"`, `"LAMBERT"` options:

`lat_orig`, `lon_orig`: Latitude (between $-90°$ and $90°$) and longitude (from $-180°$ to $180°$) of the rectangular coordinates origin. *Unit: deg*

`rot_angle`: Rotation angle of geographic north measured clockwise relative to the rectangular coordinates system Y-axis. *Unit: deg*

The following three additional parameters need to be included and set only if the `trans_type` is set to `"LAMBERT"`:

`ref_ellips`: Reference ellipsoid name. Available choices are "WGS-84", "GRS-80", "WGS-72", "Australian", "Krasovsky", "International", "Hayford-1909", "Clarke-1880", "Clarke-1866", "Airy", "Bessel", "Hayford-1830", "Sphere".

`first_paral`, `second_paral`: First and second standard parallels (between $-90°$ and $90°$). *Unit: deg*

`NLLocGrid` subsection:
Describes location search grid.

`x_num`, `y_num`, `z_num`:
Non-Global: Number of grid nodes in the x/y/z directions.
Global: Number of grid nodes in the long./lat./depth directions.

`x_orig`, `y_orig`:
Non-Global: x/y location of the grid origin relative to the geographic origin. *Unit: km*
Global: long./lat. of the south-west corner of the grid. *Unit: deg*

`z_orig`:
Non-Global: z location of the grid origin relative to the geographic origin (positive z-axis points down). *Unit: km*
Global: depth of the south-west corner of the grid (positive z-axis points down). *Unit: km*

`dx`, `dy`:
Non-Global: Grid node spacing along the x-/y-axis. *Unit: km*
Global: Grid node spacing along long./lat. directions. *Unit: deg*

`dz`: Grid node spacing along the z-axis/depth direction. *Unit: km*

`NLLocSearchOcttree` subsection:
Specifies the oct-tree global search parameters.

`init_num_cells_x`, `init_num_cells_y`, `init_num_cells_z`: Initial number of oct-tree cells in the x/y/z or long./lat./depth directions.

`min_node_size`: Smallest oct-tree node side length to process. The oct-tree search is terminated after a node with a side smaller than this length is evaluated. *Unit: km*

`max_num_nodes`: Total number of nodes to process.

`use_sta_density`: Available choices are 0, 1. If 1, weights oct-tree cell probability values used for subdivide decision in proportion to number of stations in oct-tree cell. Gives higher search priority to cells containing stations, stabilises convergence to local events when global search used with dense cluster of local stations. *Default:* 0

`stop_on_what`: Available choices are 0, 1. If 1, the oct-tree search is terminated when first `min_node_size` reached. If 0, the oct-tree search continues until `max_num_nodes` is evaluated, but cell subdivision is only done to `min_node_size`. *Default:* 1

`NLLocMeth` subsection:
Specifies the location algorithm (i.e. how to construct the posterior PDF) and corresponding parameters.

`method`: Likelihood function. Available choices are:
`"GAU_ANALYTIC"`: Least-squares L2 norm (Tarantola and Valette, 1982).
`"EDT"`: Equal Differential Time (EDT) likelihood function (Lomax, 2005).
`"EDT_OT_WT"`: Weights the sum of the EDT probabilities by the variance of origin-time estimates over all pairs of readings. Downweights locations with inconsistent origin-time estimates.

`min_dist_sta_grid`, `max_dist_sta_grid`: Minimum and maximum distance between a station and *the center* of the location search grid. Stations that are not in this distance range will not be used for event location. Use

-1 for no minimum and very large value for no maximum (e.g. 1.0e6). *Unit: km*

`min_num_phases`, `max_num_phases`: Minimum and maximum number of phase picks that must be accepted for event location. Use -1 for no maximum.

`min_num_Sphases`: Minimum number of S phases that must be accepted for event location. Use -1 for no maximum number.

`vp_vs_ratio`: V_p/V_s ration. If > 0.0, only P-wave travel-time grids are read and `vp_vs_ratio` is used to calculate S-wave travel-times. If < 0.0, S-wave travel-time grids are directly used (if available). Cannot be used in Global mode.

`reject_duplicate_arrivals`: Whether to leave out duplicate arrivals (observations having the same station and phase labels). If false, then duplicate arrival times will be used if $\Delta t < 0.5 \times$ `sigma_time`.

`NLLocGau` subsection:

Specifies parameters for theoretical, Gaussian model errors described by the covariance matrix $\mathbf{C_T}$ (Tarantola and Valette, 1982):

$$[\mathbf{C_T}]_{ij} = \sigma_{\mathbf{T}}^2 . \exp\left\{-\frac{1}{2}\frac{D_{ij}^2}{\Delta^2}\right\}, \tag{A.1}$$

where D_{ij} is the distance between the station i and the station j, $\sigma_{\mathbf{T}}$ is some theoretical error for travel time to one station due to model errors, and Δ is the correlation length of errors (the wavelength or the length of lateral heterogeneities of the medium).

`sigma_time`: $\sigma_{\mathbf{T}}$ in Equation A.1. *Unit: s*

`corr_len`: Δ in Equation A.1. *Unit: km*

`NLLocGau2` subsection:

Specifies parameters for travel-time dependent model errors. Sets the travel-time error in proportion to the travel-time, thus giving effectively a station-distance weighting, which was not included in the Equation A.1 by Tarantola and Valette (1982). This gives improvements in hypocenter clustering.

`sigma_tfraction`: Fraction of travel time to use as error (between 0 and 1). Travel-time error is calculated as `sigma_tfraction` $\times T^{calc.}$ where $T^{calc.}$ is the model-predicted travel time.

`sigma_tmin`, `sigma_tmax`: Minimum and maximum acceptable values for travel-time error.

`NLLocPhaseid` subsection:

Specifies the mapping of a set of phase codes (e.g. *PN, PG*) to a standardized phase code (e.g. *P*). Can be present multiple times in the configuration file as members of `phaseid_list` entry.

`std_phase`: Standardized phase code.

`phase_code_list`: List of phase codes that may be present in a observation files and should be mapped to (i.e. considered as) the `std_phase` in the location process.

NLLocElevcorr subsection:

Simple elevation correction using the travel time of a vertical ray from elevation zero to the elevation of the station.

`apply_elevcor`: Whether to apply elevation correction. *Default: false*

`vel_p`: *P*-wave velocity used to calculate the elevation correction for *P*-wave type phases. *Unit: km/s*; *Default:* 5.80

`vel_s`: *S*-wave velocity used to calculate the elevation correction for *S*-wave type phases. *Unit: km/s*; *Default:* 3.46

NLLocStawt subsection:

Station distribution weighting. Helps to correct for irregular station distribution, i.e. a high density of stations in regions such as Europe and North America and few or no stations in regions such as oceans. The relative weight for station i is:

$$W_i = \frac{1}{\sum_j \exp\left\{-\frac{d_{ij}^2}{c^2}\right\}^2}, \tag{A.2}$$

where d_{ij} is the surface distance between the station i and the station j, and c is the cut-off distance.

`apply_stawt`: Whether to apply station distribution weighting. *Default: false*

`cutoff_dist`: c in Equation A.2. If < 0.0, it is automatically set to the mean distance between all pairs of stations. *Unit: deg*; *Default:* -1.0

Appendix B

A multi-technology analysis of the 2017 North Korean nuclear test

Originally published as: Gaebler, P., Ceranna, L., **Nooshiri, N.**, Barth, A., Cesca, S., Frei, M., Grünberg, I., Hartmann, G., Koch, K., Pilger, C., Ross, J. O., and Dahm, T. (2018): A multi-technology analysis of the 2017 North Korean nuclear test. *Solid Earth*, 10(1):59–78. doi:10.5194/se-10-59-2019.

Abstract

On September 3rd 2017 official channels of the Democratic People's Republic of Korea announced the successful test of a thermonuclear device. Only seconds to minutes after the alleged nuclear explosion at the Punggye-ri nuclear test site in the mountainous region in the country's north-east at 03:30:02 (UTC) hundreds of seismic stations distributed all around the globe picked up strong and distinct signals associated with an explosion. Different seismological agencies reported body wave magnitudes of well above 6.0, consequently estimating the explosive yield of the device in the order of hundreds of kilotons TNT equivalent. The 2017 event can therefore be assessed being multiple times larger in energy than the two preceding North Korean events in January and September 2016.

This study provides a multi-technology analysis of the 2017 North Korean event and its aftermath using a wide array of geophysical methods. Seismological investigations locate the event within the test site at a depth of approximately 0.6 km below surface. The radiation and generation of P- and S-wave energy in the source region is significantly influenced by the topography of the Mt. Mantap massif. Inversions for the full moment tensor of the main event reveal a dominant isotropic component accompanied by significant amounts of double couple and compensated linear vector dipole terms, confirming the explosive character of the event. Analysis of the source mechanism of an aftershock that occurred around eight minutes after the test in the direct vicinity suggest a cavity collapse. Measurements at seismic stations of the International Monitoring System result in a body wave magnitude of 6.2, which translates to an yield estimate of around 400 kilotons TNT equivalent. The explosive yield is possibly overestimated, since topography and depth phases both tend to enhance the peak amplitudes of teleseismic P-waves. Interferometric Synthetic-Aperture-Radar analysis using data from the ALOS-2 satellite reveal strong surface deformations in the epicenter region. Additional multi-spectral optical data from the Pleiades satellite show clear landslide activity at the test site. The strong surface deformations generated large acoustic pressure peaks, which were observed as infrasound signals with distinctive waveforms even in distances of 401 km. In the aftermath of the 2017 event atmospheric traces of the fission product ^{133}Xe have been detected at various locations in the wider region. While for ^{133}Xe measurements in September 2017 the Punggye-ri test site is disfavoured as source by

means of atmospheric transport modeling, detections in October 2017 at the International Monitoring System station RN58 in Russia indicate a potential delayed leakage of ^{133}Xe at the test site from the 2017 North Korean nuclear test.

B.1 Introduction

The Comprehensive Nuclear Test-Ban-Treaty (CTBT) and its associated entity, the Preparatory Commission for the CTBT organization (CTBTO), are dedicated to monitoring and banning nuclear explosions worldwide – underground, in water or in the atmosphere. The CTBT was opened for signature in 1996 but will only enter into force after the 44 nuclear technology holders (states listed in the Annex 2 of the CTBT) will have signed and ratified the treaty. At the time of this study eight Annex 2 states have still not ratified the treaty, including North Korea. To detect, locate and characterize nuclear explosions an International Monitoring System (IMS) was established by the CTBTO as part of a verification regime. The IMS features four different approaches for the monitoring of potential nuclear explosions. Three methods (seismology, infrasound and hydro-acoustics) are attributed to waveform technologies and have the purpose of detecting, localizing and identifying suspicious events with an explosive source mechanism. The fourth approach features the monitoring of particulate radionuclide and noble gases in the atmosphere and potentially provides the unambiguous evidence of the nuclear character of an explosion. To assess the connection between radionuclide detections and potential source events atmospheric transport modelling (ATM) is applied. Grouping data from different IMS technologies, that is attributed to the same critical event, is referred to as data fusion. For further information on the CTBT, the IMS, and the German National Data Center the reader is referred to Pilger et al. (2017) or CTBTO (2018).

Since the first known nuclear test, carried out by the Unites States in 1945, more than 2000 confirmed nuclear explosion tests were conducted by China, France, Great Britain, India, North Korea, Pakistan, Russia and the United States. It is generally accepted that all six past explosions in North Korea between 2006 and 2017 have been nuclear underground tests. This study therefore refers to the events in North Korea as nuclear tests, even though definite proof might be missing. North Korea is the only country breaking the de facto moratorium on nuclear tests. For detailed information on the first five North Korean tests see for example Hartmann et al. (2017).

All past North Korean nuclear tests were conducted at the Punggye-ri test site in the vicinity of Mt. Mantap in the north-eastern part of the country. Following the geologic description of the test site area provided by Coblentz and Pabian (2015) and Pabian and Coblentz (2017), Mt. Mantap is made out of two distinct geologic formations. The core of the mountain consists of igneous basement rock of either diorite or granite, while the top is capped by a thin layer of basaltic lava flows. The basement crystalline rock and the top layer of Mt. Mantap are separated by a nearly horizontal sequence of volcanic deposits with a thickness of around 200 m. The origin of these deposits is suspected to be volcanic ash from Mt. Paektu, a volcano located around 100 km north-east. Due to their loose consolidation, the volcanic deposits are softer then the basement rock or the basaltic layer and are therefore more susceptible to erosion. Furthermore, the volcanic layer is more exposed to erosional scars and landslides due to its steeper slope. The erosion of the volcanic layer can cause the overlaying basalt cap to break off at the scarp, which is visible in larger piles below the volcanic layer where the slope of the mountain slightly decreases.

The official channels of North Korea announced the 2017 event as a successful test of a fusion bomb. This would be a major step in the nuclear program of North Korea. From

a scientific point, therefore, the depth of the event, its strength in terms of radiated high- and low-frequency seismic energy, the contribution of possible faulting or slope instability processes, the near surface damage in the test area as well as the proof whether fission products are detected as atmospheric tracers are key questions to be answered. These questions are approached by an integrated study based on different seismological (Section B.2), infrasound (Section B.3), remote sensing (Section B.4), radionuclide monitoring (Section B.5), and modelling techniques which complement each other. As there is no easy concept to verify and characterize nuclear explosions, especially in a country where direct observations are difficult to assess, this study demonstrates and emphasizes the strength of an integrated multi-technology approach.

In this context, new methodical approaches are introduced to improve the depth estimate from teleseismic observations and to quantify uncertainties in the non-isotropic source component. The seismological study retrieves an independent absolute location based on a combination between seismological and remote sensing data. The relative location between the six North Korean nuclear tests is obtained by means of waveform cross correlation time lag data. The event depth is estimated for the first time by a joint inversion of source time function (STF) and waveform composition of direct and depth phases observed at small aperture, high-frequency arrays at teleseimsic distances. A full waveform moment tensor inversion (MTI) is applied and compared to results of previous explosions in North Korea. The source time overshoot and peak amplitude is compared to traditional body wave magnitudes (m_b) estimates. Additionally, the effect of topography on peak amplitudes is estimated by 2D-waveform modelling to assess the possible range of explosive yield. Infrasound observations and modelling is used to understand the earth-atmosphere coupling and the propagation of infrasound from the North Korean test site. The analysis of satellite based remote sensing data is important to improve the absolute location of shallow sources as well as to quantify the secondary mass movement effects at the surface. Radionuclide monitoring demonstrates the importance of ATM to avoid over-interpretation of variations in 133Xe concentrations. While radionuclide monitoring provides the only direct evidence of nuclear explosions, it is demonstrated by careful modelling how difficult it is to interpret such data and that early claims of causal anomalies have possibly been over-interpreted.

B.2 Seismological investigations

B.2.1 Epicenter location

The localization in the Reviewed Event Bulletin (REB) of the CTBTO International Data Center (IDC) uses 125 seismic stations of the IMS and results in an epicenter of 41.321°N and 129.035°E with an error ellipse area of 110 km^2. This relatively high error is generated by the fact that only eight IMS stations are located at distances from 400 km up to 2100 km (see Figure B.1a).

However, the incorporation of 25 additional seismic stations in regional distances cannot significantly improve the absolute location estimate, as the closest station MDJ is still 372 km away from the test site. Due to these large source-receiver distances a further improvement of the absolute location accuracy is limited. Nevertheless, relative location methods can be applied for a high precision localization of the events (Zhang and Wen, 2013; Zhao et al., 2014, 2016; Gibbons et al., 2017b). In this study a relative location procedure based on the cross-correlation of seismograms from 33 regional seismic stations for the six North Korean tests is applied. Seismograms for the past North Korean events significantly vary between the stations, due to propagation paths from source to the surrounding stations at different

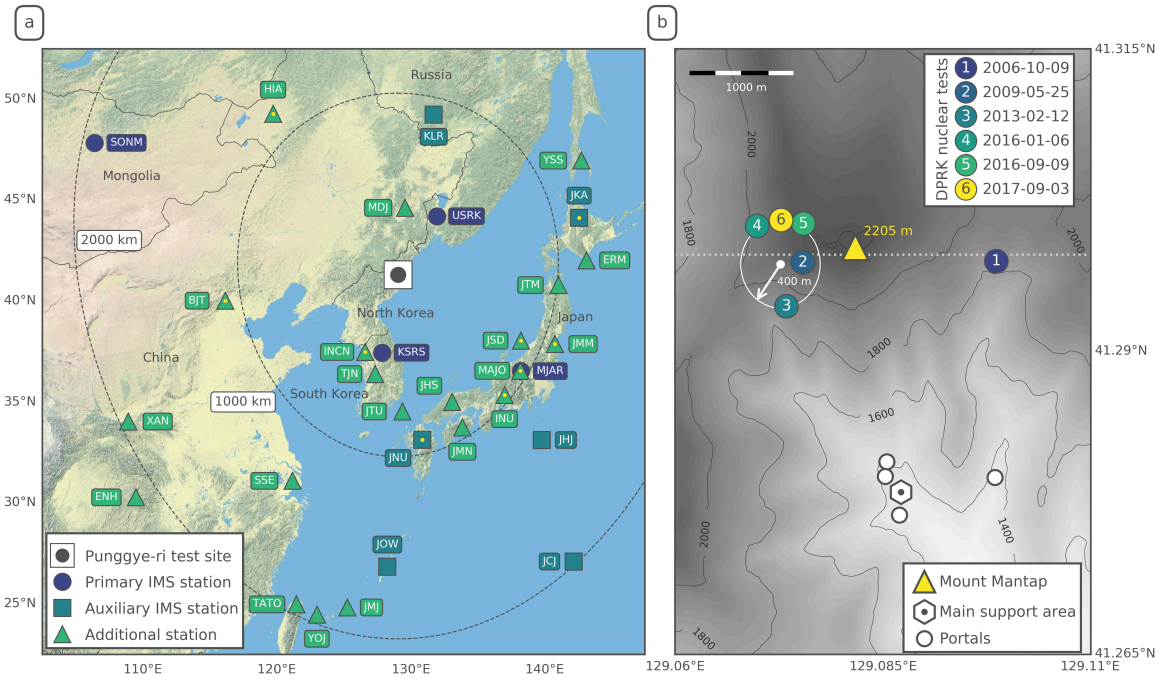

Figure B.1: (a) Seismic stations of the International Monitoring System and other earthquake monitoring networks within a radius of 2100 km from the North Korean Punggye-ri nuclear test site. Stations that are used in the moment tensor analysis in Subsection 2.3 are marked with a small yellow dot. (b) Zoom into the Punggye-ri test site area. Numbered circles indicate the absolute locations of the six North Korean nuclear tests. The relative location error for each test is less than 100 m. Dashed line marks the profile used in Subsection B.2.5 to study of topographic influence of the Mt. Mantap on seismic energy generation and radiation from the test.

distances and azimuths. However, the correlation of the seismograms of the six events for each individual station shows a good coherence between the corresponding signals with the *Pn*-phase being the most pronounced arrival in the waveforms. These signals are correlated for each individual station, which has recorded at least two North Korean nuclear tests. The cross-correlation between each pair of events is performed using normalization to 1.0 for the auto-correlation of each signal at zero lag. Maximum correlation values of 0.7 to 0.99 are obtained for stations up to 1100 km distance for the four tests in the years 2009, 2013 and 2016. Due to significant differences in explosive yield, and therefore different source time durations, the 2006 and 2017 test are slightly less correlated with the other tests. See Figure B.2 for the complete results of the cross-correlation analysis.

The estimation of time lags turned out to be reliable, when the maximum cross-correlation values exceeded a threshold of 0.4. With this constraint, a subset of 165 event pairs for 19 stations was selected, for which precise travel time differences with an accuracy in the order of the used sampling rate of 0.025 s could be determined. *Pn*-phase onset times of all tests are aligned to the onset at the closest station MDJ and fixed as relative start time for the estimation of the correlation time lags at the other stations. A double difference method (e.g. Waldhauser and Ellsworth, 2000) is applied to cross correlation time lags and results suggest that the last five events are located within a radius of 400 m, while the 2006 test is located around 2 km further to the east (see Figure B.1b). The relative locations of the six tests can be associated to absolute coordinates as soon as the geographical coordinates of one of the tests are known. The geographic, absolute location of the January 2016 nuclear explosion is fixed by means of radar interferometry data to the location of the maximum surface deformation observed after the test (Hartmann et al., 2017; Wei, 2017). The absolute epicenter location of the 2017 test from relative location procedures is consequently

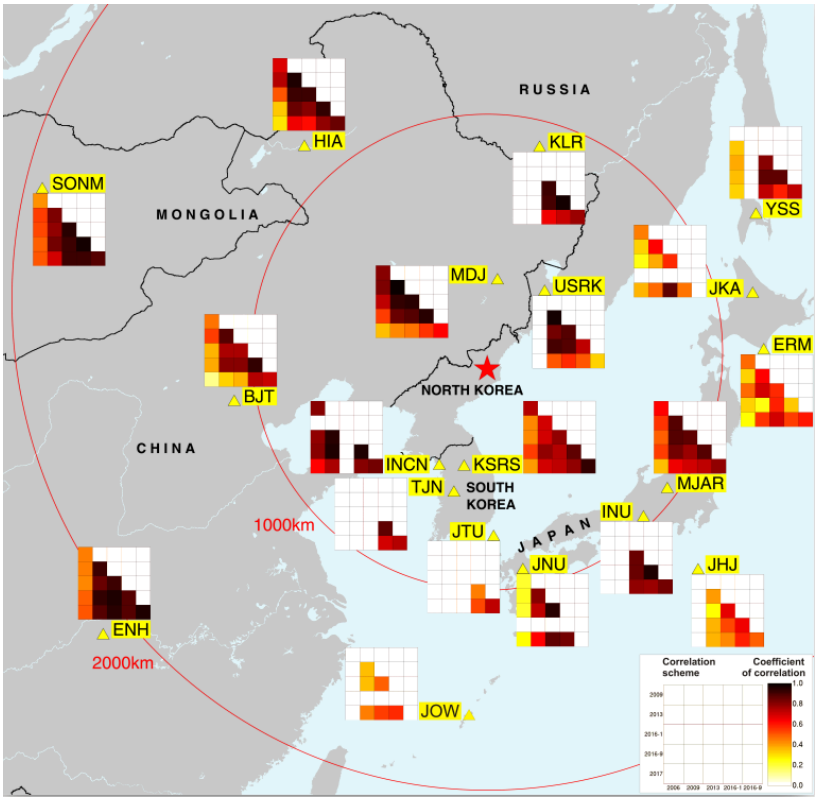

Figure B.2: Maximum correlation coefficients for the coherence of the *Pn*-phase for all available pairs of nuclear tests at 18 stations in regional distances of up to 2100 km. Due to their similar size in explosive yield, the four tests in the years 2009, 2013 and 2016 have a similar source mechanism and consequently show high maximum correlation coefficients between 0.70 and 0.99. The seismic signals for the 2006 and 2017 test are in general less correlated with the other tests due to the different source durations suspected for these two events. The 2006 and 2017 are the smallest and largest explosion, respectively.

determined to be 41.3007°N, 129.0728°E (Figure B.1b).

B.2.2 Estimation of hypocenter depth and seismic moment

The source depth is needed to estimate the explosion process and strength of the seismic source. However, constraining the depth of a shallow source is difficult from regional and teleseismic data without a close station within a focal depth's distance from the source. The modelling of the wavelet consisting of a surface-reflected *P*-phase, so-called depth phase, and STF can potentially help in such a case. Such a wavelet modelling approach resembles the inverted and time-shifted STF and needs high-frequency waveforms above 1 Hz to resolve the onset of the depth phase, and may be difficult to be performed from single station recordings if the signal to noise ratio (SNR) is poor at teleseimsic distances. An approach uncommon for nuclear test studies is used, which was established for the analysis of induced seismicity, where waveform beams are calculated at several small-aperture, short-period arrays to enhance the SNR (Figure B.3a).

The beam waveforms represent a superposition of direct and reflected waves. The depth of the explosion is estimated by comparing observed and synthetic beam waveforms (Figure B.3d), which are calculated for the best moment tensor solution described in Subsection B.2.3, a common STF and varying depths. The source time is represented as a composition of multiple basis functions with unknown weighting coefficients, which are estimated in a least squares inversion with smoothing constraint (Figure B.4). If $u(t)$ is the seismogram (beam) at the array with coordinates $\mathbf{r}_r$ and from a seismic source with coordinates $\mathbf{r}_s$, the

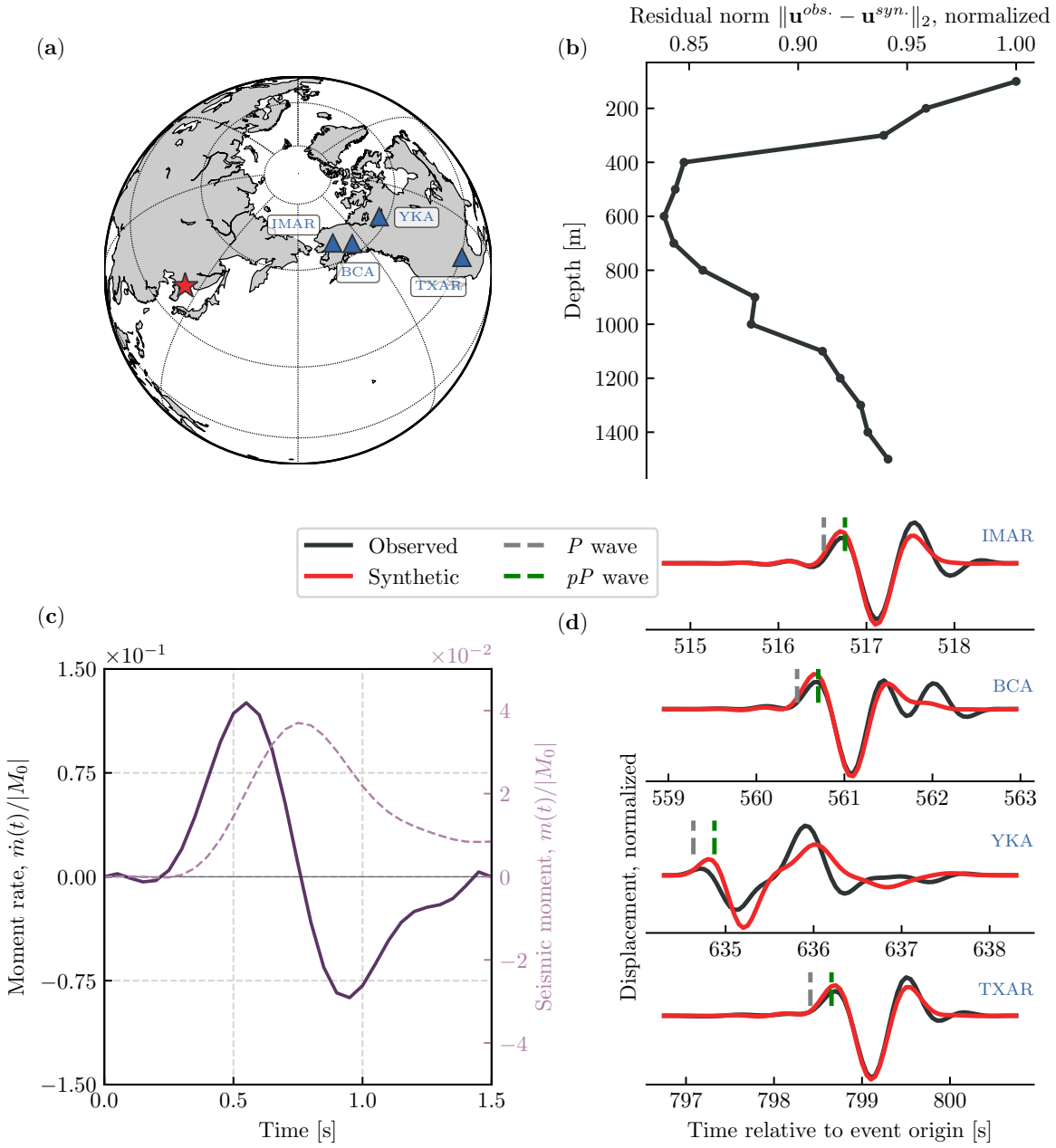

Figure B.3: (a) Setup of the depth analysis with the 2017 North Korean nuclear test marked as red star and the four small-aperture, short-period arrays marked as bluish triangles. The epicentral distances to arrays IMAR, BCA, YKA and TXAR are 48°, 54°, 65° and 94°, respectively. (b) Residuals between observed and synthetic waveforms (L_2-norm) as a function of depth of the explosion. (c) Least squares source time function associated with the best-fit regularized solution. Solid and dashed lines are the normalized moment rate and moment function, respectively. (d) Observed (black) and synthetic (red) waveforms for the best-fit regularized solution at 600 m depth. The gray and green dashed lines indicate the theoretical arrival times of the P-and pP-phases, respectively. The traces are bandpass-filtered between 0.5 and 2.5 Hz.

P-wave train (i.e. *P*- plus *pP*- plus *sP*-phase) at time t is represented by:

$$u(t) \quad = \quad \{M_{jk} G_{j,k}(\mathbf{r}_s; \mathbf{r}_r; t)\} * m(t)\,, \tag{B.1}$$

where $*$ is a time convolution and where the summation convention is applied. $G_{j,k}$ are the spatial derivatives of the Green's function, where the comma before index $_{,k}$ indicates a spatial derivative with respect to x_k. It is assumed that all moment tensor components M_{jk}

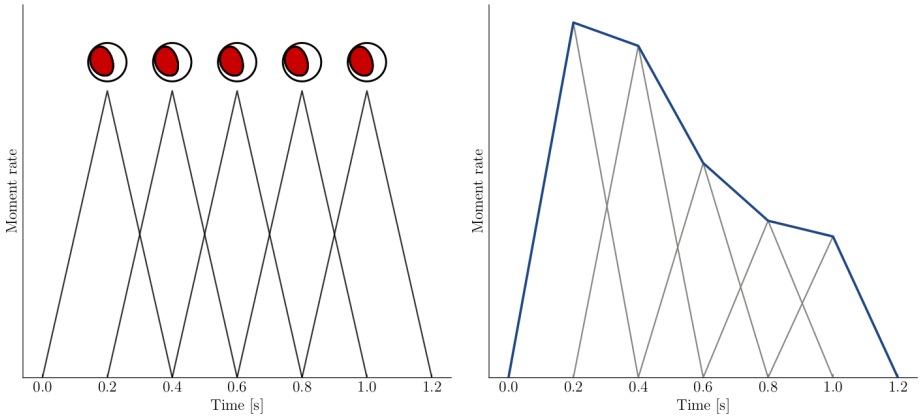

Figure B.4: (Left): Schematic sketch of five triangular basis functions $h_l(t)$ with equal weight of 1 and with a duration of 0.4 s each. The focal sphere symbols indicate that the orientation of the source mechanism is assumed constant during the rupture process. (Right): Simulation of a complex moment rate function (blue line) by applying different weights to h_l and linear superposition.

have the same time dependency, which is described as normalized moment function $m(t)$ with $m(t \to \infty) = 1$. The displacement in the far-field is controlled by the time derivative of $m(t)$, which is declared as moment rate function $\dot{m}(t)$. This explains that the far-field body-wave pulses from earthquakes are single-sided pulses (Dahm and Krüger, 2014). Since only the far-field wavefield is considered, the Green's functions in (B.1) are replaced by far-field Green's functions $G^{(ff)}$, and $m(t)$ is replaced by $\dot{m}(t)$. The inversion is set up for $\dot{m}(t)$ using a set of N time-shifted triangular basis functions $h_l(t)$ (Figure B.4):

$$\dot{m}(t) = \sum_{l=1}^{N} \beta_l h_l(t)\,, \tag{B.2}$$

where β_l is a weighting factor and each $h_l(t)$ satisfies $\int h_l(t)dt = 1$.
Hence, equation (B.1) is written as:

$$u(t) \;=\; \left\{ M_{jk} G^{(ff)}_{j,k}(t) \right\} * \left[\begin{array}{cccc} h_1(t) & h_2(t) & \dots & h_N(t) \end{array} \right] \cdot \left[\begin{array}{c} \beta_1 \\ \beta_2 \\ \vdots \\ \beta_N \end{array} \right] . \tag{B.3}$$

The convolution in (B.3) can be written in discrete form, leading to an over-determined matrix system for unknown weighting factors to be solved in a least squares sense using the L_2-norm (Dahm and Krüger, 2014). If more than one array is available, the equations are added to the coefficient matrix to realize a joint inversion. Additionally, the STF inversion is stabilized by using a regularization with a roughness matrix. The STF is inverted for every single trial depth. The length of the STF is constrained to 1.5 s, where 0.5 s are considered before the arrival of the P-wave. It should be noted that, with shorter length of STF, the details of the STF with a complex structure are difficult to resolve. On the other hand, with longer length of the STF, i.e. larger number of basis functions, the fitted curve oscillates wildly and gives a very poor representation of the model, which is known as over-fitting. The length of the STF mentioned before was chosen to reach a compromise, after examining the residual misfit in total signal variance computed for different lengths of source time function. In order to compensate travel-time residuals occurring along the mantle ray zero-lag Green's functions are correlated with P-wave beams at every array, and the travel-time corrections

are considered before the inversion. The source depth itself is estimated using a grid search approach, where the depth of the point source Green's functions is sampled from 0 to 1500 m in 100 m steps. For every depth solution the residuals are estimated and stored for final evaluation.

Green's functions are calculated using the code QSEIS (Wang, 1999), where source and station specific crustal models can be considered. 1-D global velocity model ak135 (Kennett et al., 1995) is used for the mantle, while different crustal profiles for source and station regions are taken from CRUST2.0 (Bassin et al., 2000). Intrinsic attenuation for P-waves is set to 5000, since otherwise high frequencies are damped out at teleseismic distances. The sampling frequency is 20 Hz. The grid search depth phase modelling has been applied previously to different cases of induced seismicity (Dahm et al., 2007) and the 2016 nuclear explosion (Cesca et al., 2017), but the simultaneous STF inversion is implemented for the first time in this study.

The full waveforms of beams, their peak heights and peak distances are well fitted in a joint inversion of four arrays. The best fits are obtained at depths between 400 to 800 m (Figure B.3b). However, it should be noted that the depth value obtained from the inversion procedure might be overestimated due to the use of an unperturbed velocity model. Perturbations in the velocity model for example through potential fracturing above the explosion, which would substantially reduced P-wave velocity, were neglected. If the source of the synthetic beams is placed deeper or shallower, the duration and appearance of the P-, pP- and sP-pulses changes and residuals increase (compare Dahm et al., 2007). Interesting are the retrieved moment rate and moment function, which show a clear double pulse and overshoot, respectively (Figure B.3c). Such an overshoot is not expected for the rupture process of tectonic earthquakes, where the moment rate and moment functions of the P-wave are single-sided pulse and monotonically increasing functions, respectively. However, this feature is commonly observed for nuclear explosions. This can be explained by at least a partial collapse of the explosion cavity immediately after the explosion. In this case, the final moment is only 23% of the peak moment in Figure B.3c. The inversion of long-period waves led to a seismic moment M_0 of 2.33×10^{17} Nm, representing the time after the overshoot. The peak seismic moment is thus estimated in the range of $M_0^{(\mathrm{peak})} \approx 1.02\times10^{18}$ Nm. The associated low and high frequency moment magnitudes (M_W) are M_W=5.55 and $M_W^{(\mathrm{peak})}$=5.97, respectively, and can explain the large difference between the long period M_W and the high-frequency m_b estimates which emerged during the magnitude estimation described in Subsection B.2.4.

B.2.3 Moment tensor inversion of the test and the main aftershock

Seismic signals of the 2017 North Korean test show a great similarity to those generated by the previous four nuclear tests conducted in 2009, 2013, and 2016. Especially long period waveforms with periods above 10 s recorded at regional distances show a high waveform similarity and a substantially increased amplitude, revealing a very similar radiation pattern of all events and a larger moment release for the 2017 nuclear test. In recent years, MTIs have been performed for nuclear tests in North Korea, including those carried out in 2009, 2013 and 2016 (Ford et al., 2010; Barth, 2014; Vavryčuk and Kim, 2014; Cesca et al., 2017; Hartmann et al., 2017). All MTI were performed by fitting low-frequency full waveform seismic data at regional distances, either in the time or in the frequency domain. The majority of these solutions revealed a significant positive isotropic component. For the 2013 nuclear test an extraordinary high double couple (DC) component was found, indicating differences in containment or near source damaging effects (Barth, 2014; Vavryčuk and Kim, 2014). For

the 2017 test the seismic moment tensor is inverted by fitting the low frequency amplitude spectra (epicentral distances up to 1200 km) and full displacement waveforms (epicentral distances up to 600 km) in the frequency range from 0.02 to 0.04 Hz following the approach by Cesca et al. (2013, 2017). For the moment tensor optimization the *Grond* algorithm (Heimann et al., 2018) is used, which searches the parameter space by random search first and later by an increasingly denser search around the best solutions. The algorithm finally resolves the full moment tensor components, the centroid location and centroid time, and also provides information on model uncertainties and source parameters trade-offs. Full waveforms and their spectra are calculated assuming a layered crustal model proposed by Ford et al. (2010). Example full waveform displacement and amplitude spectra fits are shown in Figure B.5.

The moment tensor solution for the 2017 test shows a dominant positive isotropic part of 60%, 16% positive compensated linear vector dipole (CLVD), and 24% of DC. The best solution, found at a depth of around 2 km, has a scalar moment of 2.33×10^{17} Nm, equivalent to a M_W of 5.55. The centroid depth is poorly resolved and good waveform fits are found for very shallow sources down to 2.5 km. This result confirms the very shallow depth of 400-800 m accurately resolved by the analysis of depth phases in Subsection 2.2. The moment tensor optimization resolves a broad ensemble of well fitting moment tensor solutions. They are plotted using a source type diagram in Figure B.6 and are characterized by strong deviations from a pure DC model (mapping in the center of the diagram), a typical model for tectonic earthquakes. Instead, acceptable solutions are either dominated by a positive isotropic component (positive values of the y-axis in the plot), a negative vertical CLVD (positive values of the x-axis), or a combination of both. The variability among these type of solutions has been attributed to trade-off among moment tensor components for very shallow sources (Cesca and Heimann, 2017; Cesca et al., 2017). This range of moment tensor solutions includes alternative moment tensor configurations as proposed for previous nuclear explosions in North Korea (e.g. Barth, 2014).

In the aftermath of the nuclear test, a seismic event took place in its direct vicinity around eight minutes later. The estimated scalar moment and M_W are 1.88×10^{16} Nm and 4.81, respectively, and thus the scalar moment is only ∼8% of the one of the nuclear test. The waveforms of the aftershock still show a sufficient SNR to perform a MTI. Waveform displacement and amplitude spectra fits of the MTI are shown in Figure B.7.

The inversion is based on spectral and waveform fits at stations located within 1000 km epicentral distance, filtered between 0.02 and 0.04 Hz. The calculated depth of the aftershock is similar to the depth of the explosion. The best MTI solution suggests a dominant implosive source component (65%), negative CLVD (29%) and a DC component of 6%. This source mechanism is compatible with a shallow collapse source or might hint to some kind of break-in process. An ensemble of well fitting moment tensor solutions for this inversion is shown in Figure B.8.

B.2.4 Magnitude and yield estimation

The determination of m_b is the prerequisite for a reliable estimation of the yield of a nuclear explosion. In order to obtain comparable results for the past six North Korean events, m_b is calculated from waveform peak values measured at always the same 15 IMS seismic stations that recorded all six events. These stations (MKAR, INK, FINES, WRA, YKA, ASAR, AKASG, HFS, NOA, VRAC, GERES, STKA, DAVOX, NVAR, PDAR) cover the entire azimuthal range with a maximum gap of 121 degrees and are located at distances between 3700 and 9000 km from the Punggye-ri test site. Exemplary, the seismic signals at

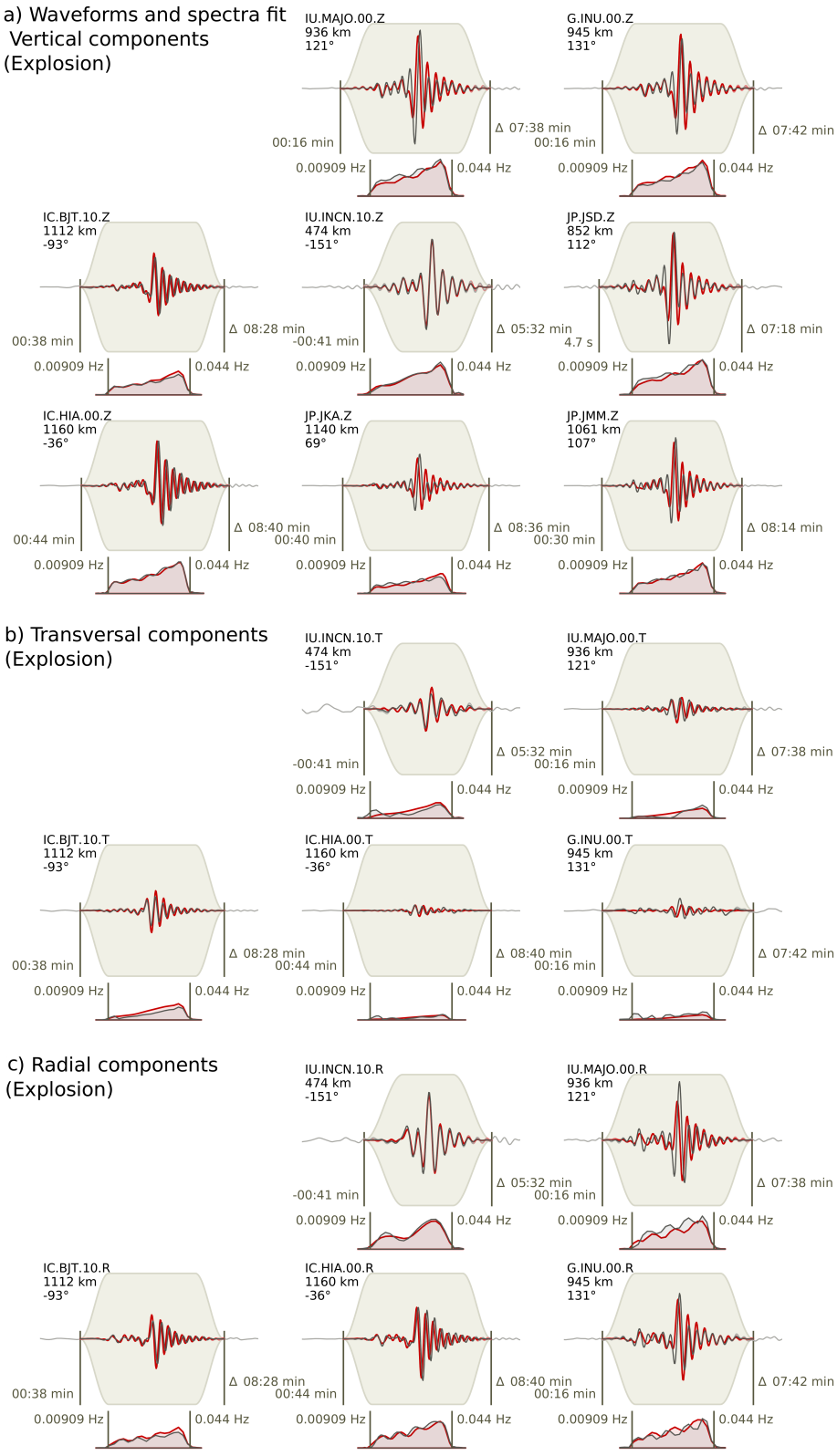

Figure B.5: Full waveform displacement and amplitude spectra fits (gray and redc lines denote observations and synthetics, respectively) are shown for the nuclear explosion for the vertical (a), transversal (b), and radial components (c). Top left side of each plot reports the trace component (network, station, location, and component codes), epicentral distance, and azimuth. Waveform plots report the starting time (relative to the origin time) and duration (in minutes and seconds) of the time window used (the gray background represents the applied taper), while spectra plots report the frequency range in Hz. For geographical locations of the used stations see Figure B.1a.

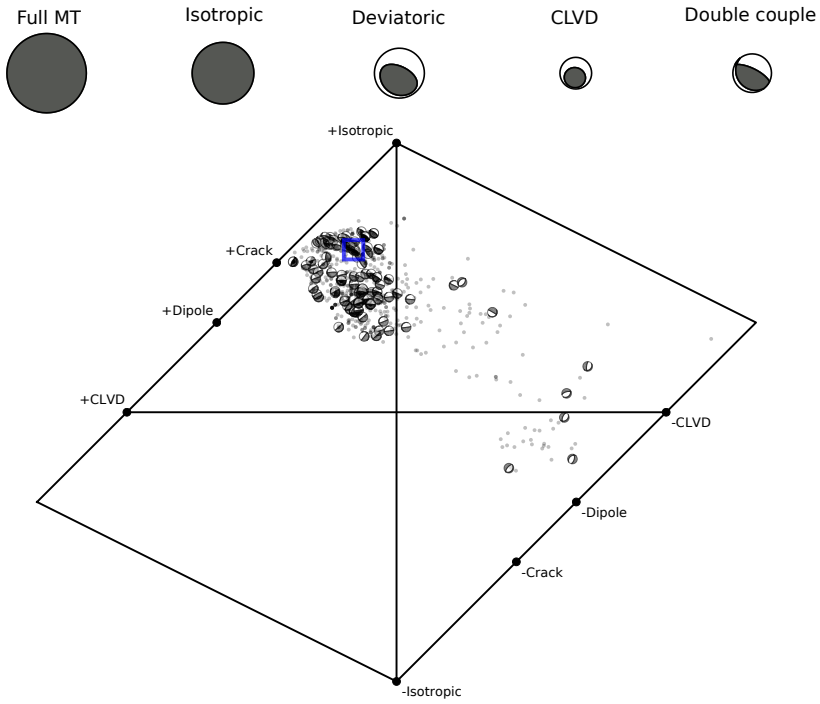

Figure B.6: (top) Best moment tensor decomposition. The moment tensor decompositions reports the focal sphere for the full moment tensor, and its isotropic and deviatoric components. The deviatoric component is further decomposed into CLVD and DC terms. The relative size of focal spheres scale with their relative magnitude. (bottom) Source type plots. The source type diagram after Hudson et al. (1989) is used to judge the moment tensor decomposition, illustrating the ensemble of best fitting solutions. Figure shows both solutions based on all available data, as well as using data sub-samples upon bootstrapping. The position of each solution (circles, focal sphere for selected solutions) illustrates the MT decomposition, while the focal spheres (shown for selected solutions only) illustrate the geometry of the DC term. The decomposition of the best solution is denoted by a blue square.

the German primary seismic station GERES are shown in Figure B.9. The high similarity between the six nuclear explosions is standing out due to the short and simple *P*-wave train. The recordings differ only in the amplitudes. The resultant single station magnitude for GERES was used together with the corresponding magnitudes of the other 14 involved stations to obtain reliable and comparable average magnitudes.

For the 2017 test a m_b of 6.2 is calculated, compared to m_b values of 4.1 to 5.3 for the five preceding tests. In general it is not possible to state one single relation between magnitude and yield, as this relation depends on various factors, such as the geological setting at the source site, the efficiency of wave propagation from source to receiver, the depth of the explosion and the coupling of the source to the underground. A number of empirical formulas of the type $m_b = A + B\log(Y)$, with Y being seismic yield in kilotons TNT equivalent and A and B being constants depending on the aforementioned factors, have been developed to relate yield and m_b. These relations have been successfully used for yield calibration for example at the Nevada test site (Murphy, 1981), in Kazakhstan (Ringdal et al., 1992) or in Nova Zemlya (Bowers et al., 2001). As no particular magnitude-yield relation has been approved so far for the North Korean test area, the latter relation by Bowers et al. (2001) is used in this study. The North Korean nuclear explosions were mainly conducted beneath the Mt. Mantap complex, consisting of stratified volcanoes covering a basement of granite and diorite. In general, wet hard rock can be taken into account for these geological conditions, when the yield is estimated on base of the seismic magnitude. Under these assumptions a yield of around 400 kilotons TNT equivalent is estimated for the September 2017 test, clearly

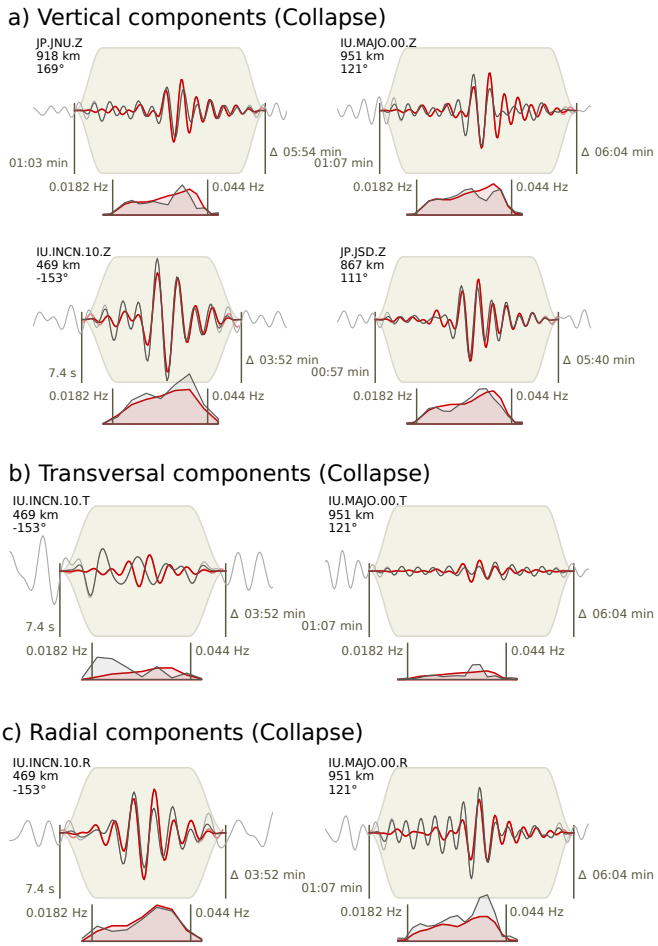

Figure B.7: Same as Figure B.5, but for the aftershock around eight minutes after the test.

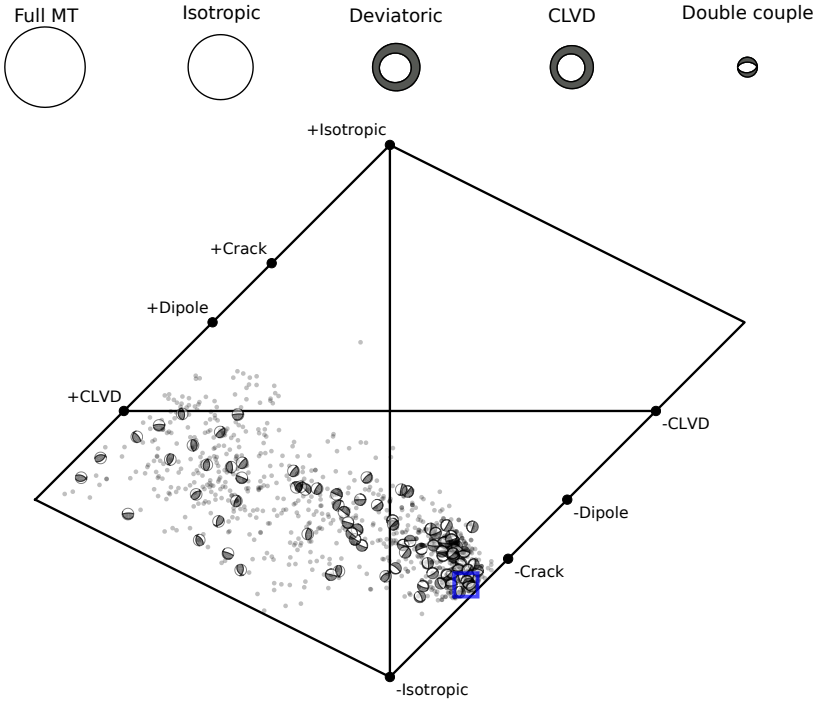

Figure B.8: Same as Figure B.6, but for the aftershock around eight minutes after the underground test.

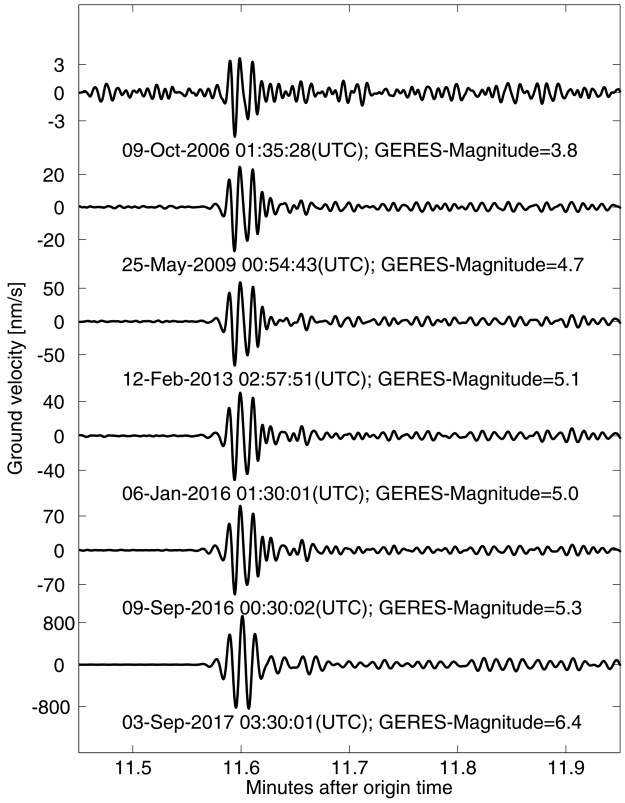

Figure B.9: Beam seismograms calculated from the vertical components of the GERES array showing the P-wave of the six North Korean nuclear explosions. The seismograms are normalized to the individual maximum amplitudes, for which the station magnitude is estimated.

illustrating a steady increase of explosive strength of the nuclear tests (see Figure B.10).

B.2.5 Influence of the Mt. Mantap topography

Two-dimensional synthetic wave-field simulations are used to study the influence of topography of the Mt. Mantap complex on the propagation of P- and S-wave energy emitted by a point-like explosion source. A Chebyshev pseudo-spectral method (e.g. Tessmer et al., 1992) is used for modelling the elastic wave-fields on a Cartesian 820×512 grid for an 8 km×5 km box in x- and z-direction, respectively. No variation of medium properties is assumed in the y-direction. Figure B.11 shows the model configurations as well as the wave propagation for an explosion source at 0.6 km depth below surface (see Subsection B.2.2).

The source time function is taken from Glasstone and Dolan (1977, Chapter 6), where the source duration is 0.15 s. The wave-field V is separated in divergence ($|\nabla \cdot V|$) and curl ($|\nabla \times V|$) reflecting the P- and SV-energy, respectively. Moreover, the wave propagation is considered for one model without and two models with topography; whereas the topography is considered for a west-east profile along 41.3°N crossing the Mt. Mantap massif (see Figure B.1b). The velocity model is chosen such that it reflects the petrology of the local geology as described by Coblentz and Pabian (2015). However, strong lateral variations as thrust or normal faulting in the uppermost layers are not taken into account due to reasons of numerical stability. Instead lateral variations, which are based on an exponential perturbation with a correlation length of 100 m, are considered with differences in density, P- and S-wave velocities of ±3%. Merely, the last model accounts for erosion of the uppermost basaltic and volcanic layers as well as an almost vertical dyke reflecting the transition between the granodiorites and the granite from west to east. Nevertheless, computing the P-divergence

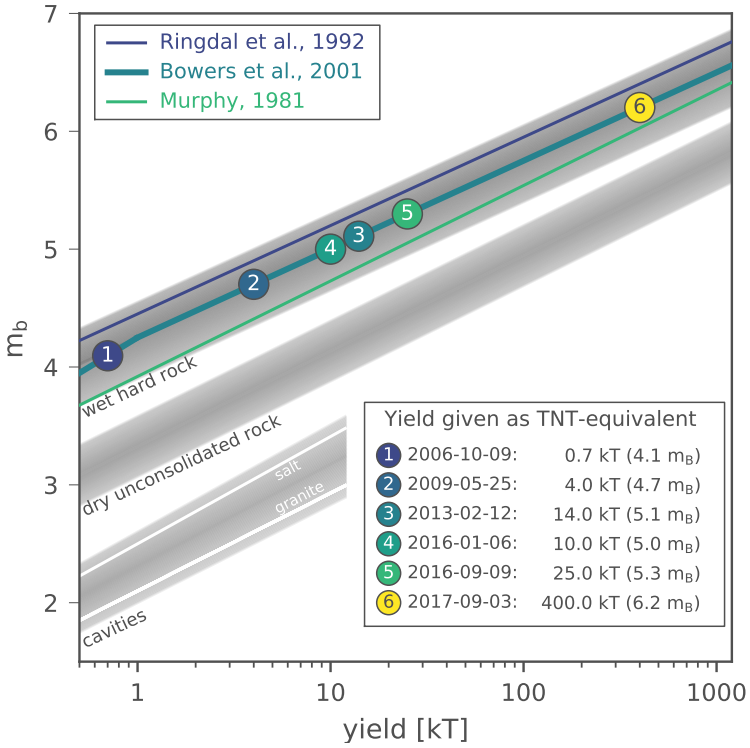

Figure B.10: Magnitude-yield relation curves for different geological settings. Numbered circles indicate the six North Korean nuclear tests. Gray background shading represents lower and upper boundary literature values for the different environments.

and SV-curl in a rectangular box shows large differences in the downward propagating wavefields, where strong increases for both pP- and pS-wave amplitudes can be observed. The position and the lateral extent of this box covers a slowness range from -9 $s/°$ to +9 $s/°$, which are typical slowness values for teleseismic P-waves. For a source under Mt. Mantap surface reflections are increased in their amplitudes by a factor of ∼1.5 due to topography.

Wave energy is focused due to the shape of the mountain, especially from the easterly flank with a change in altitude of approximately 600 m (see Figure B.1b). Topography is the crucial factor, the difference between the two simulations with and without a realistic geologic setting (see Figure B.11, middle and right panels) is negligible. Further simulations for sources shallower and deeper as the reference value of a depth of 0.6 km below surface provided similar pictures; whereas for sources shallower than 0.5 km and deeper than 1.7 km, respectively, energy focusing is less pronounced with amplifications in amplitude of 1.3 and less. Although only a two-dimensional model is considered, such simulations are also valid for the three-dimensional nature because Mt. Mantap exhibits a high symmetry. In general, this numerical modelling gives indications for: (1) generation of clear infrasonic signals (see Section B.3), because topography (slope of Mt. Mantap) increases the amount of radiated acoustic energy in sub-horizontal direction, which is the usual propagation path for infrasound (compare Figure B.12), (2) a reduced value of the isotropic part obtained by MTI because a larger amount of S-wave energy is generated in the source region due to topography effects above the source (see Subsection B.2.3), (3) an overestimation of the yield of the explosion, because P- and pP-phases are considered as a single onset in teleseismic distances and in the investigated frequency range for shallow sources, leading to an increase in maximum P-wave amplitude of approximately 1.3 and hence in m_b of around 0.1, respectively, and (4) no effect on differential travel times between P- and pP-phases due to topography, therefore no effect on hypocenter depth estimation using depth phase modelling (see Section B.2.2).

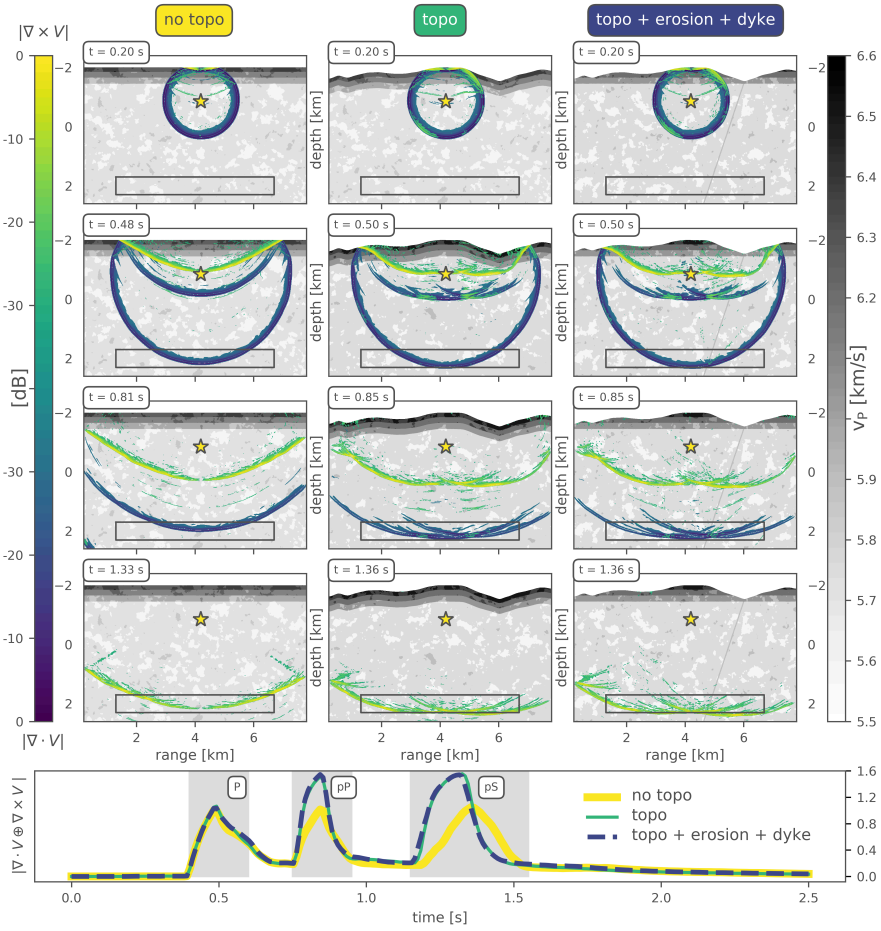

Figure B.11: Snapshots obtained by and velocity model used for numerical simulations. P-wave velocities are indicated by shading according to the gray scale map (for S-wave velocities we assume a v_P/v_S-ratio of 1.73), as well as logarithmically scaled divergence (P-wave energy) and curl (SV-wave energy) by bluish and greenish colors, respectively. The left paneled snapshots show the P- and SV-wave separated propagation for an explosion source without topography, the middle panels with topography across the North Korean test site for a West-East profile along 41.3°N with Mt. Mantap in the middle. The right panel shows is similar to the middle panel, but with a more realistic geological setting, where erosion is accounted for. The time stamp of each snapshot is displayed in the upper left corner. The point source is beneath the center of Mt. Mantap in a depth of 0.6 km below surface. The panel below the snapshots compares the summed average divergence and curl computed every 0.02 s in a rectangular box below the source for the case without (yellow) and the cases with (green and blue) topography. The downward propagating wave-field shows strongly increased amplitudes for pP- and pS-phases in both cases of topography.

B.3 Infrasound observations

For a shallow event in the given magnitude range it is expected to record infrasound signals in distances of up to hundreds of kilometres (Mutschlecner and Whitaker, 2005). Infrasound is sub-audible sound below the human hearing threshold of 16 Hz and is the dedicated monitoring technology of the CTBTO for remotely detecting atmospheric explosions. Furthermore, infrasound can be used in civil and scientific applications such as the monitoring of volcanoes, meteoroids, ocean swell and various other natural and anthropogenic activities (see Le Pichon et al. (2010) for a comprehensive overview). Infrasound signals are also generated by strong underground or underwater sources when the generated waves couple into the atmosphere. The North Korean tests between 2006 and 2016 were investigated and registered by various infrasound arrays (Che et al., 2014; Assink et al., 2016; Park et al., 2018; Koch and Pilger, 2018). Detections of the 2013 test by the IMS stations I30JP in

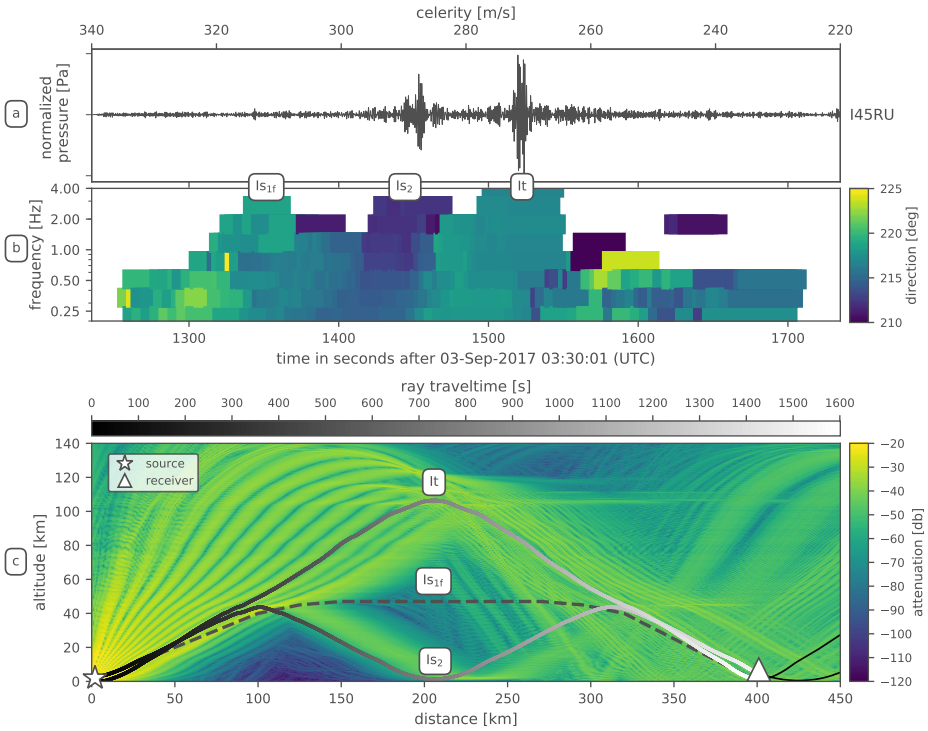

Figure B.12: (a) Waveform beam of the 4-element infrasound array I45RU with corresponding celerity values. (b) Progressive Multi-Channel Correlation analysis in the same time frame for signal frequencies between 0.2 and 4 Hz. Information on back-azimuth direction is color coded. True back-azimuth from test site to station is 218°. (c) Propagation modelling using ray tracing with gray-shaded travel-time information for eigenrays from the test site to the station and color coded attenuation information from parabolic equation modelling. Is_2 and It denote the corresponding stratospheric and thermospheric arrivals after 1450 s and 1520 s, respectively. Is_{1f} shows the early signal detection and theoretical ray-path for an infrasonic forerunner.

Japan and I45RU in Russia were part of the REB and thus confirmed the underground nuclear test as source of infrasound waves. For the 2017 test, the station I45RU, located in a distance of 401 km from the test site, detected infrasound signatures from the nuclear test (see also Assink et al., 2018). Clear waveforms undoubtedly associated to the nuclear test were recorded and were again part of the REB. Figure B.12a highlights the waveform beam of the Russian 4-element infrasound array I45RU (denoted as the co-located seismic station USRK in Figure B.1a).

Coherent waveform signals can be observed and associated to infrasound propagation from the nuclear test site arriving at I45RU after travel times of 1450 s and 1520 s, corresponding to celerities of 290 m/s and 270 m/s, respectively. Preceding waveform activity at around 1350 s (315 m/s) can either be associated to infrasound radiation from an extended (near-)epicentral source region or the fast acoustic phase of an infrasonic forerunner (Evers and Haak, 2007). These values are in the pure acoustic range and indicate stratospheric ducting (Is_2 with two reflections and Is_{1f} with one elongated reflection, turning heights of 40 to 55 km) and thermospheric ducting (It, turning heights above 100 km) (Drob et al., 2003). It is the first time that an underground nuclear test is strong enough to generate distinct and far-reaching pressure signatures that were clearly recorded at a remote IMS infrasound station after propagation through the thermosphere above 100 km altitude. The corresponding Progressive Multi-Channel Correlation (PMCC, Cansi, 1995) analysis of the signal content in terms of time variation, frequency content and back-azimuth direction is illustrated in Figure B.12b. The PMCC method draws rectangular time-frequency-windows wherever cor-

related signal energy in three or more array elements is present. Colour-coded back azimuths between 210° and 225° (south-west) point towards the Punggye-ri nuclear test site with a true back-azimuth of 218°. Effects from cross winds (west to north-west, strongest in the stratosphere) lead to the fact that the observed back-azimuths are some degrees lower, especially within the stratospheric duct. The PMCC signatures with broadband frequency content from 0.2 to 4 Hz can thus clearly be associated to the 2017 DPRK nuclear test.

Figure B.12c models the propagation from the test site epicenter to the station I45RU using parabolic equation and ray-tracing methods for the attenuation of signal amplitude and the connection of source and receiver by eigenrays. A combination of European Centre for Medium-Range Weather Forecasts (ECMWF) analysis data and climatological profiles is implemented for temperature and wind model backgrounds including gravity wave perturbations (see Koch and Pilger (2018) for further details on the methods and the atmospheric profiles used). The eigenrays show that the stratospheric phases are about 170 s and 70 s faster than the thermospheric phase (caused by a higher effective sound speed in the stratosphere and the longer wave path for the thermospheric phase). The signal attenuation, as obtained from parabolic-equation modelling, indicates that only a small portion of signal energy is ducted in the stratosphere caused by partial reflections from gravity wave variations of the stratospheric mean background. This leads to about 4 to 5 dB higher attenuation in the stratospheric duct and thus stronger signal amplitudes in the thermospheric duct by a factor of 1.6 to 1.8, which corresponds to the observed waveforms. The presented infrasound signals clearly observed even at 401 km distance and with disadvantageous propagation conditions are indicative for a strong surface movement in the epicentral area (see Section B.4) of the underground test generating large acoustic pressure peaks as argued in Subsection B.2.5. Apart from the strong epicentral surface movement, infrasonic signatures were also identified from seismo-acoustic coupling and the assumed cavity collapse associated to the eight minute subsequent aftershock (see the Supplement to this paper for further information).

B.4 Remote sensing studies

To visualize and characterize the surface imprint of the 2017 test radar data from the ALOS-2 satellite (Suzuki et al., 2009) and multi-spectral optical data from the Pleiades satellite (Gleyzes et al., 2012) are investigated. Data from the ALOS-2 satellite in the L-band (1257.5 MHz frequency, 3 m resolution) are analysed by Interferometric Synthetic Aperture Radar (InSAR) to investigate surface deformations (subsidence and uplift) correlated with the 2017 test and its aftershocks. The method of change detection analysis based on the Normalized Differential Vegetation Index (NDVI) is applied. Spaceborne InSAR has been used to detect surface displacements of the Earth's surface since more than 20 years (Massonnet et al., 1993) and has reached maturity in recent years (Adam et al., 2009), nowadays allowing for the detection of surface displacements with a precision in the order of a few millimetres. Repeat pass interferometry is based on the registered interferometric phase per ground cell (pixel) and is related to the distance differences between the scatterer and the SAR sensor between two acquisitions separated in time. The interferometric phase measured as moduli 2π is thus ambiguous. To solve this ambiguity, frequency estimations using unwrapping techniques are calculated. The Earth's curvature, topography and atmospheric effects influence the interferometric phase in addition to surface displacements. These phase contributions have to be estimated and subtracted to correctly estimate the surface displacement (Kampes, 2006). In addition, the backscattered electromagnetic signal between the acquisitions times needs to be correlated or coherent. Decorrelation can be caused by (1) temporal (large separation between the acquisitions in time), (2) geometrical

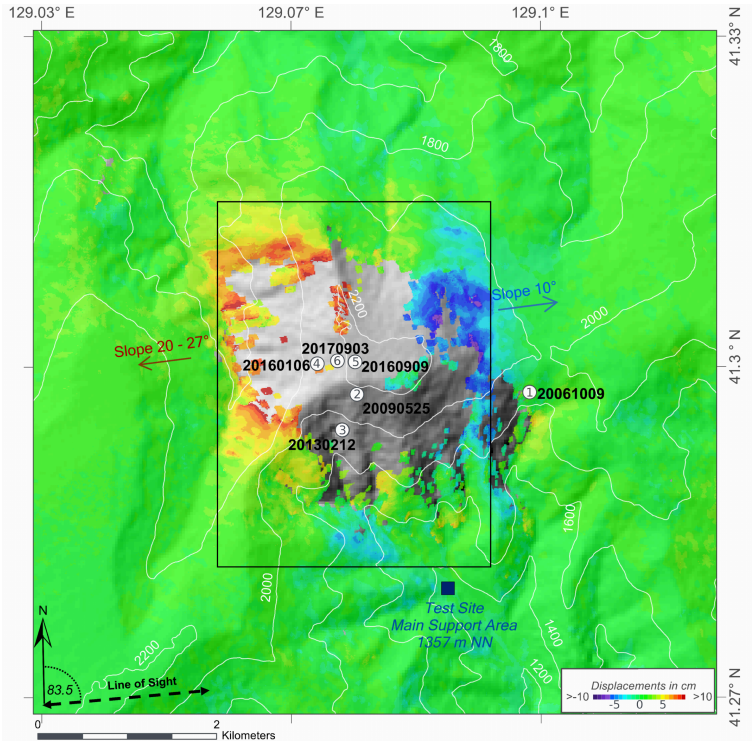

Figure B.13: Surface displacements from DINSAR analysis for the 2017 North Korean nuclear test in September 2017. Coherence threshold is set to 0.25. Data from the days August 29 and from September 12, 2017 are used. Arrows indicate slope direction and angle. Numbered circles indicate the epicenters of the tests from 2006 to 2017. Black solid box delineates an area of around 3×4 km^2 in which the surface displacement is between between -10 and 10 cm.

(large perpendicular baseline) and (3) scattering effects (incoherent movement of scattering elements within the pixel, Gatelli et al., 1994).

Differential InSAR (DInSAR) processing was adjusted to the test site target area regarding above mentioned constraints. As the investigated area is located in a mountainous region, DInSAR processing is challenging due to factors such as limited visibility for SAR acquisition geometry, tropospheric phase contributions and/or snow cover and vegetation causing temporal phase decorrelation. DInSAR processing encompasses following steps: co-registration, filtering, unwrapping and the discussion of coherence. Coherence serves as a measure of the quality in DInSAR studies, with coherence values ranging from 0.0 to 1.0, with 1.0 suggesting a perfect interferogram with no noise. For the analysis of the surface displacement due to the 2017 test, data from August 29 and from September 12, 2017 is used, data coherence between these two times has a mean value of 0.6 for the investigated area. For areas that show surface deformation the coherence values range from 0.2 to 0.8.

Figure B.13 shows the surface deformation at the test site during the 2017 test restricted to pixels with coherence values greater than 0.25.

In the central part of the Mt. Mantap massive, coherence values dropped significantly below 0.25 due to very strong ground deformations (see also Wang et al., 2018). The recognition of the displacements is only possible in line of sight in the direction towards or away from the sensor. Due to the incidence and look angle of the sensor measured with respect to the ground and north direction, respectively, it is not possible to fully resolve the amount of the vertical surface displacement caused by the 2017 nuclear test. During data acquisition on August 29 and September 12, 2017 the sensor had an incidence angle of 43° and look angle facing East North East. These angles combined with the topography of Mt. Mantap result in the maximum measurable percentage of vertical surface displacement. For the western

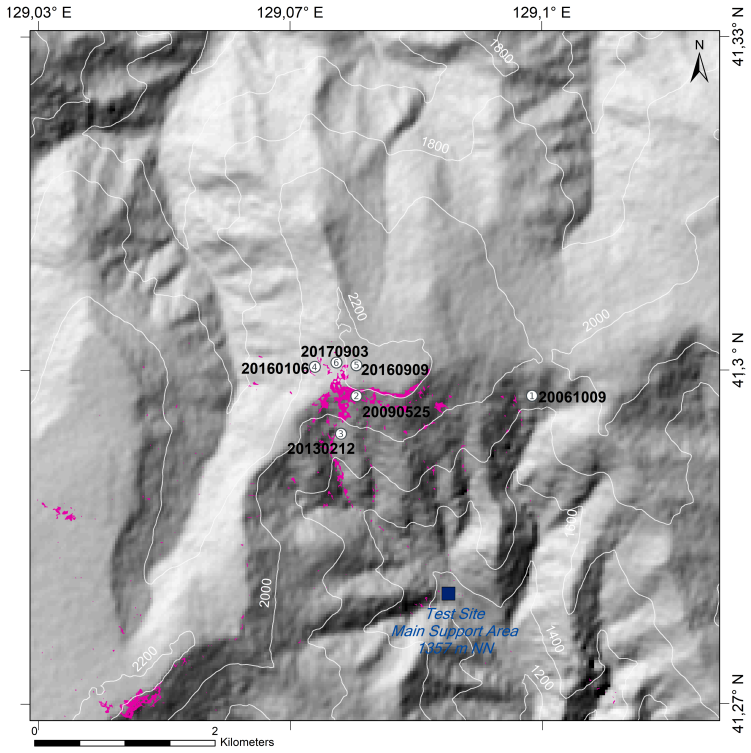

Figure B.14: Change detection analysis via NDVI (Normalized Difference Vegetation Index) from Pleiades data showing potential landslides (in purple patches) triggered by the 2017 nuclear test. Numbered circles indicate the epicenters of the tests from 2006 to 2017.

flank of Mt. Mantap pointing towards the sensor with a slope of around 27° the percentage of resolvable surface displacement is only around 30%, for the eastern flank pointing away from the sensor with a slope of around 10° the value of maximum measurable surface displacement increases to around 80%. The resulting map of resolvable displacements clearly shows an area of subsidence of up to 10 cm around 3 km north of the main support area (compare Figure B.1b), and an area with clear uplift of up to 10 cm west of the Mt. Mantap peak. DInSAR processing of C-Band Sentinel data and TerraSAR-X data for the 2017 test did not reveal acceptable quality measures regarding coherence in the central part of Mt. Mantap, whereas for the tests in 2016 Sentinel data did show excellent results (Hartmann et al., 2017; Wei, 2017). A study by Wang et al. (2018) shows additional results based on amplitude images from TerraSAR-X data and calculates 0.5 m subsidence in the centre and 3.5 m of horizontal displacement. This strong spatial and temporal coincidence of the displacement areas to the nuclear test site suggests a high correlation with the underground test. To validate the displacement maps of the DInSAR analysis of the nuclear test, Pleiades data sets from August 26 and from September 8, 2017 were processed to reveal surface characteristics related to the underground test (Figure B.14). This relation is concluded by the strong temporal and spatial connection of the landslides to the test and aftershock origin time and epicenter locations.

Change detection analysis show numerous landslides activated during the test and aftershocks. As a result of the processing of the ALOS-2 data, an area of around 3×4 km^2 can be delineated, where surface movement rates range between -10 and 10 cm. For comparison, the area of the January 2016 North Korean nuclear test, which showed comparable surface movement rates, was in the range of 1.5×1.5 km^2 (Hartmann et al., 2017). This large difference clearly underlines the enormous power of the 2017 nuclear test. The strong surface deformations at the surface observed for the 2017 test might lead to pathways and the sub-

sequent release of radionuclide, especially gaseous radionuclide such as ^{133}Xe, from the test site. Potential measurements of radionuclide are discussed in the following Section B.5.

B.5 Radionuclide monitoring and atmospheric transport modelling

Measurements of radioactive fission products released into the atmosphere even at far distances can deliver the definite proof of the nuclear character of an explosion. To assess the consistency between measurements and potential source locations the method of ATM is applied (Becker et al., 2007; Ross et al., 2017). For the ATM analysis of potential detections of radionuclide the Lagrangian Particle Dispersion Model HYSPLIT (National Oceanic and Atmospheric Administration – Air Resources Laboratory, Stein et al., 2015) is used. The ATM is operated with meteorological data from the US National Centers for Environmental Prediction (NCEP). For the prediction of potentially affected radionuclide measurement stations, HYSPLIT is operated in forward mode with hypothetical releases. For the assessment of the potential source region of detected radioisotopes the model runs in backward mode. Dispersion simulations of a potential immediate release after the explosion on September 3, 2017 show prevailing wind directions to the north east (Figure B.15a).

According to the forward simulations, the IMS station RN58 (Ussurysk, Russia) would have been affected, but was not operational at that time. Station RN38 (Takasaki, Japan) would have been missed by the plume from the potential release from the test site which is typical for the wind patterns of the season. Stations further downwind, for example in Northern America, would have required a larger release for activity concentrations to exceed the detection threshold.

The South Korean Nuclear Safety and Security Commission issued a press release on September 13, 2017 with results of national efforts to detect radioactive Xe isotopes after the test. The statement *'Considering the timing and location of sampling and air currents, the NSSC could conclude that the air currents from the North Punggye-ri area has been mixed to the sample and the Xe-133 detected from this air sampling is relevant to the sixth nuclear test of DPRK'* (Nuclear Safety and Security Commission, 2017) was interpreted by the media as source attribution. Backward simulations for the samples collected at the north-eastern stationary measurement system at Geojin were performed using 500,000 model particles per sample and 0.5° GDAS (Global Data Assimilation System) meteorological data. Additive overlay of the source regions of seven stationary 12-hour samples with elevated ^{133}Xe from September 7 to 10, 2017 points to the region where the Yongbyon North Korean Scientific Research Center is located, as likely coincident source (Figure B.15b), whereas the test site can be disregarded as common source for the seven samples. This contradicts the suggestions in the media that the detected ^{133}Xe originated from the test explosion.

Continued forward simulations for hypothetical releases from the test site show that the station RN58 would have been affected by the plumes repeatedly during October. Figure B.15c shows as an example the dispersion after 36 h of a hypothetical ten hour release on October 4, 2017 using HYSPLIT with 0.25° GFS (Global Forecast System) data and 1 million particles released. In fact, the station RN58 went back to operation in between and three peaks of elevated ^{133}Xe activity concentration were measured on the days indicated by routine forward simulations from the test site (October 5, 19, and 26). Those peaks consist of five samples with ^{133}Xe activity concentrations between 0.5 and 1 mBq/m^3. Backward ATM results also indicate a high sensitivity of these five samples to being released from the test site. Figure B.15d shows the overlap of the corresponding retro-plumes at time of max-

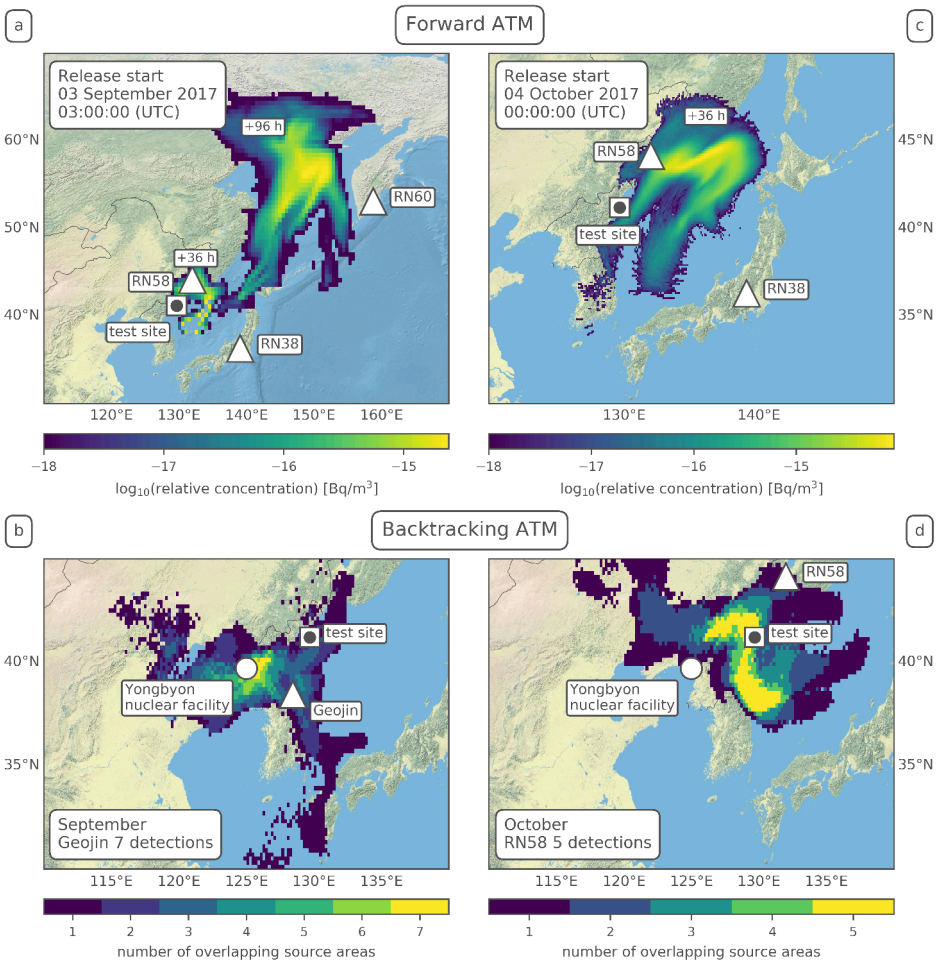

Figure B.15: Atmospheric Transport Modelling results. (a) Forward dispersion modelling after 36 and 96 hours for an immediate release on September 3, 2017. (b) Number of overlapping backward plumes for seven ^{133}Xe detecting samples in north-eastern South Korea from September 7 to 10, 2017 (fixed to 42 hours transport time for each sample). (c) High resolution forward dispersion modelling after 36 hours for a delayed leakage on October 4, 2017. (d) Number of overlapping backward plumes for five ^{133}Xe detecting samples at RN58 Ussurysk during October 2017 (transport time fixed at maximum sensitivity to North Korean test site).

imum sensitivity to the test site. A leakage in the order of 10^{11} Bq ^{133}Xe would have been sufficient to explain the detections at station RN58. Although the measurements and the ATM are consistent with delayed small releases from the test site in October, they cannot be unambiguously attributed to the North Korean test explosion.

B.6 Discussion

A combination of seismological analysis using a double-difference method and remote sensing technologies results in an epicenter location of the 2017 test of 41.3007°N, 129.0728°E, clearly placing the event inside the North Korean nuclear test site, in which all previous tests have been conducted. The epicenter location is confirmed by results from (Wang et al., 2018), who estimated an epicenter location of 41.300°N, 129.078°E ± 50 m, which places the two epicenter solutions only ∼400 to 500 m apart. On May 24, 2018 North Korea invited international media to witness the demolition of the Punggye-ri test site. During a demonstration North Korean officials presented a map showing the relative locations of the six nuclear tests (CNN, 2018). Although the correctness of the information provided

by the North Korean government cannot be verified, comparisons indicate that the assumed locations fit the results from the independent relative location method reasonably well. Two independent methods showed that the 2017 North Korea event was very shallow. The full waveform moment tensor inversion indicates a centroid depth in the range of about 2 km, but has a relatively poor resolution because of the long wavelength of low-pass filtered data. The depth phase modelling of the *P*-waveform was performed at 2.5 Hz and found a centroid depth between 400 and 800 m. According to the crustal profile at the source side, the expected P-wave wavelength is ∼1000 m, which indicates that the source depth is still resolved. This is supposedly the best absolute centroid depth estimate possible from seismological data far from the source. Depth estimations in this study are comparable to results from Wang et al. (2018). The authors used numerical models to minimize the misfit between predicted and observed surface displacements and specified a depth of 450 ± 100 m.

The explosive character of the 2017 event is confirmed by MTI analysis, which indicates a dominant isotropic source part of around 60%. These results are supported by studies by Liu et al. (2018) and Han et al. (2017), who also revealed a dominant positive isotropic source part. Under the assumption of the magnitude-yield relation following Bowers et al. (2001) the estimated m_b of 6.2 (see Subsection B.2.4) for the event results in a yield of 400 kilotons TNT equivalent. This value is assumed to be an upper limit, as following reasons might lead to a yield overestimation: (1) Topography at the test site (see Subsection B.2.5) strongly influences the radiation of seismic energy from the source. This results in higher amplitudes of the *pP*-phase. As the hypocenter location is very shallow, *P*- and *pP*-phases from the event arrive nearly simultaneously at distant receivers and superimpose at frequencies relevant for the estimation of m_b. This superimposition leads to an increase of approximately 1.3 in *P*-wave amplitude in the far-field and consequently to an increase in m_b of around 0.1. (2) Furthermore in the standard calculations of m_b (Gutenberg, 1945a,b; Bormann, 2012), distant-dependent correction curves, which are valid for a DC source, are applied. Gaebler and Ceranna (2017) state, that the use of correction terms for a shallow explosion source can lead to an overestimation of m_b of around 0.2. Taking both these effects into account, the originally estimated value for m_B of 6.2 had to be considered as an upper limit estimate and has to be corrected by a factor of up to 0.3. This correction leads to a lower estimate for m_B of 5.9, similar to $M_W^{(\mathrm{peak})}$ that is estimated from the source time function, which translates to an estimated yield of around 160 kilotons TNT equivalent. Therefore indications are strong that yield might be overestimated, not only for the 2017 explosion, but also for all five previous North Korean nuclear tests.

Following the main event, around eight minutes later, a large aftershock of local magnitude m_L 4.1 was detected. MTI analysis of this event shows a clear negative isotropic part which leads to the conclusion that this event is caused by at least a partial collapse of the cavity formed by the main explosion. These findings are again supported Liu et al. (2018) and Han et al. (2017), who also find a clear negative isotropic source part for the aftershock. According to Liu et al. (2018), the aftershock can qualitatively be interpreted as a rapid destruction of an explosion-generated cracked rock chimney due to cavity collapse. Following this strong aftershock, nine more earthquakes with local magnitudes m_L ranging from 2.5 up to 3.2 were detected by the Korean Meterological Agency (Korean Meterological Agency, 2018) in the region (41.2 to 41.4°N, 129.0 to 129.2°E) until April 2018. Aftershocks in such magnitude range and quantity were not observed from the five previous tests from 2006 to 2016, but are not unusual for nuclear explosions of that size (Boucher et al., 1969).

In the aftermath of the 2017 event measurable surface activity was detected in the region of the Punggye-ri test site. Remote sensing results suggest a distinct pattern of uplift (up to 10 cm) in the western part of the Mt. Mantap massif and subsidence (up to −10 cm) in the

eastern part. The geological interpretation by Coblentz and Pabian (2015) and Pabian and Coblentz (2017) shows a north-south trend of various geological units ranging from carbonates, diorites, granites and gneisses in contact to a younger basalt (layered volcanic) at Mt. Mantap. Furthermore, the structural pattern in the region suggests a north-south trending system of faults up to the main tunnel entrances, with a part of the fault system branching out to the north-west. Considering this geological background the deformation pattern can be interpreted as a (partial) uplift of the basement rocks in the western part. Eventually this is structurally controlled by the north-south trending reverse faults together with the unconformable capping of stratified volcanic sequences. This interpretation is confirmed by multi-spectral optical data from the Pleiades satellite which shows that the layered tuffs are strongly affected by intensive landslide activities.

Overall, accounting for all these activities (surface deformations, the collapse event, aftershocks, landslides) it can be argued, that the internal structure beneath Mt. Mantap might be strongly stressed and shattered due to the last six tests and might be rendered useless for further test explosions (see also Wang et al., 2018).

Despite these strong activities and the enormous release of seismic energy from the event no immediate release of radionuclide was measured by the IMS. This is a strong indication that no direct pathways from the cavity to the surface for the propagation of radionuclide were created during the test and the subsequent collapse-type aftershock. Only a few days after the 2017 event South Korea announced national measurements of ^{133}Xe and proposed a connection of these observations to the test. However, backward ATM calculations performed in the context of this study disfavour the Punggye-ri test site as possible origin for ^{133}Xe but rather point to the Yongbyon nuclear complex as a most likely coincident source region instead in September. Nevertheless, in October 2017 three peaks of ^{133}Xe were detected at the IMS station RN58 in Ussurysk, Russia. Forward as well as backward ATM show directly connecting dispersion conditions and indicate the North Korean test site as a likely source for the ^{133}Xe detections. Nevertheless, other regional sources cannot be excluded and it was not possible to definitely identify the presence of ^{131m}Xe in the RN58 samples, which – in the correct isotropic ratio – would have increased the evidence of a nuclear explosion source (Kalinowski et al., 2010), as for example shown for the 2013 North Korean nuclear explosion by Ringbom et al. (2014). According to calculations of concentration and sensitivity, a release at the test site in the order of a few 10^{11} Bq would have been sufficient to cause and explain the detections at station RN58. This is also quantitatively consistent as the required source term ranges well below the remaining fission inventory even after six to ten half-life of ^{133}Xe (5.2 days) and a small leakage through mountain cracks. However, a direct number of the fission inventory is hard to estimate as the fission yield depends not only on the explosive yield but also on the type of nuclear device. Within the available data it is not possible to determine if nuclear fusion was involved in the process. The largest yield ever achieved by a boosted fission device was 720 kT TNT equivalent of the British *Orange Herald* in 1957. For this explosion an amount of 118 kg ^{235}U was mounted (Arnold and Pyne, 2001). The explosive yield in this study of between 160 and 400 kilotons TNT equivalent is therefore still fully compatible with a fission only device.

DInSAR results show a large area of strong displacement in the case of the 2017 test and it is not possible to demarcate a definite surface location of the test epicenter from these measurements. However retrieving a ground truth from DInSar measurements from the January 2016 test, which showed a clear and distinct maximum of surface displacement, can help to provide an absolute epicenter location of the 2017 test. By combining remote sensing and relative locations methods only the epicenter of the event can be estimated. A third method (depth phase modelling) is required for the complete estimation of the

2017 test hypocenter. This method is further able to provide an explanation for the large difference in m_b and M_W, which has not been observed in this order for the previous tests. Furthermore while for previous weaker tests radionuclide measurements were able to prove the nuclear character of the explosions (Ross et al., 2017), radionuclide measurements alone in September 2017 could have been misleading in regards to the source area. This examples clearly demonstrate that an integrated multi-technology and multi-methodology approach is essential for a reliable and comprehensive identification and characterization of a potential nuclear test.

B.7 Conclusions

Overall, the following main conclusions can be deduced from this study:

- Explosive character of the September 3, 2017 North Korean event is confirmed by MTI analysis.
- Yield of the event is estimated to be around 400 kilotons TNT equivalent with indications that this value should be considered as an upper limit and might be as low as 160 kilotons TNT equivalent. This overestimation can be explained by the enhancement of peak amplitudes of teleseismic P-waves due to topography and depth phase effects.
- The estimated yield of the nuclear device is certainly smaller than the largest documented yield ever achieved by a boosted fission device and is therefore still compatible with a fission only device.
- Strong surface deformations ($\pm$10 cm) are observed in an area of 3×4 km^2. Comparisons of affected surface area to the January 2016 test underline the enormous power the 2017 nuclear test. Furthermore multiple landslides as well as a number of aftershocks were observed in the aftermath of the test.
- The aftershock directly following the nuclear explosion has a similar depth as the test and can be characterized as a collapse of the cavity created by the test.
- Infrasound signals measured at the station I45RU can clearly be related to the 2017 event. It is the first time that a thermospheric propagation path of infrasound could be observed for an underground nuclear explosion.
- No immediate measurements of radionuclide related to the test in September were observable, but later occurrences of radionuclide are consistent with a delayed leakage from the test site in October.
- The test site might have been strongly stressed and shattered and thus rendered useless for further test activities.

The combination of the results from the different technologies and methods yields a reliable estimation of hypocenter, magnitude, explosive energy, source mechanism as well as an indication for delayed leakage of ^{133}Xe from the test site. The cross-links between the different results complement each other in a consistent manner. The multi-technology and multi-methodology analysis presented in this study, clearly indicates that the September 2017 North Korean event was in fact a nuclear test. Even in the phase of pre entry-into-force the CTBTO verification regime has again demonstrated its readiness with respect to the recent nuclear test.